Werkstofftechnik

UNIVERSITÄT SIEGEN

Xinyue Chen

Surface Functionalization of Boron/Nitrogen Doped Diamond for Electrocatalytic Nitrate Reduction

Schriftenreihe der Arbeitsgruppe
des Lehrstuhls für Oberflächen- und Werkstofftechnologie
im Institut für Werkstofftechnik

Herausgeber: Prof. Dr. rer. nat. habil. Xin Jiang

Band 22

Xinyue Chen

Surface Functionalization of Boron/Nitrogen Doped Diamond for Electrocatalytic Nitrate Reduction

Schiftenreihe derArbeitsgruppe des Lehrstuhls für Oberflächen-und Werkstofftechnologie im Institut für Werkstofftechnik

Impressum

Prof. Dr. rer. nat. habil. Xin Jiang

Lehrstuhl für Oberflächen-und Werkstofftechnologie

Institut für Werkstofftechnik

Universität Siegen

57076 Siegen

ISSN: 2194-0096

Zugl.: Siegen, Univ., Diss., 2025

Surface functionalization of boron/nitrogen doped diamond for electrocatalytic nitrate reduction

Von der Naturwissenschaftlich-Technischen Fakultät

der Universität Siegen

zur Erlangung des Grades eines Doktors

der Ingenieurwissenschaften

genehmigte

Dissertation

von:	M. Sc. Xinyue Chen
aus:	Xinjiang, China

eingereicht am:	12. Feb. 2025
Mündliche Prüfung am:	15. Mai 2025
Referent:	Prof. Dr. rer. nat. habil. Xin Jiang
Korreferent:	Prof. Dr. Nianjun Yang

Kurzfassung

Zahlreiche Diamantmaterialien haben sich aufgrund ihrer einzigartigen chemischen, physikalischen und mechanischen Eigenschaften als Schlüsselmaterial für verschiedene Anwendungen etabliert. Insbesondere leitfähige Diamantfilme, zumeist dotierte Diamantfilme (Dia), werden weit verbreitet als Elektroden für fortschrittliche elektrochemische Anwendungen eingesetzt. Die Dotierung von Diamantfilmen bezeichnet die Einführung von Fremdatomen wie Bor, Stickstoff oder Phosphor in das Diamantgitter, wodurch deren elektronische und strukturelle Eigenschaften verändert werden. Besonders interessant ist die Ko-Dotierung, bei der zwei oder mehr Dotierstoffe (z. B. Bor und Stickstoff) gleichzeitig eingebracht werden. Diese Methode optimiert synergistisch die Leitfähigkeit, elektrochemische Aktivität und Stabilität der Diamantfilme. Ko-dotierte Diamantfilme verbessern den Ladungstransport, schaffen zusätzliche aktive Stellen und steigern die katalytische Effizienz, was ihre Anwendung in Bereichen wie Energiespeicherung, Schadstoffabbau und Katalyse erweitert.

Im Gegensatz zu (ko-)dotierten Diamantfilmen bestehen Diamantkomposite (DCs) aus Diamant und anderen Komponenten und bieten einzigartige Möglichkeiten, diese Fortschritte weiter zu nutzen. Sie kombinieren die herausragenden Eigenschaften von Diamant mit denen ihrer Bestandteile, was zu umfangreichen Untersuchungen in mechanischen, physikalischen, chemischen und biomedizinischen Anwendungen geführt hat. Diese „ 1+1 > 2 “ -Strategie hat sich als äußerst effizient für die Entwicklung fortschrittlicher Diamant-basierter Funktionsmaterialien erwiesen. Obwohl DCs außergewöhnliche chemische und physikalische Eigenschaften bieten, stellt die begrenzte elektrokatalytische Leistung von Diamant-basierten Elektroden aufgrund weniger aktiver Stellen eine erhebliche Herausforderung dar.

Vor diesem Hintergrund adressiert diese Dissertation die genannten Herausforderungen durch den Einsatz von Bor- und Stickstoff-ko-dotierten Diamantkompositen (BNDD), die Entwicklung verschiedener Zwischenschichten und weitere Oberflächenmodifikationen - die Bildung von DCs -, um die

elektrokatalytische Aktivität und Stabilität dieser Diamantmaterialien zu verbessern und ihre elektrochemischen Anwendungen in den Bereichen Energiespeicherung (hier Superkondensatoren und Zink-Batterien) und -umwandlung (hier elektrochemische Nitratreduktionsreaktion) zu untersuchen. Die Dissertation beschreibt zunächst die experimentellen Techniken zur Synthese und Charakterisierung dieser Materialien, einschließlich Magnetronsputtern, Elektroabscheidung und mikrowellenunterstützter plasmaverstärkter chemischer Gasphasenabscheidung. Der Schwerpunkt liegt dann auf der Herstellung und Charakterisierung von BDDD-Filmen und ihren Kompositen, einschließlich BNDD/Metall/Si, Cu_2O@CNF-BNDD (CNF = Kohlenstoff -Nanofasern) und teilweise bedeckten BNDD/Ti/Si. Detaillierte Methoden zur Analyse der Morphologie, Oberflächenchemie und elektrochemischen Leistung dieser Filme werden diskutiert, ebenso wie ihre elektrochemischen Anwendungen, darunter Superkondensatoren, katalytische Nitratreduktion und deren Integration mit der elektrochemischen Methylorange(MO)-Degradation unter Verwendung von BNDD-Filmen sowie Zink-Nitrat-Batterien. Die Inhalte werden wie folgt detailliert beschrieben:

Im ersten experimentellen System wurden BNDD-Filme auf einem Si-Substrat mit/ohne Ti- und Ta-Zwischenschichten gezüchtet, was zur Herstellung von BNDD/Si-, BNDD/Ti/Si- und BNDD/Ta/Ti/Si-Elektroden führte. Nach der Charakterisierung durch Mikroskopie, Spektroskopie, elektrochemische Techniken und Simulationen der Dichtefunktionaltheorie (DFT) wurde der Zusammenhang zwischen ihrer Zusammensetzung, Grenzflächenstruktur, Ladungstransport und elektrochemischen Eigenschaften untersucht. Die BNDD/Ta/Ti/Si-Elektroden zeigten schnellere Elektronentransferraten und geringere Widerstände für Redox-Sonden im Vergleich zu anderen Diamant-Elektroden. Die Bildung von TaC erleichterte das Ladungsträgertunneln und erhöhte die Konzentration elektrisch aktiver Defekte, wodurch die elektrochemische Leistung verbessert wurde. Als Fallstudie wurde die BNDD/Ta/Ti/Si-Elektrode als Kondensatorelektrode für die Herstellung eines Superkondensators auf Redox-Elektrolyt-Basis eingesetzt.

Im zweiten experimentellen System wurde die BNDD-Oberfläche mit Kohlenstoff-Nanofasern (CNF) und anschließend mit Cu_2O funktionalisiert. Das resultierende Cu_2O@CNF-BNDD-Komposit wurde als effizienter Elektrokatalysator für die elektrochemische Nitratreduktionsreaktion (NO_3RR) eingesetzt. Dieses Komposit vereint die einzigartigen Eigenschaften von BNDD-Filmen, CNFs und Cu_2O. Zum Beispiel verfügen BNDD-Filme über ein breiteres elektrochemisches Potenzialfenster, das die konkurrierende Wasserstoffentwicklungsreaktion (HER) unterdrückt, was zu einer hohen Faraday-Effizienz der NO_3RR führt.

Im dritten experimentellen System wurde die langsame Sauerstoffentwicklungsreaktion (OER) durch eine schnelle photo-elektrokatalytische Oxidationsreaktion von Methylorange (MO) ersetzt, um die langsame Kinetik der Acht-Elektronen-NO_3RR zu bewältigen. In einem solchen integrierten System liefert die anodische MO-Abbaureaktion auf einer BNDD/Ti/Si-Elektrode Elektronen, während die kathodische Reaktion auf einer Cu_2O/CNF-BNDD-Kathode Nitrat zu Ammoniak reduziert.

Zusammenfassend liefert diese Dissertation neue Einblicke in die Gestaltung und Optimierung von ko-dotierten Diamant(BNDD)-Filmen und ihren Kompositen für potenzielle elektrochemische Anwendungen in den Bereichen Energiespeicherung und -umwandlung.

Danksagung

I am deeply grateful to **Prof. Xin Jiang** for his unwavering support and mentorship throughout my PhD journey, which began in February 2021 at the LOT (Chair of Surface and Materials Technology), University of Siegen. His generosity in providing me with the opportunity to pursue this dissertation, coupled with his encouragement of academic freedom, allowed me to explore a wide range of research projects with creativity and independence. His profound knowledge of functional thin-film preparation techniques and exceptional expertise in the field have been a constant source of inspiration, motivating me to delve deeply into the fascinating realm of diamond research.

I would like to express my heartfelt gratitude to **Prof. Nianjun Yang** at Hasselt University for his enduring support and for playing a pivotal role in bringing me to the University of Siegen. Throughout my personal and academic journey, his thoughtful guidance and encouragement have been invaluable, especially during the more challenging moments of my PhD studies. I am deeply appreciative of his willingness to share his knowledge and expertise, as well as his invaluable advice on my experiments. His trust and mentorship have been a constant source of motivation, for which I am sincerely grateful.

A heartfelt thanks goes to **Ximan Dong**, whose support has been immeasurable both in my research and daily life. The meaningful discussions, heartfelt conversations, shared meals, and travels have left me with cherished memories. I am also deeply thankful to **Changli Li, Yao Li**, and **Dr. Zhaofeng Zhai**, whose dedication to their own research has been a constant source of inspiration and motivation during my time in Siegen.

I am sincerely appreciative of the members of the LOT team, who have contributed significantly to my academic journey. I would like to give special thanks to **Dr. Chuyan Zhang** for her invaluable assistance with theoretical calculations and simulations. I also extend my gratitude to **Mrs. Andrea Brombach** for her kind support in all student affairs matters. My heartfelt thanks also go to **Dr. Thorsten**

Staedler, Dr. Kevin Suta, Dr. Hamid Ullah, Dr. Aleksandr Zubtsovskii, Dr. Akif Zeb, Petra auf dem Brinke, Tianxiao Guo, Claudia Kretzer, Bharath Reddy Lakki Reddy Venkata, Stefan Wagener, and Chen Wang for their consistent academic and personal support. I feel like a mosaic pieced together by the kindness and contributions of those around me, each interaction shaping and empowering me along this journey.

I would also like to acknowledge the collaborators of this dissertation. I am profoundly grateful for the immense help and support of **Prof. Ken Haenen** from the Institute for Materials Research at Hasselt University. My heartfelt thanks go to **Dr. Paulius Pobedinskas, Dr. Rozita Rouz, Dr. Rani Mary Joy, Essraa Ahmed** and **Giridharan Krishnamurthy** for their contributions to diamond sample growth. Their expertise and dedication have been integral to the progress of my research.

I am immensely grateful to the members of the Electron Microscopy for Materials Research (EMAT) group at the University of Antwerp, particularly **Dr. Nicolas Gauquelin** and **Dr. Daen Jannis**, for their assistance with TEM characterization. My appreciation extends to **Prof. Holger Schönherr** from the research group Physical Chemistry I and to the team members who supported the XPS and UV-visible spectrum characterizations: **Dr. Kawaljit Kaur, Dr. Fanfan Zhang, Dr. Chunyun Zhu, Zhiliang Chen, and Renée Sophie Hoffmann.** Additionally, I would like to thank **Prof. Robert Brandt, Markus Hartmann** for XRD measurements, **Felix Thiel** for Raman measurements and **Dr. Aly Mohamed Elsayed Hafez** for TOF-SIMS measurements.

Finally, I wish to express my profound gratitude to my family and friends. Their unwavering emotional support and strength have been my anchor throughout this challenging journey, enabling me to persevere and reach the finish line.

As I conclude this dissertation, I reflect on how the world is like a vast thin film, and may we each strive to be a unique, shining diamond upon it.

Siegen, in Feb. 2025 Xinyue Chen

Publikationen

1. **Xinyue Chen**, Ximan Dong, Chuyan Zhang, Meng Zhu, Essraa Ahmed, Giridharan Krishnamurthy, Rozita Rouzbahani, Paulius Pobedinskas, Nicolas Gauquelin, Daen Jannis, Kawaljit Kaur, Aly Mohamed Elsayed Hafez, Felix Thiel, Rainer Bornemann, Carsten Engelhard, Holger Schönherr, Johan Verbeeck, Ken Haenen, Xin Jiang, and Nianjun Yang, Interlayer affected diamond electrochemistry, *Small methods*, 2024, 2301774.
2. **Xinyue Chen**, Ximan Dong, Xin Jiang, and Nianjun Yang, Diamond Composite: A "1+1 >2" Strategy to Design and Explore Advanced Functional Materials, *Accounts of Materials Research*, 2024, 33, 015401.
3. **Xinyue Chen**, Xin Jiang, Nianjun Yang, Graphdiyne Electrochemistry: Progress and Perspectives, *Small*, 2022, 2201135.
4. Ximan Dong, **Xinyue Chen**, Xin Jiang, and Nianjun Yang, Light-Assisted Energy Storage Devices: Principles, Performance, and Perspectives, *Advanced Energy Materials,* 2023, 2301143.

Content

Symbol List ..... **IV**

Abstract ..... **XI**

Chapter 1. Introduction **1**

1.1 Diamond films **1**

1.1.1 Diamond growth 1

1.1.2 Diamond doping 1

1.1.3 Co-doped diamond films 2

1.2 Diamond composites **4**

1.2.1 Synthesis 5

1.2.2 Properties 8

1.2.3 Applications 10

1.3 Motivation of the thesis **13**

1.4 Overview of the thesis **14**

Chapter 2. Experimental **17**

2.1 Film deposition techniques **17**

2.1.1 Magnetron sputtering physical vapor deposition 17

2.1.2 Electrodeposition 18

2.1.3 Microwave plasma enhanced chemical vapor deposition 18

2.2 Preparation **19**

2.2.1 Preparation of BNDD/Metal/Si films 19

2.2.2 Preparation of Cu_2O@CNF/BNDD composites 21

2.2.3 Preparation of BNDD/Ti/Si films 23

2.3 Characterization **25**

2.3.1 Morphology and physical structure characterization 25

2.3.2 Surface chemistry analysis 27

2.3.3 Electrochemical characterization 28

2.4 Performance measurements of electrochemical devices 31

2.4.1 Supercapacitors using the BNDD films 31

2.4.2 Electrocatalytic nitrate reduction reactions 32

2.4.3 Electrocatalysts and photoelectrocatalysts 34

2.4.4 Assembly of a zinc-nitrate battery 36

2.5 Ion detection 37

2.5.1 Determination of NO_3^--N 38

2.5.2 Determination of NO_2^--N 39

2.5.3 Determination of NH_4^+-N 40

2.6 Computer simulations 42

2.6.1 Models construction for BNDD/Si, BNDD/TiN, and BNDD/TaC 42

2.6.2 Models construction for Cu and Cu_2O 43

Chapter 3. BNDD/Metal/Si films for supercapacitors 45

3.1 Characterization for BNDD/Metal/Si films 47

3.2 Theoretical simulation of the BNDD films 60

3.3 BNDD/Metal/Si films for supercapacitor fabrication 62

3.4 Conclusions 68

Chapter 4. Cu_2O@CNF-BNDD composites for NO_3RR and Zn-NO_3^- batteries 69

4.1 Characterization of Cu_2O@CNF-BNDD 71

4.2 Electrochemical NO_3RR performance of Cu_2O@CNF-BNDD 74

4.3 DFT simulations 79

4.4 Rechargeable Zn-nitrate batteries 83

4.5 Conclusions 86

Chapter 5. NO_3RR using electrons generated from MO oxidation 88

5.1 Characterization of BNDD/Ti/Si films 89

5.2 Photo-electrcatalytic methyl orange oxidation of BNDD/Ti/Si 98

5.3 Coupling of anodic methyl orange oxidation and cathodic NO_3RR 99

5.4 Conclusions 101

Chapter 6. Summary and outlook 102

6.1 Summary 102

6.2 Outlook 104

References 105

Symbol List

Abbreviations

AC	alternating current
BDD	boron-doped diamond
BNDD	boron and nitrogen co-doped diamond
CV	cyclic voltammetry
CNFs	carbon nanofibers
CO_2RR	electrochemical CO_2 reduction reaction
CP	chronopotentiometry
CVD	chemical vapor deposition
DC	diamond composite
Dia	diamond
DFT	density functional theory
DOS	density of states
ECSA	electrochemical active surface area
EDLC	electrical double-layer capacitor
EIS	impedance spectroscopy
ELNES	energy-loss near edge structure
FE	faradaic efficiency
FETs	field-effect transistors
PEO	plasma electrolytic oxidation
GCD	galvanostatic charge and discharge
GGA	generalized-gradient approximation
Gr	graphite
Gra	graphene
HAADF	high angle annular dark field
HEP	hydrogen evolution potential

HFCVD	hot filament chemical vapor deposition
HPHT	high pressure-high temperature
HER	hydrogen evolution reaction
LODs	lower detection limits
LSV	linear sweep voltammetry
MO	methyl orange
MPCVD	microwave plasma chemical vapor deposition
NDD	nitrogen-doped diamond
NO_3RR	nitrate reduction reaction
OCV	open-circuit voltage
OER	oxygen evolution reaction
OEP	oxygen evolution potential
PAW	projector augmented wave method
PBE	Perdew-Burke-Ernzerhof
PC	pseudocapacitor
PEO	plasma electrolytic oxidation
RHE	reversible hydrogen electrode
SAED	selected area electron diffraction
SCF	self-consistent field
SEM	scanning electron microscope
STEM-EELS	scanning transmission electron microscopy - electron energy loss spectroscopy
TCVD	thermal chemical vapor deposition
TEM	transmission electron microscope
ToF-SIMS	Time-of-flight secondary ion mass spectrometry
UV-VIS	ultraviolet spectroscopy or ultraviolet-visible
VASP	vienna ab initio simulation package
XPS	X-ray photoelectron spectroscopy

XRD	x-ray diffraction
μXRD	Micro-X-ray diffraction

Chemicals

Ar	argon
B	boron
BN	boron nitride
C	carbon
$C_6H_8N_2O_2S$	sulfapyridine
$C_{12}H_{14}N_2 \cdot 2HCl$	pyridoxine hydrochloride
Cd(II)	cadmium ion
CH_4	methane
Co_4N	cobalt nitride
Cu(II)	copper(ii) ion
Cu_2O	copper(i) oxide
$Cu_2SO_4 \cdot 5H_2O$	copper(ii) sulfate pentahydrate
CuO	copper(ii) oxide
$Fe(CN)_6^{3-/4-}$	ferricyanide/ferrocyanide
Ge	germanium
H_2	hydrogen
H_2SO_4	sulfuric acid
HCl	hydrochloric acid
KOH	potassium hydroxide
MnO_2	manganese dioxide
N	nitrogen
N_2	nitrogen gas
Na_2SO_4	odium sulfate
$NaNO_3$	sodium nitrate

Nb	niobium
Nessler's regent	potassium tetraiodomercurate(II) solution
NH_2SO_3H	sulfamic acid
NH_3	sulfamic acid
NH_4Cl	ammonium chloride
NO_3^--N	nitrate nitrogen
O_2	oxygen
Pb(II)	lead(ii) ion
Pt	platinum
$Ru(NH_3)_6^{2+/3+}$	ruthenium ammines
TMS	tetramethylsilane
Ta	tantalum
TaC	tantalum carbide
Ti	titanium
TiC	titanium carbide
TiN	titanium nitride
TiO_2	titanium dioxide
TMB	trimethyboron
Zn	zinc
Zn(II)	zinc ion
β-SiC	β-silicon carbide

Symbols

C	capacitance
C_{dl}	double-layer capacitance
ΔE^*	change in activation energy
ΔG^*	change in Gibbs free energy
ΔS	change in entropy

ΔZPE	change in zero-point energy
E_g	band gap energy
F	faraday's constant
I	current
λ	wavelength
P	power
Q	charge
R_{ct}	charge transfer resistance
R_s	internal resistance
S	entropy
T	temperature
V	voltage
Z_w	mass transfer impedance
η	removed fraction

Units

%	percentage
°	degree
Å	ångström (10^{-10} meters)
c mol^{-1}	coulombs per mole
cm	centimeter
cm^{-3}	per cubic centimeter
cm^2	square centimeter
°C	degrees celsius
eV	electron volt
Hz	hertz (frequency)
h	hour
k	boltzmann constant

kV	kilovolt (thousand volts)
kW kg^{-1}	kilowatt per kilogram (power per unit mass)
l/mm	lines per millimeter (resolution measure)
mA cm^{-2}	milliamps per square centimeter (current density)
mbar	millibar (pressure)
meV/pixel	millielectron volt per pixel (energy resolution)
mg/L	milligrams per liter (concentration)
mF cm^{-2}	millifarads per square centimeter (capacitance)
min	minute
mL	milliliter (volume)
ms	millisecond (time)
mrad	milliradian (angle)
mV	millivolt
mV s^{-1}	millivolts per second (scan rate)
mW	milliwatt
mW·cm^{-2}	milliwatts per square centimeter (power density)
nm	nanometer
pA	picoampere
ppm	parts per million
rpm/min	revolutions per minute
sccm	standard cubic centimeters per minute (flow rate)
Torr	unit of pressure
V	volt
V/s	volts per second
W	watt
Wh kg^{-1}	watt-hours per kilogram
μF cm^{-2}	microfarads per square centimeter
μg L^{-1}	micrograms per liter

$\mu g \cdot h^{-1} \cdot cm^{-2}$	micrograms per hour per square centimeter
μm^2	square micrometer
Ω	ohm

Abstract

Numerous diamond materials have been emerging as a critical material for various applications, due to their unique chemical, physical, and mechanical properties. Among them, conductive diamond films, in most cases doped diamond films (Dia) have been widely employed as electrodes for advanced electrochemical applications. Doping of diamond films refers to the introduction of foreign atoms such as boron, nitrogen, or phosphorus into the diamond lattice, leading to their altered electronic and structural characteristics. Of special interest, a co-doping process involves simultaneous incorporation of two or more dopants (e.g., boron and nitrogen), thus synergistically optimizing the diamond's conductivity, electrochemical activity, and stability. These co-doped diamond films enhance charge transport, create additional active sites, and improve catalytic efficiency, enabling their broader applications in fields such as energy storage, pollutant degradation, and catalysis.

Different from (co-)doped diamond films, diamond composites (DCs) - comprise diamond and other components, thus offering unique opportunities to further leverage these advancements. They effectively combine the outstanding properties of diamond with those of its components, leading to extensive exploration and testing in mechanical, physical, chemical, and biomedical applications. This "1+1 > 2" strategy has proven to be highly efficient for designing and developing advanced diamond-based functional materials. Although DCs offer exceptional chemical and physical properties, the poor electrocatalytic performance of diamond-based electrodes, mainly due to limited active sites, presents a significant challenge.

In this context, this thesis addresses above issues by harnessing boron and nitrogen co-doped diamond (BNDD) composites, designing various interlayers and further adding surface modifications – the formation of DCs - to gain enhanced electrocatalytic activity and stability of these diamond materials, and exploring their electrochemical applicaitons in the fields of electrochemical energy storage (here

supercapacitors and zinc batteries) and conversion (here electrocatalytic nitrate reduction reaction). This thesis firstly outlines the experimental techniques for synthesizing and characterizing these materials, including magnetron sputtering, electrodeposition, and microwave plasma-enhanced chemical vapor deposition. Its focus then shifts to the preparation and characterization of BDDD films and their composites, including BNDD/Metal/Si, Cu_2O@CNF-BNDD (CNF = carbon nano fibers), and partially covered BNDD/Ti/Si. Detailed methods for analyzing the morphology, surface chemistry, and electrochemical performance of these films are discussed, along with their electrochemical applications such as supercapacitor formation, catalytic nitrate reduction and its integration with electrochemical methyl orange (MO) degradation using BNDD films, and Zn-nitrate batteries. The details of these contents are described as follows.

In the first experimental system, the BNDD films were grown on a Si substrate with/without Ti and Ta interlayers, resulting in the fabrication of BNDD/Si, BNDD/Ti/Si, and BNDD/Ta/Ti/Si electrodes. After they were characterized using microscopies, spectroscopies, electrochemical techniques, and density functional theory (DFT) simulations, the relationship between their composition, interfacial structure, charge transport, and electrochemical properties was investigated. The BNDD/Ta/Ti/Si electrodes demonstrated faster electron transfer rates and lower resistances for redox probes compared to other diamond electrodes. The formation of TaC facilitated carrier tunneling and increased the concentration of electrically active defects, enhancing its electrochemical performance. As a case study, the BNDD/Ta/Ti/Si electrode was employed as a capacitor electrode to construct a redox-electrolyte-based supercapacitor. This section highlights the importance of interlayer composition and its impact on charge transfer and relevant electrochemical performance of co-doped diamond films, in other worlds how a tailored interlayer design can unlock new capabilities of co-doped diamond (e.g., BNDD) films.

In the second experimental system, the BNDD surface was functionalized with

carbon nanofibers (CNF) and further with Cu_2O. The resultant Cu_2O@CNF-BNDD composite was introduced as an efficient electrocatalyst for the electrochemical nitrate reduction reaction (NO_3RR). This composite has unique properties of BNDD films, CNFs and Cu_2O. For example, the BNDD films have a wider electrochemical potential window that suppresses the competing hydrogen evolution reaction (HER), resulting in a high NO_3RR faraday efficiency. The CNFs grown on the BNDD surface regulate the sp^2 content, enhancing electrical conductivity and electrochemical activity. Furthermore, the Cu_2O catalyst donates electrons to the lowest unoccupied π^* orbital of NO_3^-, making it highly effective for NO_3RR. As revealed in DFT calculations, the d-band center of Cu 3*d* orbitals of reconstructed Cu NPs is shifted to -2.47 eV, balancing the adsorption of nitrogen-contained intermediates, and reducing the overpotential of NO_3RR from 1.11 eV to 0.15 eV. Taking the advantage of a eight-electron nitrate-to-ammonia reaction and the exceptional activity of Cu_2O@CNF-BNDD, a Zn-nitrate battery system was further proposed, where dual functionality was offered by using NO_3RR-generated electrons for both electricity production and ammonia generation. This strategy simultaneously degrades nitrate pollutants and produces valuable chemicals.

In the third experimental system, the sluggish oxygen evolution reaction (OER) was proposed to be replaced with a fast photo-electrocatalytic oxidation reaction of methyl orange (MO) with an aim to address the slow kinetics of the eight-electron NO_3RR. In such an integrated system, the anodic MO degradation reaction occurring on a BNDD/Ti/Si electrode provides electrons, while the cathodic reaction performed on a Cu_2O/CNF-BNDD cathode reduces nitrate to ammonia. Comprehensive characterization of these composite electrodes demonstrates their impact on electron transfer and electrochemically active surface area for both processes. This "three birds with one stone" strategy not only degrades nitrate pollutants and produces valuable chemicals, but also degrades dye molecules, providing a framework for viable NO3RR and waste degradation processes.

In summary, this thesis provides new insights into the design and optimization of BNDD films and their composites for some potential electrochemical energy storage and conversion applications. By enhancing active sites and modifying surface structure of BNDD films, this thesis proves the great appeal of co-doped diamond films and their composite in the aspects of electrochemical energy storage, pollutant degradation, and electrocatalysis, boosting future developments in the synthesis, characterization and electrochemical applications of various diamond materials and related devices.

Chapter 1. Introduction

1.1 Diamond films

1.1.1 Diamond growth

It is known that diamond can be synthesized using two common artificial approaches: *via* the high pressure-high temperature (HPHT) method invented in 1955, and chemical vapor deposition (CVD) techniques till the 1980s.[1,2]

Taking the diamond growth on non-diamond substrates by means of microwave plasma enhanced CVD (MPCVD) technique as an example, its distinct steps (**Figure 1.1**) involve substrate pre-treatment (e.g., cleaning, etching), seeding/nucleation, and growth within a MPCVD chamber. Prior to diamond growth, a mixture of hydrocarbon gas (usually methane) and high-concentration hydrogen (≈ 95%) needs to be introduced into the MPCVD chamber. The dissociation of the reaction molecules occurs within a plasma, then carbon species are deposited on the subsctrate.[3] Hydrogen abstraction serves a dual role during diamond growth: extracting hydrogen from the hydrocarbon gas, creating a methyl radical (CH_3^-), and forming active radical sites on hydrogen-terminated surfaces conducive to adding carbon radicals (CH_3^-). Simultaneously, hydrogen radicals remove non-diamond carbon from the substrate, yielding high-quality diamond films. Varying hydrocarbon gas concentration (e.g., methane) yields distinct diamond growth patterns. Lateral growth, two-dimensional (2D) terrace nucleation, and three-dimensional (3D) growth of diamond films are thus possible.[4,5]

1.1.2 Diamond doping

Pure (intrinsic) diamond is a material with wide band gap material (E_g=5.47 eV) and there are little amounts of electrons that can move under electrical fields. Hence, appropriate doping is necessary when diamond is attempted to be utilized as a

conductive material. Boron, nitrogen, phosphorus, sulphur and arsenic are utilized dopant for diamond doping. Among them, boron is the most common, which creates a state just above the valence band (0.35 eV). The doping level of boron in a boron-doped diamond (BDD) film can be up to 10^{21} atoms cm^{-3}. The heavy doped BDD film exhibits *p*-type semiconducting behavior with metal-like conductivity due to the high concent ration of hole carriers introduced by boron doping (doping level is higher than 10^{20} atoms cm^{-3}). It must be highlighted here that the electrochemistry of doped diamond strongly depends on the amount of sp^3-carbon and carbon impurities, surface terminations, and defects in diamond layers.[6-9] For example, heavily boron-doped BDD exhibits metal-like conductivity,[6] while nitrogen-doped diamond (NDD) provides a wider potential window.[10]

In terms of their electrochemical applications, doped diamond film (based) electrodes have been widely employed for electrochemical sensors,[11,12] supercapacitors,[13,14] electrocatalytic corrosion,[15] electrocatalysis (e.g., oxygen reduction reaction (ORR)),[16] and other applications.[17]

1.1.3 Co-doped diamond films

In addition to single-dopant doped diamond films (e.g., BDD and NDD), co-doped diamond films, namely those involve the simultaneous introduction of two different doping elements into the diamond structure (e.g., with common dopants including boron, phosphorus, and nitrogen) have been paid extreme attention very recently.[18]

The preparation of co-doped diamond films typically employs CVD techniques, such as MPCVD and hot filament chemical vapor deposition (HFCVD).[19] These methods commonly use hydrogen, methane, and borane along with nitrogen gas as the doping sources. Under controlled conditions, the precise introduction of two dopants into the diamond structure was conducted.[20] For example, a common co-doping combination is boron and nitrogen. By adjusting the composition of the reaction gases

and the deposition temperature, a uniform co-doped layer was formed within the diamond structure. By varying the doping ratio of boron and nitrogen, the crystal structure and surface chemical properties of boron-nitrogen doped diamond (BNDD) films were effectively tuned.[21]

Compared to pure and single-doped diamond, moderate B-N co-doping can optimize the band structure of diamond, enhance the density of states (DOS), and improve electron transfer rates, thereby increasing conductivity and electrochemical activity. Additionally, co-doping generally enhances the diamond's electrical conductivity, thermal conductivity, and chemical stability. The combination of boron and nitrogen doping thus not only improves the *p*-type and *n*-type conductivity of the diamond, but also enhances its electrochemical activity and mechanical strength. However, excessive B-N co-doping (approaching a 1:1 ratio) may lead to electron-hole compensation, reducing the free carrier concentration and consequently lowering conductivity and catalytic performance. Therefore, precise control of the B-N doping ratio is essential to fully exploit the advantages of BNDD in electrochemical energy conversion and catalytic applications.

For example, co-doped diamond with an appropriate ratio holds great promise in various fields. It can be used in high-performance electronic devices, such as high-power semiconductors, sensors, and field-effect transistors (FETs).[22] In the energy sector, co-doped diamond electrodes have been widely used for supercapacitors, water electrolysis, fuel cells, and other electrochemical devices, thanks to their excellent conductivity and electrocatalytic properties. They are also often used in the degradation of organic pollutants and water treatment applications, due to their high chemical stability and corrosion resistances. In recent reports, the electrochemistry of co-doped diamond films has been investigated and discussed.[21,23-26] Compared with single-dopant doped diamond, bi-element incorporated diamond regulates the electronic structures of a diamond film, resulting in faster electron transfer rates and higher catalytic ability toward different

reactions.[27-29] Both BDD and BNDD films were utilized for the ensemble of supercapacitors.[23] The electrocatalytic selectivity and efficiency of the CO_2 reduction reaction (CO_2RR) on BNDD electrodes for ethanol production were found to be highly enhanced. This is due to the synergistic effect of B and N co-doping on electrocatalytic activity of carbon materials and fine balance between the N content and H_2 evolution potential. In these reactions, diamond is particularly beneficial under electrochemically reducing conditions, since the competing reaction of H^+ reduction is particularly facile on metals and most other electrode materials.[24] The BNDD films with adjustable nitrogen and boron dopant ratios exhibit similar performance toward the ORR as a commercial Pt/C catalyst, including high current densities for the ORR and its long-term durability during the ORR.[21]

1.2 Diamond composites

Diamond composite (DCs) refers to a system which consists of diamond and other components.[30-32] Various interactions between diamond and other components exist.[33,34] The first DC - Dia/β-silicon carbide (β-SiC) composite - was grown in 1992 by means of CVD technique.[35] Later on, other DCs, produced using different CVD techniques, have been reported, including Dia/carbides,[35-40] Dia/oxides,[8,41-43] Dia/nitrides,[40,44] Dia/sp^2-carbon,[9,45] Dia/metal,[46] Dia/metal alloy,[47] and Dia/organic composites.[48] Meanwhile, these composites possess different micro- and nanostructures (**Figure 1.1**).[49]

Since DCs fully combine the outstanding properties of diamond with those of other components, their utilization in the mechanical, physical, chemical and biomedical fields have been extensively explored and tested. This “1+1 >2” strategy is believed to be extremely efficient and useful to design and explore advanced diamond functional materials. The origin of superior enhancement and/or new properties of these DCs using the 1+1 > 2 strategy stems from the interface and interactions between individual components as well as their synergistic effects.[50-51]

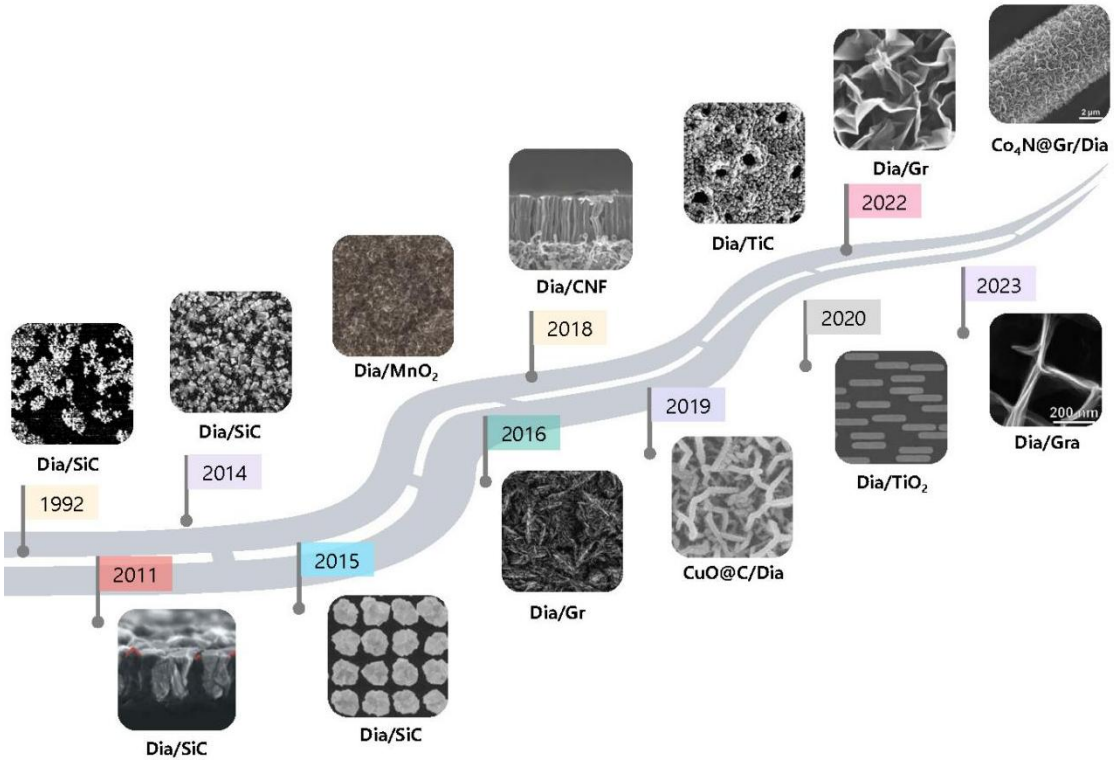


Figure 1.1 *SEM images of several typical DCs that were designed and synthesized in our group since 1992. Reproduced with permission from ref 35. Copyright 1992 AIP Publishing. Reproduced with permission from ref 36. Copyright 2011 Elsevier. Reproduced with permission from ref 38. Copyright 2014 Elsevier. Reproduced with permission from ref 49 Copyright 2015 Springer International Publishing. Reproduced with permission from ref 8. Copyright 2015 American Chemical Society. Reproduced with permission from ref 65. Copyright 2016 Elsevier. Reproduced with permission from ref 9. Copyright 2018 Wiley-VCH. Reproduced with permission from ref 41. Copyright 2019 Wiley-VCH. Reproduced with permission from ref 39. Copyright 2019 Wiley-VCH. Reproduced with permission from ref 44. Copyright 2023 Wiley-VCH. Reproduced with permission from ref 42. Copyright 2020 Wiley-VCH. Reproduced with permission from ref 54. Copyright 2021 IOP Publishing. Reproduced with permission from ref 45. Copyright 2023 Wiley-VCH.*

1.2.1 Synthesis

Once the concentration of the hydrocarbon gas exceeds a critical point during the

diamond growth process, a mixture of diamond and non-diamond carbon materials, namely DCs can be synthesized. For example, the augmenting of methane concentration led to the growth of diamond/graphite (Dia/Gr) composites.[52,53] The morphologies of these Dia/Gr composites (e.g., 3D-networks, nanoplatelets, nanowalls) were even tailorable, as confirmed from their SEM images (**Figure 1.2 a**), TEM images (**Figure 1.2 b**) as well as Raman spectra (**Figure 1.2 c**). Note that they were simply tunable through adjusting the growth parameters (e.g., flow rate of methane, growth temperature, and microwave power).[52,54]

Meanwhile, other components (e.g., carbides) have been introduced during the diamond CVD growth processes. This strategy was testified in 1992 for the first time for the synthesis of Dia/β-SiC composites. Inside a MPCVD reactor, methane and tetramethylsilane (TMS) were employed as the precursors to grow diamond and β-SiC phases, respectively. The variation of growth conditions (e.g., concentrations of gas precursors, power density, growth temperature) resulted in the growth of different Dia/β-SiC composites that featured different morphologies, crystal orientations, and phase concentrations.[6] A hydrogen-induced and selective growth model was further proposed to demonstrate the growth mechanisms of these Dia/β-SiC composites. Here, the key assumption is that only $-SiH_3$ and $-CH_3$ are stably bonded to β-SiC and diamond phases, respectively.[55-59] The non-stable SiH_3 species on the diamond phase and the non-stable CH_3 species on the β-SiC phase are immediately etched away by highly energetic hydrogen radicals. The surface is then re-saturated with H bonds. Such two successive processes lead to the formation of the Dia/β-SiC composites, as demonstrated from their SEM images (**Figure 1.2 d,e**), XRD patterns (**Figure 1.2 f**) and Raman spectra (**Figure 1.2 g**).[36]

Some alternative approaches have been presented to prepare other DCs, including the CVD growth of diamond on structured substrates, the cultivation of diamond on the surface of other materials, the continuous growth of other materials on top of diamond. For example, a porous boron-doped diamond/titanium carbide

(BDD/TiC) composite was synthesized using a plasma electrolytic oxidation (PEO)-treated titanium plate as the substrate, followed by the CVD diamond growth inside a MPCVD reactor.[60] In the patterned Dia/TiO_2 composites, the exposure ratio of diamond to TiO_2 was simply varied by altering the area/amount of the sputtered TiO_2 thin film on the diamond surface.[9] Vertically aligned carbon nanofibers (CNFs) were coated on a diamond film, where a nanometer-thick copper layer sputtered on the diamond surface acting as the catalyst for the thermal CVD growth of CNFs and acetylene was the precursor. The dimensions and densities of the CNFs were varied as a function of the features of the sputtered copper catalyst (e.g., thickness) and the growth parameters (e.g., growth duration and acetylene concentration).[8]

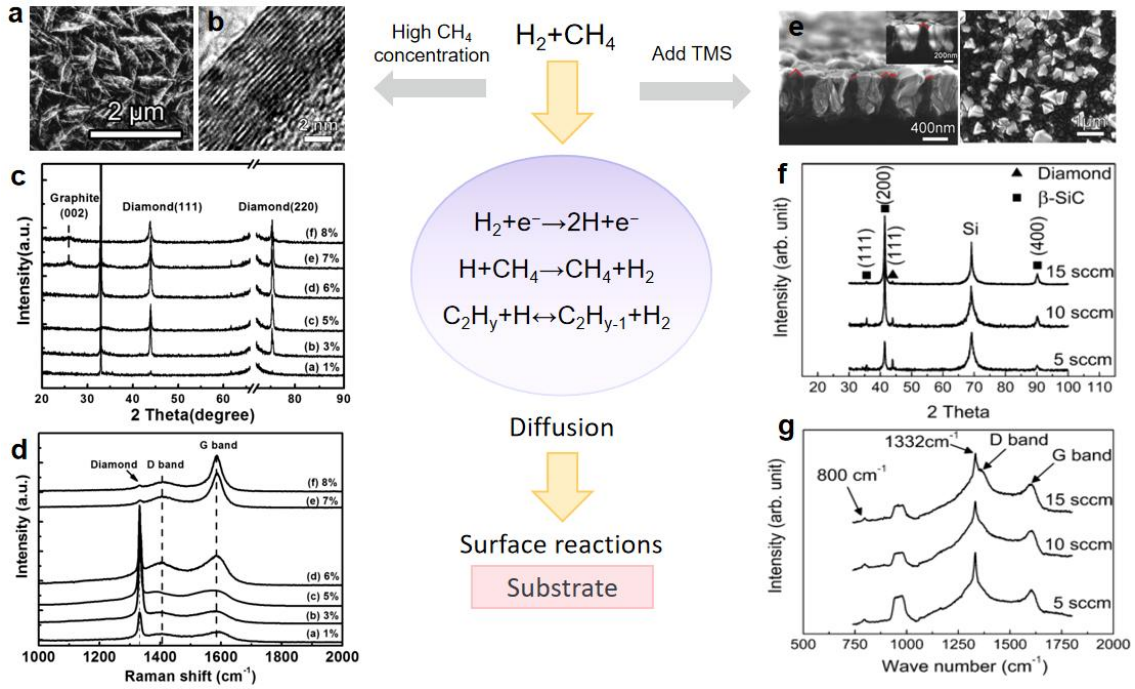


Figure 1.2 *Synthesis and characterization of Dia/Gr (a,b,c) and Dia/β-SiC (d,e,f,g) composites: (a) SEM and (b) TEM images, (c) XRD patterns and (d) Raman spectra of Dia/Gr composites; (e) SEM images, (f) XRD patterns and (g) Raman spectra of Dia/β-SiC composites. Reproduced with permission from ref 36. Copyright 2011 Elsevier. Reproduced with permission from ref 52. Copyright 2016 Elsevier.*

In addition, some methods in liquid phases were applied to prepare DCs. In most cases, the components (e.g., metals, polymers, and metal oxides) are directly

deposited onto the diamond surface using electrochemical deposition or chemical reactions. One recent example is electrochemical deposition of MnO_2 layers on the diamond surface, of which thicknesses were regulated by modulating the deposition times and the applied current densities.[8] The Dia/Pt composites were obtained through the electrodeposition of Pt particles on the diamond electrode surface.[61] The CuO@C/Dia and Dia/Gr composites have been produced *via* sputtering and electrochemical intercalation methods, respectively.[41,45]

1.2.2 Properties

The most important advance of these DC electrodes is that they remain the features of doped diamond materials, such as wide electrochemical potential windows, low background currents, long-term stability, and environmental benignity. Meanwhile, the properties of other components are fully integrated with those of diamond materials. Therefore, these DCs have been widely explored in the fields of electrosynthesis, electrocatalysis, electrochemical energy storage and conversion, electrochemical sensing, and other electrochemical devices. In the past years, DCs with diverse components such as Dia/CNF, porous Dia/TiC,[60] Dia/MnO_2,[62] Dia/Gr,[8] and Dia/TiO_2[42] have been frequently utilized as electrodes.

Electrochemical intercalation of sulfuric acid molecules or related ions into vertically aligned Dia/Gr composites, more precisely into graphene layers has been conducted at different voltages. Different intercalation voltages made these Dia/Gra composites exhibit varied volumetric capacitances (**Figure 1.3 a**). When the applied voltage were 1.4, 1.6, and 1.8 V, the capacitances of these Dia/Gra composites were 1.5, 6.7, and 16.5 mF cm^{-2}, respectively.[45] Their double layer capacitances of such expanded Dia/Gra composites were thus altered with the spacing of the expanded graphene layers or the sizes of the graphene channels.

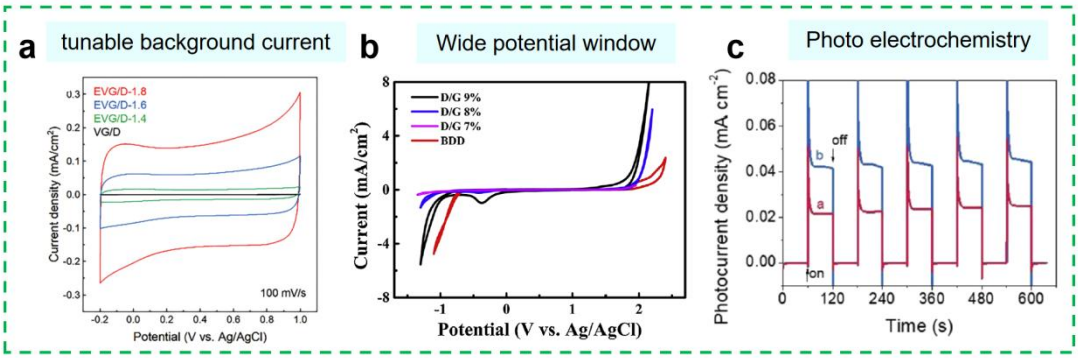


Figure 1.3 *Electrochemical properties of DCs: (a) The comparison of the cyclic voltammograms (CVs) of a BDD/Gra composite;*[45] *Reproduced with permission from ref 45. Copyright 2023 Wiley-VCH. (b) CVs of several Dia/Gr composites and a BDD film at 50 mV* s^{-1} *in 0.1 M* H_2SO_4;[65] *Reproduced with permission from ref 65. Copyright 2016 Elsevier. (c) Variation of photocurrent densities of. a* TiO_2*/BDD composite in 0.1 M* Na_2SO_4 *aqueous solution in the dark and under light irradiation.*[42] *Reproduced with permission from ref 42. Copyright 2020 Wiley-VCH.*

A wide potential window is the second feature of these DCs. Doped or conductive diamond and DC composites are believed to be superior to most electrodes. This is because the potential window of a working electrode is one of the key parameters in evaluating the electrochemical applications of an electrode.[63] For example, the potential window of a Dia/Gr composite that was fabricated with a methane concentration of 8% was about 3.1 V in 0.1 M H_2SO_4 when a current density of 0.9 mA cm^{-2} was selected as a turning point (**Figure 1.3 b**). This value is comparable to that of a BDD electrode and significantly wider than that of an exfoliated graphite electrode (~ 2.2 V).

In addition, DC composites exhibit high activities toward both inner-sphere $Fe(CN)_6^{3-/4-}$ and outer-sphere $Ru(NH_3)_6^{2+/3+}$ redox probes. Once DC composites and redox probes are changed, electrochemical response is varied accordingly.[23] Another example is in photoelectrochemical properties, a *p-n* heterojunction Dia/TiO_2 was synthesized using uniform patterns of a *p*-type BDD film and a *n*-type anatase TiO_2

film. The exposure ratios of the BDD patterns were varied to tune the photo-electrocatalytic abilities of this heterojunction. A heterojunction with a BDD exposure ratio of 20% exhibited a photocurrent density of 0.63 mA cm^{-2}, which is 2.86-fold higher than that obtained on a BDD film and 1.91-fold higher than that obtained on a TiO_2 film coated on a BDD film (**Figure 1.3 c**).[42]

1.2.3 Applications

1.2.3.1 Electrocatalysis

Some DCs have been employed as electrocatalysts for different catalytic reactions. For example, nitrogen-doped graphite/Dia (N-Gr/Dia) composites, composed of a thin nano-diamond layer at the bottom and vertically aligned multigraphene layers on the surface (**Figure 1.4 a**), have been treated by thermal annealing and then applied for the ORR. They exhibited superior ORR performance, namely a high onset potential of 835 mV (*vs*. standard hydrogen electrode, RHE) as well as excellent stability (e.g., 90% current retention even after an electrolysis time of 20 h). Their high performance was attributed to the activation and exposure of graphene edge sites along with the presence of a bonded nano diamond layer.[54] The Co_4N@Gr/Dia composites were further synthesized on carbon cloth (as the current collector). As bi-functional catalysts for both ORR and OER, they exhibited superior performance (**Figure 1.4 b**). The potential gap was as small as 0.75 V. They were further employed as air electrodes to assemble flexible zinc-air batteries, demonstrating an open circuit voltage of 1.41 V and excellent bending stability.[46]

1.2.3.2 Supercapacitors

Some DCs have been employed as the capacitor electrodes to improve the capacitances of diamond-based supercapacitors. This is because the component phase is possible to reduce the charge transfer resistance (R_{ct}) of the DCs, facilitating rapid ion and electron transportation.[6,64] For instance, a porous BDD/TiC electrode

delivered a specific capacitance of 46.3 mF cm^{-2} at 1 mA cm^{-2}, which was greater than that of individual TiC and BDD electrodes under identical conditions (**Figure 1.4 c**).[42] To fabricate supercapacitors with both high power- and energy- densities as well as large and stable capacitances, the Dia/CNFs composites were utilized as the capacitor electrodes. The assembled two-electrode symmetrical electrical double-layer capacitor (EDLC) and pseudocapacitor (PC) devices exhibited the capacitances of 30 and 48 mF cm^{-2} at 10 mV s^{-1}, respectively. Their power densities were 27.3 and 25.3 kW kg^{-1}, along with their energy densities of 22.9 and 44.1 Wh kg^{-1}, respectively (**Figure 1.4 d**).[9]

1.2.3.3 Photoelectrochemistry

Some DCs have been explored as the photoelectrodes for photo electrochemistry. A standard approach of utilizing a DC in photoelectrochemical applications involves the formation of a *p*-*n* composite or a heterojunction.[42] The typical example is to combine a *p*-type semiconductor (e.g., BDD) with a *n*-type semiconductor (e.g., TiO_2).[42] To adjust the photo-electrocatalytic abilities of this heterojunction, the exposure ratio of the BDD patterns on this heterojunction was varied. This is because the *p*-*n* heterojunction enhanced charge carrier separation and prevents recombination of electron-hole pairs (**Figure 1.4 e**). It completely degraded methyl orange within 4 h, following the application of a 2.5 V bias potential, while the degradation efficiency on the BDD film and the TiO_2 film was 56% and 45%, respectively. As confirmed by electron spin resonance spectroscopy, an accelerated production rate of •OH radicals were realized on this heterojunction. It originates from a synergistic effect between the BDD patterns that act as an ultra-microelectrode array with a TiO_2/BDD *p*-*n* heterojunction as well as facilitated charge separation in a lateral direction.

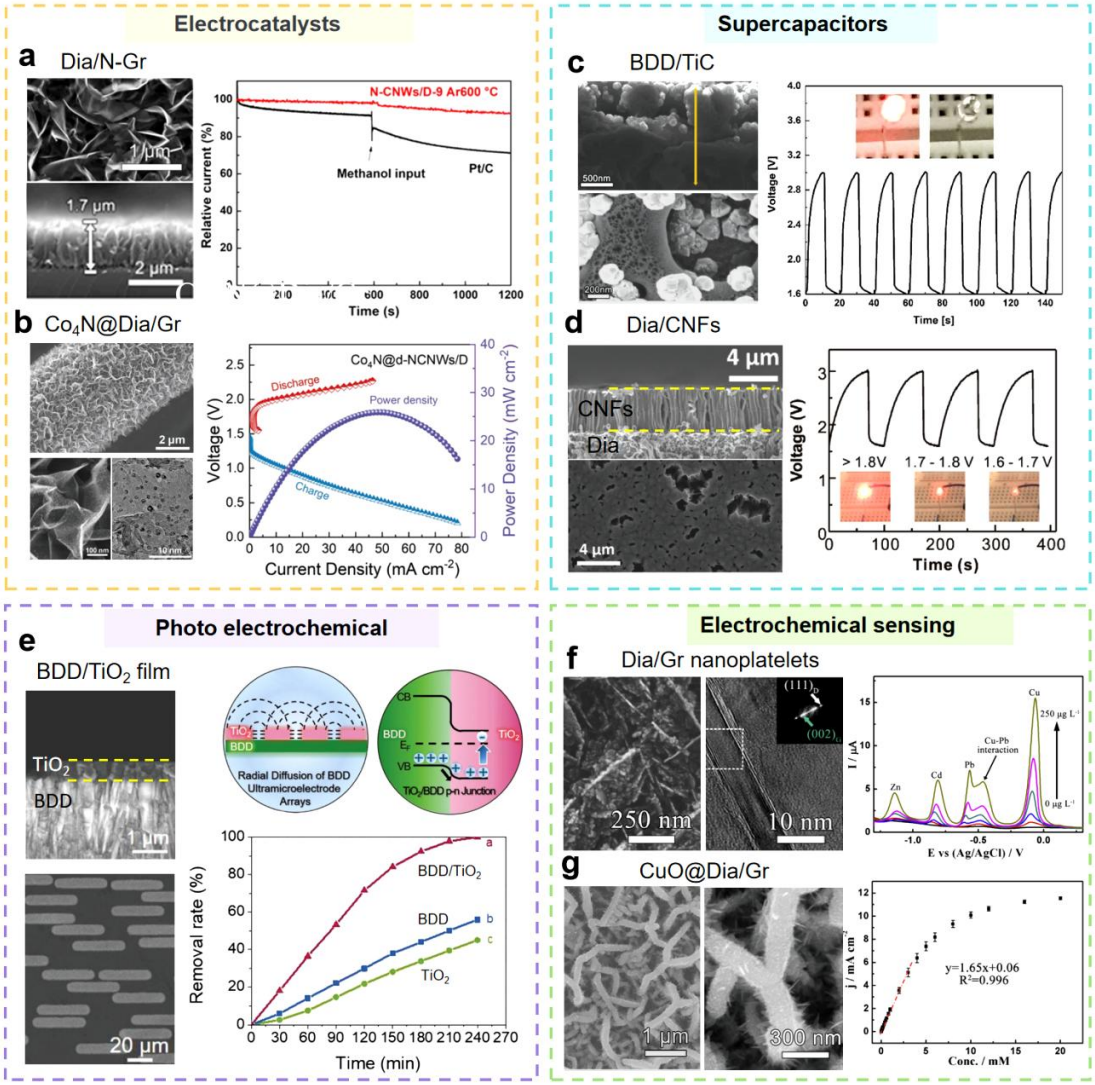


Figure 1.4 *(a) SEM images and schematic of N-Gr/Dia composite showing enhanced ORR performance.[54] Copyright 2021 IOP Publishing. (b) SEM/TEM images of Co_4N@Gr/Dia composite and its application in flexible zinc-air batteries.[44] Copyright 2023 Wiley-VCH. SEM images of (c) BDD/TiC and (d) CNF/BDD composites with supercapacitor performance.[60,9] Copyright 2018, 2019 Wiley-VCH. (e) SEM images, schematic of photoelectrochemical mechanism, and methyl blue degradation performance of TiO_2/BDD composite.[42] Copyright 2020 Wiley-VCH. (f) SEM/TEM images of Dia/Gr composite and its voltammogram for Zn(II), Cd(II), Pb(II), Cu(II) detection.[66] Copyright 2018 Elsevier. (g) SEM images of CuO@Gr/Dia composite and calibration curve for glucose detection.[41] Copyright 2019 Wiley-VCH.*

1.2.3.4 Electroanalysis

Some DCs have been applied as sensing materials for electrochemical detection of different soluble targets (e.g., heavy metal ions, biomolecules). Take Dia/Gr composites as an example, they exhibited higher sensitivity, wider linear ranges, more facile R_{ct} values and larger active areas than a BDD film. Therefore, these electrodes presented lower detection limits (LODs), wider linear ranges, better reproducibility, enhanced stability, and higher selectivity toward monitoring heavy metals ions (e.g., Ag^{+}, Zn^{2+}, Cd^{2+}, Pb^{2+} and Cu^{2+}).[65] The Dia/Gr composite exhibited superior performance toward simultaneous detection of Zn^{2+}, Cd^{2+}, Pb^{2+} and Cu^{2+} ions, including wide linear ranges (e.g., from 10 to 250 μg L^{-1}) and low LODs (**Figure 1.4 f**).[66] The rationally designed 3D-networked CuO@Gr/Dia composite was applied for the non-enzymatic detection of glucose, delivering a wide linear range, high sensitivity, and a low LOD, high selectivity, great long-term stability, and good reproducibility. The performance of this DC electrode was ascribed to the synergistic effect from highly electrocatalytic CuO nanoparticles and the 3D-networked conductive Dia/Gr composite (**Figure 1.4 g**). As an excellent transducer, this composite was believed to greatly accelerate the mass- and charge-transport kinetics of electrocatalytic reaction on the CuO biorecognition element.[41]

1.3 Motivation of the thesis

The motivation of this thesis stems from the need to address the limitations of traditional diamond-based materials and further to explore their seldom report new electrochemical applications. While diamond composites exhibit exceptional chemical and physical properties, their electrocatalytic performance is hindered by the limited number of active sites, which restricts their application in fields like energy storage, nitrate reduction, and further catalysis system. Diamond-based materials, though known for their high chemical stability and wide potential windows, often suffer from poor electrochemical performance due to insufficient surface reactivity and a lack of

efficient charge transfer pathways.

To overcome these challenges, this thesis focuses on enhancing the electrocatalytic activity of diamond-based materials through their co-doping using boron and nitrogen. By introducing two dopants, the number of active sites is expected to be increased tighter with improved electron transfer mechanisms, thereby unlocking the full potential of diamond composites in advanced electrochemical processes. Furthermore, the introduction of interlayers and surface post-treatment strategies is explored to optimize the structure and enhance the stability of the materials under electrochemical conditions.

Regarding electrochemical applications of these novel diamond composites, this thesis is driven by the growing demand for efficient, stable, and environmentally friendly materials, particularly in the fields of energy storage, pollution control, and sustainable energy generation. These approaches offer promising solutions to address the limitations of existing diamond composites and open up their new possibilities for the development of high-performance electrochemical devices.

1.4 Overview of the thesis

This thesis is divided into five sections and each focus on different aspects of the development and applications of BNDD films (based) electrodes:

Chapter 1 – Introduction - provides a background on diamond film electrodes and diamond composites. It introduces the concepts of diamond growth, doping techniques, and the specific challenges associated with boron and nitrogen co-doping. Additionally, this chapter outlines the motivation for the research and its focus on improving the electrochemical performance of diamond-based materials through novel interlayer and surface modification techniques.

Chapter 2 – Experimental - details the experimental techniques used in the synthesis and characterization of the BNDD materials. It covers various film synthesizing methods such as magnetron sputtering, electrodeposition, and MPCVD.

This chapter also outlines the preparation and characterization of synthesized materials. Focuses on the preparation of different diamond composites, including BNDD/Metal/Si, Cu_2O@CNF-BNDD, and partially covered BNDD with Ti/Si. The synthesis methods, structural analysis, and electrochemical characterization of each material are discussed in detail.

Chapter 3 - BNDD/Metal/Si Films - explores boron and nitrogen co-doped diamond (BNDD) films grown on Ti and Ti/Ta interlayers sputtered onto Si substrates using chemical vapor deposition (CVD). Characterizations (SEM, Raman, SIMS, XPS, EELS) confirmed the presence of C,O-doped TiN and TaC in the interlayers. Electrochemical evaluations in $[Fe(CN)_6]^{3-/4-}$ and $[Ru(NH_3)_6]^{3+/2+}$ systems showed superior performance for BNDD films on Ta/Ti/Si interlayers due to lower resistance, faster electron transfer, smaller particle size, and TaC presence. DFT calculations provided insights into interlayer effects on electronic properties.

Chapter 4 - Cu_2O@CNF-BNDD composites - designing, characterizing, and applying Cu_2O@CNF-BNDD composites as efficient catalysts for the electrochemical nitrate reduction reaction (NO_3RR) form the focus of this chapter. The Cu_2O@CNF-BNDD composite integrates the properties of BNDD films, carbon nanofibers (CNFs), and Cu_2O nanoparticles to significantly enhance NO_3RR performance. Building on these advancements, a Zn-NO_3^- battery system was proposed, showcasing dual functionality for energy generation and ammonia production.

Chapter 5 - BNDD/Ti/Si films - After conducting comprehensive characterizations of BNDD/Ti/Si anodes with varying coverage levels, the electrocatalytic performance of the integrated system was tested and evaluated. Coupling of anodic methyl orange oxidation and cathodic NO_3RR- building on the foundation of Chapter 4, which demonstrated the effectiveness of Cu_2O@CNF-BNDD composites for NO_3RR, this chapter introduces an integrated system where the oxygen evolution reaction (OER) is replaced with the

photo-electrocatalytic oxidation of methyl orange (MO). In this integrated system, NO_3RR is performed on a Cu_2O/CNF-BNDD cathode, while the photo-electrocatalytic oxidation of MO occurs on a BNDD/Ti/Si anode under light irradiation. Such a system achieves simultaneous nitrate reduction to ammonia and MO degradation, offering a multifunctional approach to address environmental challenges while producing valuable chemicals

Chapter 6 - Summary and Outlook - provides a comprehensive summary of the research findings and discusses the future outlook for diamond composites. It highlights the potential applications of these materials in various electrochemical fields and outlines possible directions for further research to improve the performance of diamond-based materials in advanced technologies.

Chapter 2. Experimental

2.1 Film deposition techniques

2.1.1 Magnetron sputtering physical vapor deposition

Magnetron sputtering, a form of physical vapor deposition (PVD) technique, involves the application of a magnetic field to enhance the rate at which particles are ejected from a cathode target.[67] This versatile method can be employed for the fabrication of various materials including metals, semiconductors, and insulators. It offers several advantages such as uncomplicated equipment setup, convenient control mechanisms, wide coating coverage, and excellent adhesion to substrates.[68]

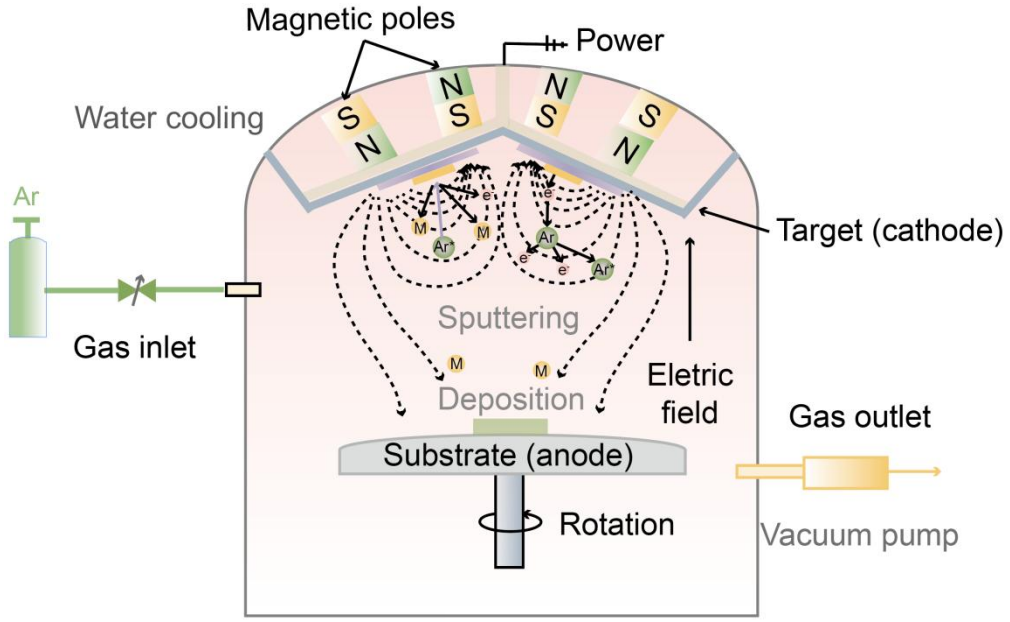


Figure 2.1 *Illustration of the magnet sputtering physical vapor deposition.*

During the deposition process, electrons interact with argon gas in an electrically charged environment, leading to the generation of Ar ions. These ions are then accelerated towards the cathode target where they collide with high energy causing sputtering. The neutral atoms released from this process are subsequently deposited onto a substrate while secondary electrons become excited and traverse circular paths on the target surface under electric and magnetic fields.[69] As they move along these

paths, they ionize numerous Ar ions before eventually losing their energy and falling onto the substrate **(Figure 2.1**). Consequently, magnetron sputtering is characterized by its ability to achieve high deposition rates even at low temperatures.

2.1.2 Electrodeposition

Electrodeposition refers to an electrochemical deposition process of a metal or alloy from an aqueous, non-aqueous solution, or molten salt compound.[70] Typically occurring within specific electrolytes and operating conditions within three-electrode systems (**Figure 2.2**), this process is influenced by various factors such as the deposited metal's properties, electrolyte composition and its pH level, temperature, current density, and other variables.[71] These factors collectively determine both the electrodeposition process and the morphology of the resulting deposit.[70,72]

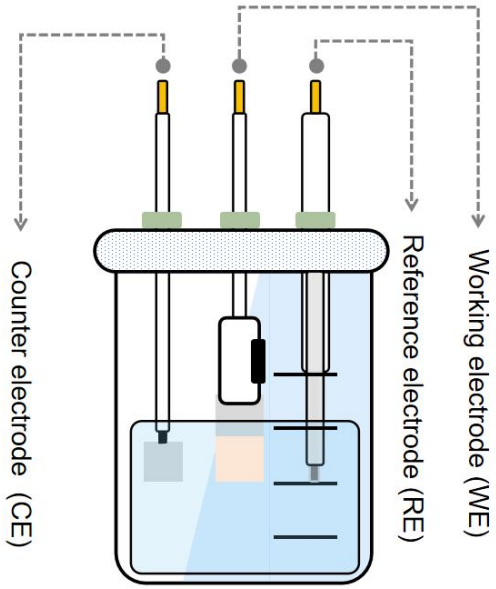


Figure 2.2 *Illustration of the electrodeposition in a three-electrode cell.*

2.1.3 Microwave plasma enhanced chemical vapor deposition

Microwave plasma enhanced/assisted chemical vapor deposition (MPCVD) has been widely used in diamond growth due to its ability to efficiently decompose carbon sources (e.g., methane) in the plasma and promote the deposition rates of

high-quality diamond films.[73] By generating plasma using microwaves, MPCVD allows for the growth of diamond films at relatively low temperatures, offering advantages over traditional high-pressure-high-temperature (HPHT) methods such as lower energy consumption and better temperature control. This technique enables uniform growth of diamond films on larger substrates, achieving high crystallinity and purity.[74] MPCVD has found to be extremely vital for extensive applications of diamond films, especially single crystalline ones, in the production of diamond-based electronic devices, optical components, and high-performance cutting tools.

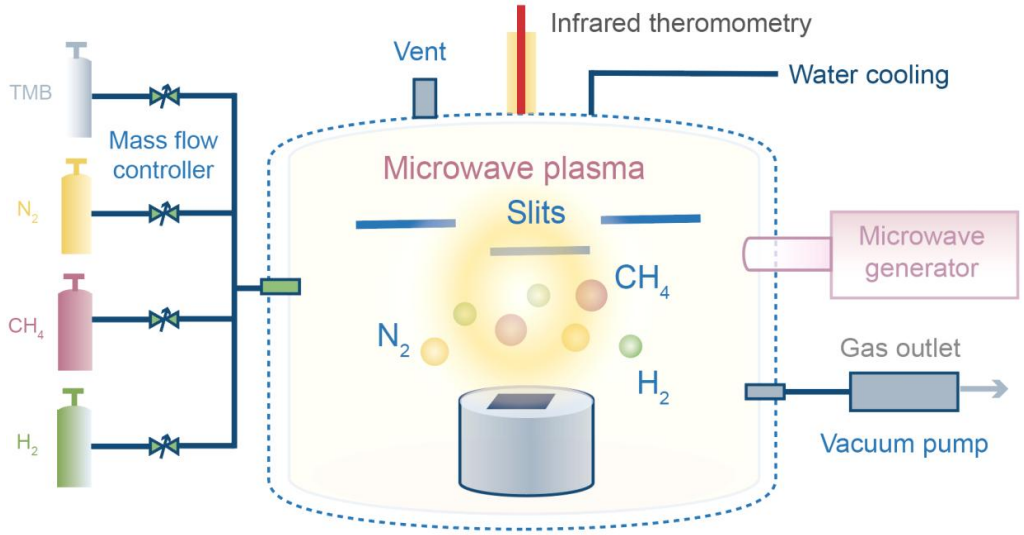


Figure 2.3 *Illustration of the microwave plasma chemical vapor deposition (MPCVD) of diamond films.*

2.2 Preparation

2.2.1 Preparation of BNDD/Metal/Si films

The synthetic procedure of BNDD/Metal/Si is illustrated in **Figure 2.4.** The detailed preparation process of each sample is described as follows:

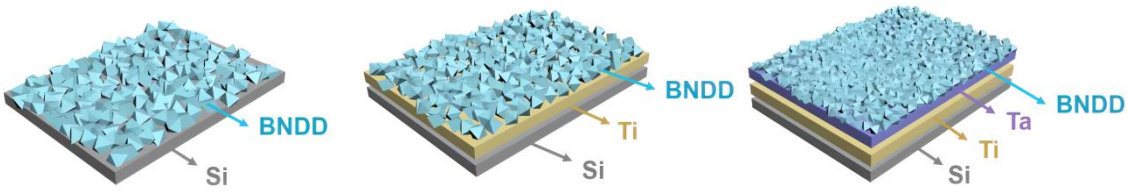


Figure 2.4 *Structure of BNDD films on different interlayers*.

Table 2.1 *Parameters of the metal sputtering*

Parameter	Ti	Ta
Base Pressure (10^{-6} mbar)	6.9	7.4
Working Pressure (10^{-3} mbar)	4.5	4.5
Power (W)	150	150
Voltage (V)	152.8	155.1
Current (A)	0.98	0.97
Ar Gas (sccm)	50	50
Time (min : s)	01:11	01:08

The thin metal interlayers on (100) oriented Si substrates were deposited by reactive direct current-pulsed magnetron sputtering. Prior to deposition, the substrates were exposed to oxygen plasma for the removal of surface contaminants. The sputtering targets were 4 inches in diameter, held on a water-cooled magnetron cathode. The distance between the target and the substrate holder was 10 cm. Before the deposition, targets were cleaned using argon gas discharge plasma for 5 min, followed by a pre- sputtering stage, using the same conditions as the subsequent film deposition with a shutter shielding the sample. The base pressure in the sputtering chamber was below 1×10^{-5} mbar, while the deposition pressure was kept at 4.5×10^{-3} mbar. **Table 2.1** shows the detailed parameters of the metal sputtering.

The BNDD films growth was carried out in an ASTeX 6500 series MWPCVD reactor. The growth temperature was monitored by a Williamson Pro92 dual-wavelength pyrometer. The CH_4, N_2, H_2, trimethyboron (TMB) was flown at a rate of 5, 10, 385, 100 sccm, respectively. Under such conditions, the nitrogen concentration was kept as 2%. A substrate temperature of 700 ℃ was induced by a

microwave power of 4000 W at a total pressure of 40 Torr. The CH_4, N_2, H_2, TMB (The TMB is diluted to 1000 ppm in H_2) was flown at a rate of 5, 10, 385, 100 sccm, respectively. This gas composition gives [B]/[C] = 20 000 ppm. Under such conditions, the nitrogen concentration was kept as 2%. A substrate temperature of 700 ℃ was induced by a microwave power of 4000 W at a total pressure of 40 Torr. The growth time of these BNDD films was 2 h.

2.2.2 Preparation of Cu_2O@CNF/BNDD composites

To solve low current density for the BNDD/Si, primarily due to low conductivity of a Si substrate, a Ta/Ti interlayer was introduced before diamond growth as it offers a higher electronic conductivity as well as more convenient control in diamond morphology. With a Ta interlayer, the as-synthesized Cu_2O@CNF/BNDD on Ta/Ti delivers significantly enhanced current response. Namely this metal interlayer is essential for the synthesis of high quality Cu_2O@CNF/BNDD.

2.2.2.1 CNF/BNDD films

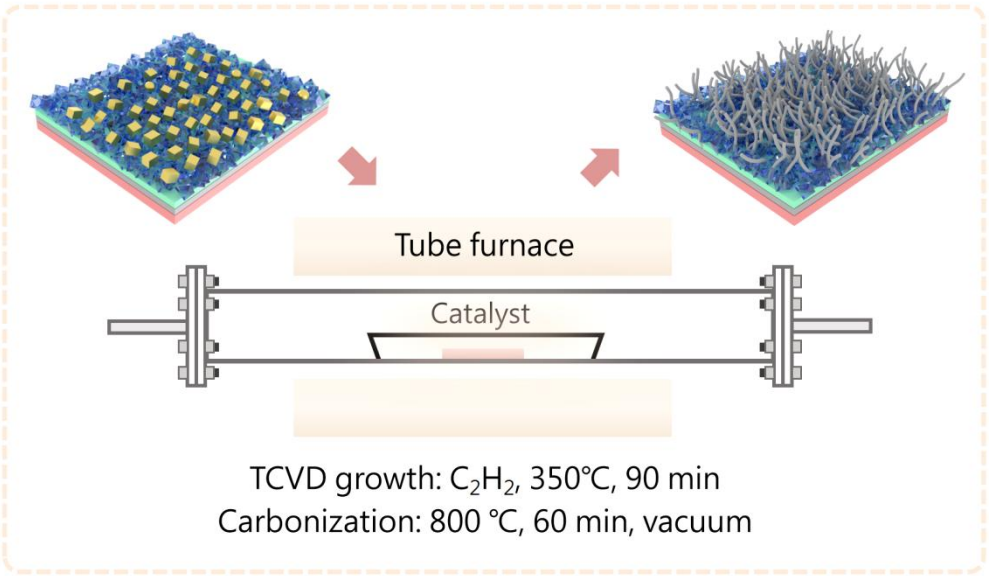


Figure 2.5 *Schematic plot of the synthesis of Cu@CNF/BNDD using a thermal chemical vapor deposition (TVCD) reactor.*

Figure 2.5 illustrates schematically the steps for the growth of Cu@CNF/BNDD hybrid films using a TCVD technique. The growth of CNFs was performed using Cu particles as the catalyst. The coating of BNDD with a thin copper film was realized with aid of an electrochemical deposition method at room temperature, where the as-prepared BNDD composites were utilized as the working electrode at room temperature. For electrodeposition, a three-electrode system was applied, consisting of an Ag/AgCl as the reference electrode and a platinum plate as the counter electrode. The used aqueous electrolytic bath contained 0.005 M copper sulfate ($Cu_2SO_4 \cdot 5H_2O$). The Cu-based nanoclusters were deposited at a fixed potential of -0.8 V (*vs.* Ag/AgCl) by means of chronoamperometry for 600 s. Subsequently, copper coated BNDD films were introduced in the center of a quartz tube in a TCVD device at a pressure of about 5×10^{-2} mbar and heated to 350 °C with a heating rate of 5 °C min^{-1}. After that the reaction gas of C_2H_2 was filled into the tube till a pressure of 600 mbar was reached and the CNF growth was conducted for 90 min. Once it was done, the reactor was rapidly evacuated till the pressure in the tube was lower than 5×10^{-2} mbar, when the carbonization of CNFs was then carried out. The carbonization temperature was 800 °C and the time applied was 60 min. Such a sample was finally cleaned with deionized water and dried in a N_2 atmosphere before the electrochemical experiments.

2.2.2.2 Cu_2O@CNF/BNDD films

The synthesis procedure and structure of Cu_2O@CNF-BNDD is illustrated in **Figure 2.6**. The Cu_2O nanocubes were further coated on the CNF/BNDD by means of an electrochemical deposition process at room temperature, where an as-prepared CNF/BNDD was utilized as the working electrode. For such experiments, a three-electrode system was applied, consisting of an Ag/AgCl reference electrode and a platinum plate counter electrode. In 0.005 M copper sulfate ($Cu_2SO_4 \cdot 5H_2O$), the Cu_2O nanoclusters were deposited at a constant potential of -0.8 V (*vs.* Ag/AgCl) by means of chronoamperometry for 300 s.

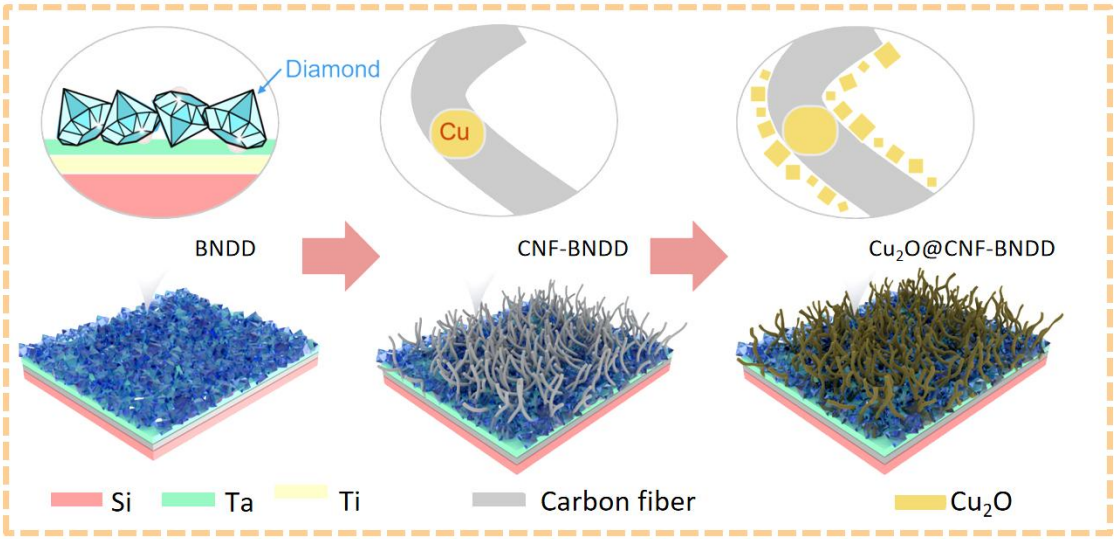


Figure 2.6 *Schematic illustration of the synthesis of BNDD composites films.*

2.2.3 Preparation of BNDD/Ti/Si films

2.2.3.1 Metal sputtering for Ti/Si substrate

Table 2.2 *Parameters of the metal sputtering*

Parameter	Ti
Base Pressure (10^{-7} mbar)	40-50
Working Pressure (10^{-3} mbar)	4.5
Power (W)	150
Ar Gas (sccm)	50
Time (min : s)	03:33

Fabrication of Ti layers on silicon substrates, the thin metal interlayers were deposited by reactive direct current-pulsed magnetron sputtering on (100) oriented Si substrates. Prior to deposition, the substrates were exposed to oxygen plasma to remove surface contaminants. The sputtering targets, 4 inches in diameter, were mounted on a water-cooled magnetron cathode. The distance between the target and

the substrate holder was 10 cm. Before deposition, the targets were cleaned using argon gas discharge plasma with the following parameters: Ar flow rate of 50 sccm, power of 150 W, pressure approximately 4.5 × 10^{-3} mbar, for a duration of 5 minutes. This was followed by a pre-sputtering stage and film deposition, with a deposition time of 3 minutes and 33 seconds. The base pressure in the sputtering chamber was approximately 4–5 × 10^{-6} mbar. **Table 2.2** shows the parameters for metal sputtering.

2.2.3.2 BNDD/Ti/Si

Table 2.3 *Parameters of the growth of BNDD films*

	BNDD/Ti/Si-1	**BNDD/Ti/Si-2**	**BNDD/Ti/Si-3**	**BNDD/Ti/Si-4**
H_2 (sccm)	385	385	385	385
CH_4 (sccm)	5	5	5	5
TMB (sccm)	100	100	100	100
N_2 (sccm)	10	10	10	10
Power (W)	4000	4000	4000	4000
Pressure (Torr)	40	40	40	40
Temp. (°C)	≈ 750	≈ 750	≈ 750	≈ 750
Duration	16 h 30 min	1 h 30 min	45 min	30 min

A series of BNDD films were grown on Ti/Si substrates with different coverage amounts of diamond nanoparticles, as shown in **Figure 2.7**. The growth of BNDD films was carried out in an ASTeX 6500 series MPCVD reactor. The growth temperature was monitored by a Williamson Pro92 dual-wavelength pyrometer. The CH_4, N_2, H_2, trimethyboron (TMB) was flown at a rate of 5, 10, 385, 100 sccm, respectively. Under such conditions, the nitrogen concentration was kept as 2%. A

substrate temperature of 750 ℃ was induced by a microwave power of 4000 W at a total pressure of 40 Torr. The diamond coverage on the Ti layer surface was controlled by varying the growth time, with the first sample being unseeded, meaning no diamond nanoparticles were present on its surface. **Table 2.3** shows the detailed parameters for the grow the of BNDD films.

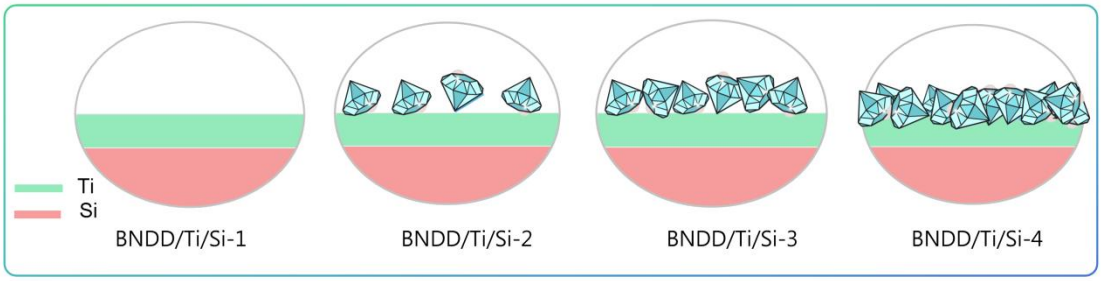


Figure 2.7 *Schematic illustration of the BNDD films with different coverages on a Ti/Si substrate.*

2.3 Characterization

2.3.1 Morphology and physical structure characterization

2.3.1.1 Scanning electron microscopy (SEM)

Scanning electron microscopy (SEM) is a technique used to visualize the surface morphology of materials at high resolution. It works by scanning a focused beam of electrons over the surface of a sample, producing signals that contain information about the sample's topography and composition. In this thesis, the surface morphology of the synthesized composites films was characterized in this thesis by means of a field emission scanning electron microscope with Inlens mode (FE-SEM, Zeiss ultra55, Germany). The acceleration voltage of the electron gun was varied from 5 to 10 kV, which was selected to optimize the clarity of the surface details while minimizing potential distortion, enabling comprehensive surface analysis of the composite films.

2.3.1.2 Scanning transmission electron microscopy - electron energy loss spectroscopy (STEM-EELS)

Scanning transmission electron microscopy (STEM) combined with electron energy loss spectroscopy (EELS) is a highly advanced analytical technique that provides both structural and compositional information at the atomic scale. STEM operates by focusing a high-energy electron beam onto a sample and detecting the scattered electrons, while EELS analyzes the energy lost by electrons as they interact with the sample, providing insights into the material's elemental composition and chemical bonding states. The microstructures of the BNDD films with different interlayers were examined using a Thermofisher Titan ThemisZ microscope operating at 60 kV. The convergence and collection angle for STEM-EELS was set to 16 and 40 mrad, respectively. The dispersion was 170 meV pixel^{-1} and the energy spread of the incoming electrons was 700 meV. Low and core loss were acquired almost instantaneously with a dwell time of 20 ms and incoming electron current of 30 pA. Model based fitting procedure[75] was used to extract the elemental maps where a linear background model was used[76] and the core-loss edges were modelled using the atomic cross sections.[77]

2.3.1.3 Micro-X-ray diffraction

Micro-X-ray diffraction (Micro-XRD) is used to study the crystal structures, phases, and orientations of materials. The method works by directing a focused X-ray beam onto a material and analyzing the resulting diffraction patterns, which reveal information about the atomic arrangement and phase composition. Its high spatial resolution makes it particularly suitable for characterizing small or heterogeneous samples. The physical phases of the investigated materials were confirmed by micro-X-ray diffraction (Micro-XRD, Bruker D8 Discover, Billerica, MA, USA), equipped with a Co Ka1 radiation source (λ = 1.78897 Å) in that micro-XRD is a widely used technique for analyzing the crystal structures of materials. By examining

the diffraction patterns obtained from the sample, its phases and crystalline structure can be precisely identified. In this thesis, the instrument employed a Co Ka1 radiation source with a wavelength of 1.78897 Å, which provides high-resolution diffraction data essential for accurate phase analysis.

2.3.2 Surface chemistry analysis

2.3.2.1 Raman spectroscopy

Raman spectroscopy is a non-invasive spectroscopic method widely employed for discerning the vibrational modes of molecules. This technique provides valuable insights into various aspects such as distinguishing between sp^2 and sp^3 phases in carbon-based materials, identifying dopants, characterizing dangling bonds, and revealing distinct "fingerprints" of transition metal compounds. In this thesis, the Raman spectra of the studied films were collected by use of a homemade Raman microscope around an inverted microscope (Nikon TE300, objective lenses from Nikon and optical Filters from AHF Analysentechnik) equipped with a 532-nm laser (Coherent Compass 315M-100, 100 mW output power) as an excitation source, a monochromator (Jobin Yvon, TRIAX 320, with a 1200 l/mm grating) and a spectroscopic back illuminated EMCCD camera (Oxford Instruments Andor, Newton EMCCD DU970P) as a detection unit.

2.3.2.2 X-ray photoelectron spectroscopy (XPS)

X-ray photoelectron spectroscopy (XPS) is a surface-sensitive analytical technique used to determine the chemical composition, oxidation states, and electronic structure of materials. XPS operates by irradiating a material's surface with X-rays, causing photoelectrons to be emitted. By analyzing the energy of these photoelectrons, detailed information about the material's surface chemistry can be obtained, typically to a depth of $1-10$ nm. The surface analysis of these as-grown diamond films was conducted using X-ray photoelectron spectroscopy (XPS)

(S-probe ESCA SSX-100s, Surface Science Instruments, USA) with Al Kα radiation of 200 W. The XPS spectra were recorded from 0 to 1200 eV with a resolution of 1 eV and a spot size of 800 μm^2. The high-resolution XPS spectra were collected with a 0.1 eV resolution at a spot size of 300 μm^2.

2.3.2.3 Time-of-flight secondary ion mass spectrometry (ToF-SIMS)

A time-of-flight secondary ion mass spectrometer (ToF-SIMS IV, ION-TOF GmbH, Germany) was used to map the dopants in diamond films in the positive mode, such as the contents of nitrogen and boron atoms in the BNDD films. Its works by bombarding the surface with a focused primary ion beam, causing the ejection of secondary ions. These ions are then analyzed based on their mass-to-charge ratio using a time-of-flight mass analyzer, enabling both qualitative and quantitative analysis. For these mapping experiments, a 25 keV Bi^+ primary ion beam was used to bombard the diamond surface within an area of 300 × 300 μm^2 after 1200 s sputtering.

2.3.2.4 Ultraviolet–visible spectroscopy

Ultraviolet spectroscopy or ultraviolet-visible (UV-vis) spectrophotometry is a technique used in analytical chemistry and biochemistry for determining the concentration of a substance. UV spectroscopy typically involves shining UV or visible light through a sample and measuring the intensity of light that passes through it. By comparing the intensity of incident light with the intensity of transmitted light, which determines the amount of light absorbed by the sample. This absorption is due to electronic transitions within molecules, where electrons move from lower to higher energy levels.

2.3.3 Electrochemical characterization

In this thesis, various electrochemical techniques including cyclic voltammetry (CV), linear sweep voltammetry (LSV), impedance spectroscopy (EIS), Galvanostatic

charge and discharge (GCD), chronoamperometry (or *i-t* curve), as well as chronopotentiometry (CP) were utilized to explore electrochemical properties of synthesized composites and films, along with their special electrochemical performance. The measurement system employed for these electrochemical analyses comprised an integrated setup, consisting of a potentiostat, a current-voltage converter, and a data acquisition system. The used electrolysis cell consisted of four components: a working electrode, a counter electrode, a reference electrode, and an electrolyte.

2.2.4.1 Linear sweep voltammetry (LSV)

Linear sweep voltammetry (LSV) is a method where the current at a working electrode is measured while its potential (*vs*. a reference electrode) changes linearly over time.[78] When a substance starts to be oxidized or reduced, it shows up as an anodic/cathodic peak/wave or trough in the current signal. Compared with cylic voltammetry (CV), LSV is generally conducted at low scan rates (V s^{-1}) to ensure the static surface properties during the redox processes.

2.2.4.2 Cyclic voltammetry (CV)

Cyclic voltammetry (CV) is a type of measurements where the potential of a working electrode changes over time.[79] CV is commonly used to study electrochemical properties of substances in solutions or molecules attached to the electrode.[80] In this thesis, the potential was increased linearly until a set point was reached and then reversed to return to the starting point. These cycles were repeated as necessary. The current at the working electrode was plotted against the applied voltage to create a cyclic voltammogram.

2.2.4.3 Electrochemical impedance spectroscopy (EIS)

Electrochemical impedance spectroscopy (EIS) is a highly sensitive electrochemical technique to establish electrical response of electrode systems.[81] EIS

measures the time-dependent response of an electrode system by applying low-amplitude alternating current (AC) voltages across a range of frequencies. Quantitative measurements are possible using EIS and also enable the evaluation of small-scale chemical mechanisms at the electrode/electrolyte interface. In this thesis, EIS was used to investigate the reaction kinetics, charge transfer resistances, and double-layer capacitances of the synthesized catalysts.

2.2.4.4 Galvanostatic charge/discharge (GCD)

Galvanostatic charge/discharge (GCD) method is frequently used to study the charge and discharge processes of batteries, supercapacitors, and other energy storage devices.[82] In GCD experiments, a constant current is applied to the studied device, and the resulting voltage or potential response is monitored as a function of time. During the charge process, a constant current is applied to the device, leading to the accumulation of charges within an energy storage material (e.g., ions being intercalated into an electrode material in a battery). This results in an increase in voltage or potential across the device. During the discharge process, the stored energy is released as the device is allowed to discharge through an external circuit. A constant current is again applied, but this time it flows out of the device, causing the voltage or potential to decrease as the stored charge is depleted.

2.2.4.5 Chronoamperometry

Chronoamperometry (CA), also known as time-based amperometry or current-time (*i-t*) curves, is an electrochemical technique used to monitor the current response at a working electrode as a function of time under a constant applied potential. In CA experiments, a fixed potential is applied to the working electrode, and the resulting current is measured continuously or at specific time intervals.[83] This technique is particularly useful for studying the kinetics of electrochemical reactions, including redox reactions and catalytic processes. By monitoring the current as a

function of time, one can gain insights into reaction mechanisms, reaction rates, and the behavior of electrode surfaces. CA is commonly used in various applications, especially for catalysis, electrodeposition and electrosynthesis studies. Overall, CA is a valuable tool in electrochemical research and has been widely employed for studying reaction kinetics, characterizing electrode materials, and optimizing electrochemical processes.

2.2.4.6 Chronopotentiometry (CP)

Chronopotentiometry (CP) is an electrochemical technique that involves applying a constant current to an electrochemical cell and monitoring the resulting changes in potential over time.[84] Unlike CA where the potential is held constant and the current is measured, in CP tests the current is held constant while the potential is monitored. The CP method provides information about the resistance of an electrochemical cell, the kinetics of electrode reactions, and the transport properties of ions in solutions. It has been commonly harnessed in various fields, including electrochemistry, materials science, and corrosion engineering, studies/optimization of electrochemical processes.

2.4 Performance measurements of electrochemical devices

2.4.1 Supercapacitors using the BNDD films

Table 2.4 *The chemical compositions of the electrolytes.*

Supercapacitor	Chemical composition of electrolytes
EDLC	1 M Na_2SO_4
PC	0.05 M $Fe(CN)_6^{3-/4-}$ + 1.0 M Na_2SO_4

Based on their working mechanisms, supercapacitors or electrochemical capacitors can be broadly classified into two categories: electric double layer

capacitor (EDLC) and pseudocapacitor (PC). An EDLC operates by forming an electrical double layer at the interfaces between a capacitor electrode and an electrolyte. This process involves the electrostatic adsorption of ions from the electrolyte onto the active electrode surface, resulting in double-layer charge storage. In contrast, a PC involves Faradaic reactions of redox species either coated on the capacitor electrodes or dissolved in the electrolyte solutions.

For the supercapacitors in this thesis their electrochemical measurements were carried out on a CHI 660E workstation (Shanghai Chenhua Company, China). In the first step, a classic three-electrodes system was applied, where the reference electrode was an Ag/AgCl electrode, the counter electrode was a Pt wire, and the working electrode was the BNDD film (BNDD/Si, BNDD/Ti/Si, and BNDD/Ta/Ti/Si). The geometric area of the working electrode was 0.05 cm^2. To investigate the performance of electrochemical capacitors from fabricated BNDD films, electrochemical technique such as CV, GCD and EIS method were employed. The cyclic voltammograms (CVs) and GCD curves of the BNDD/Si, BNDD/Ti/Si, or BNDD/Ta/Ti/Si film-based capacitor electrodes were recorded in were recorded in different solutions (**Table 2.4**). For the construction of diamond-based EDLCs and PCs, a three-electrodes system in 1.0 M Na_2SO_4 and 1.0 M Na_2SO_4 containing 0.05 M $K_3Fe(CN)_6/K_4Fe(CN)_6$ aqueous solutions were employed, respectively. Their performance was evaluated through CV at various scan rates, the GCD method at different current densities, and EIS technique at open circuit potentials within the frequency range of 0.01 to 10^6 Hz.

2.4.2 Electrocatalytic nitrate reduction reactions

Electrochemical performance of the NO_3RR were measured using a CHI 660E electrochemical workstation (Chenhua, Shanghai) within an H-type electrolytic cell configuration (**Figure 2.8**). The electrolytic cell was partitioned by a Nafion 117 membrane. The working electrode, reference electrode, and counter electrode were the synthesized diamond composite, an Ag/AgCl electrode, and a platinum plate,

respectively. The geometric surface area of the working electrode was 0.5 cm^2.

A 0.5 M Na_2SO_4 solution (100 mL) was evenly distributed between the cathode and anode cells. $NaNO_3$ was introduced into the cathode cell at a concentration of 100 mg/L NO_3^--N (NO_3^--N refers to the mass of nitrogen present in the nitrate). All potentials were referenced against the reversible hydrogen electrode (RHE). Prior to the NO_3RR test, linear sweep voltammogram were recorded until the polarization curves reached a steady state. Such a linear sweep voltammogram were recorded at a scan rate of 2 mV s^{-1}, ranging from -0.2 to -1.6 V (vs. RHE). Subsequently, *i-t* curves were conducted at various potentials for 2 h with a stirring rate of 500 rpm min^{-1}.

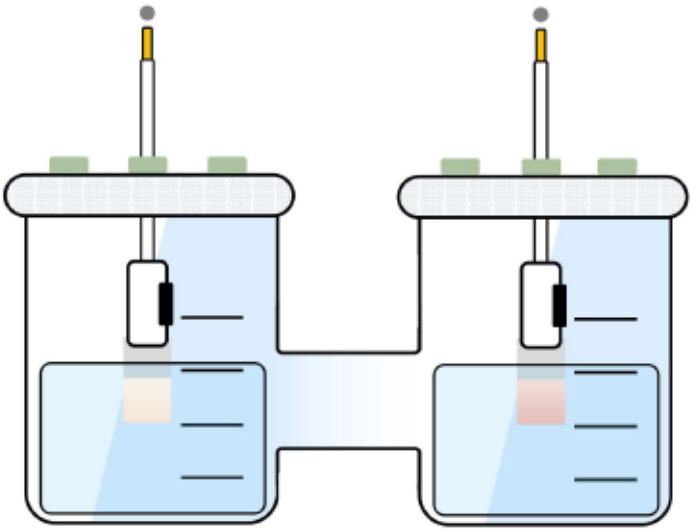


Figure 2.8 *Schematic illustration of a multi-function electrochemical system.*

2.4.2.2 Calculation of the nitrate conversion, selectivity, the yield of ammonia and Faradaic efficiency

For the NO_3RR, the nitrate conversion was calculated using the equation of:

$$Conversion = \frac{\Delta c_{NO_3^-}}{c_0} \times 100\% \quad (2.1)$$

The yield of ammonia was calculated by the equation of:

$$Yield_{NH_3} = \frac{c_{NH_3} \times V}{M_{NH_3} \times t \times S} \quad (2.2)$$

The Faradaic efficiency was defined by:

$$FE = \frac{8F \times c_{NH_3} \times V}{M_{NH_3} \times Q} \quad (2.3)$$

where $\Delta c_{NO_3^-}$ is the concentration difference of NO_3^- before and after the NO_3RR test, c_0 is the initial concentration of NO_3^-, c is the produced concentration of ammonia or nitrite. c_{NH_3} is the concentration of $NH_{3(aq)}$, V (= 100 mL) is the volume of the electrolyte in the cathode cell, M_{NH_3} is the molar amount of NH_3, t (= 2 h) is the synthesis time, S (= 0.5 cm^2) is the geometric area of the working electrode. F (= 96485 C mol^{-1}) is the Faradaic constant, Q is the total charge passing the electrode, which was calculated as the area integral of the *i-t* curve.

2.4.3 Electrocatalysts and photoelectrocatalysts

2.4.3.1 Photoelectrochemical degradation

Photoelectrochemical cell is one of the key components of a photoelectrochemical system. The used photoelectrochemical cell in this thesis was based on a conventional electrochemical H-type cell. It was fabricated from UV-grade fused silica that it is transparent in the entire range from UV to near-IR (namely from 200 nm to 2.2 mm). The volume of this photoelectrochemical cell was designed as 15 ml for both cathode and anode. For easy handling, a detachable sample insert was designed for sample mounting. The electrical contact to the sample surface was made with a platinum plate. The space at the bottom of the cell was accommodated a small magnetic stir.

The ultimate test for a photoelectrochemical device or a photoelectrode was performed under light irradiation at a dentistry of 1 mW cm^{-2}. Since light source is known to be another key component of a photoelectrochemical measurement setup, **Figure 2.2** overviews the main components of the photoelectrochemical setup used in this thesis. The light source is a 150 W Xenon lamp coupled with a monochromator (MSH-300, LOT-Quantum Design GmbH), which was used to transmits a mechanically selectable narrow band of wavelengths. An optical lens was used to

properly focus the light onto the sample. The potential of the sample was again controlled by a CHI 660E electrochemical analyzer, which also measured the current.

The photocurrents were measured under different initial voltages or while sweeping the potential at a constant scan rate. The current-voltage measurements were conducted in dark, under constant illumination, as well as by switching the illumination on or off at a fixed frequency. In this thesis, various techniques such as CV, EIS, LSV and amperometry (*i-t* curves) were employed to analyze the photoelectrochemical performance of a Ti/Si substrate without BNDD, a BNDD film fully covered on a Ti/Si film, partially covered BNDD composite films (BNDD/Ti/Si).

The application of the BNDD/Ti/Si for photoelectrocatalytic degradation of methyl orange (MO) was explored. The degradation experiments were conducted in a photoelectrochemical cell with a 5 mL of 10 mg L^{-1} MO dissolved in 0.5 M Na_2SO_4. Besides an anode/working electrode from a BNDD/Ti/Si composite film, an Ag/AgCl reference electrode, a Pt wire was used as counter electrode in the cathode compartment. The light source was the same as that above mentioned for other photoelectrochemical measurements. All degradations were carried out with a basis voltage of 2.8 V using a CHI 660E electrochemical analyzer.

The MO concentration was detected by a UV-visible spectrophotometer (CARY, 50 Bio). The characteristic peak of MO at $\lambda = 464.5$ nm was quantitatively measured and employed to estimate the removal of MO. The removed fraction (η) was calculated using Eq. (2.4).

$$\eta = \frac{A_0 - A_t}{A_0} \times 100\% \qquad (2.4)$$

where A_0 and A_t are the absorbance intensity of MO at the initial stage and the given time t, respectively.

2.4.3.2 Photoelectrochemical coupling: nitrate reduction and dye degradation

An integrated photo-electrochemical cell was constructed to couple nitrate

reduction with dye degradation. It consists of two compartments. In the cathodic compartment, Cu_2O/CNF-BNDD serves as the electrocatalyst to facilitate the electrochemical reduction of nitrate (NO_3^-) to ammonia (NH_3), with an electrolyte containing 0.5 M Na_2SO_4 and 100 mg L^{-1} NO_3^--N. In the anodic compartment, a BNDD electrode performs the photoelectrocatalytic oxidation of methyl orange (MO) under light irradiation, with an electrolyte of 0.5 M Na_2SO_4 and 50 mg L^{-1} MO. The two compartments are separated by a Nafion 117 membrane that allows selective ion exchange. (**Figure 2.9**)

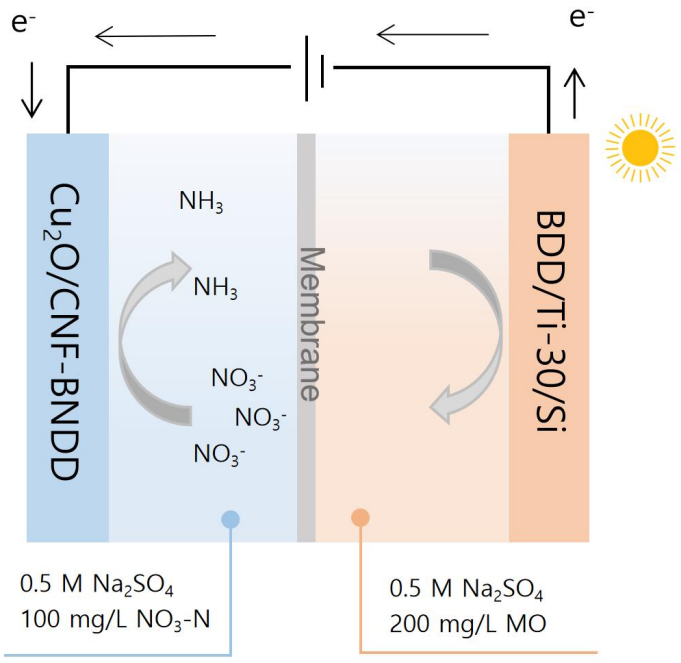


Figure 2.9 *Schematic illustration of a NO_3RR-MO system.*

2.4.4 Assembly of a zinc-nitrate battery

The electrochemical reactions in a Zn-nitrate battery are assumed as following:

Discharge: $4Zn + NO_3^- + 7H_2O + 6OH^- \rightarrow 4Zn(OH)_4^{2-} + NH_4^+$

Charge: $2Zn(OH)_4^{2-} \rightarrow 2Zn + 2H_2O + 4OH^- + O_2$

Overall reaction: $NO_3^- + 3H_2O \rightarrow NH_4^+ + 2OH^- + 2O_2$

To assemble such a zinc-nitrate battery, a Cu_2O@CNF/BNDD film (1×0.5 cm^2) was employed as the cathode and a Zn plate (1×2 cm^2) as the anode (**Figure 2.10**). A

typical H-type cell that contains 100 mL cathode electrolyte (0.5 M Na_2SO_4 + 100 mg L^{-1} NO_3^--N) and 100 mL anode electrolyte (3 M KOH) was separated by a bipolar membrane (Nafion 117). The discharging polarization curves with a scan rate of 5 mV s^{-1} and chronopotentiometric tests were conducted using a CHI 660E workstation at room temperature. After electrochemical test, the electrolyte was diluted for the next detection.

The power density (P) of this zinc-nitrate battery was determined by $P = I \times V$, where I and V are the discharge current density and voltage, respectively.

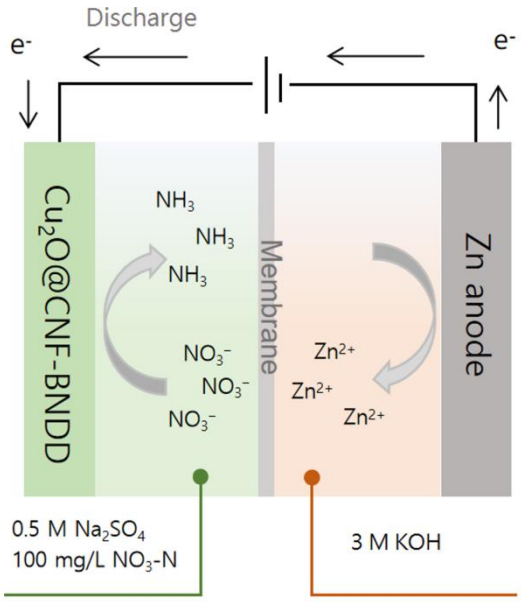


Figure 2.10 *Schematic illustration of the Zn-NO_3^- battery.*

2.5 Ion detection

The UV-vis spectroscopy encompasses absorption or reflectance spectroscopy within the ultraviolet and adjacent visible regions of the electromagnetic spectrum. Due to its cost-effectiveness and ease of use, this technique finds extensive applications in analytical chemistry for the quantitative determination of various analytes. In this thesis, UV-vis spectroscopy was utilized to quantitatively analyze concentrations of pre- and post-test reduction electrolytes, through dilution to match the calibration curve range for specific detection methods (0.5 M Na_2SO_4 solution was

used as the baseline), as outlined below:

2.5.1 Determination of NO_3^--N

The concentration of the NO_3^--N was determined by the following procedure:

In the first step, two reagents were prepared: The reagent (A): 8.3 mL of HCl was diluted to 100 mL to prepare 1 M HCl solution. The reagent (B): 0.8 g of NH_2SO_3H was added into 100 mL distilled water to prepare a 0.8 wt% solution.

Then, a standard NO_3^--N solution was prepared to calibrate concentration and absorbance curves were drawn using the following solutions:

a) 1000 mg L^{-1} NO_3^--N of 0.5 M Na_2SO_4 solution: 0.6071 g $NaNO_3$ was first dried in the oven for 2 h, and then dissolved to 100 ml 0.5 M Na_2SO_4. To prepare different standard solutions, the 1000 ppm NO_3^--N solution was diluted to different concentrations.

b) 100 mg L^{-1} NO_3^--N in 0.5 M Na_2SO_4 solution: 10 mL of the prepared 1000 mg L^{-1} NO_3^--N was diluted to 100 mL by adding 0.5 M Na_2SO_4 solution.

c) 2 mg L^{-1} NO_3^--N in 0.5 M Na_2SO_4 solution: 2 mL of the prepared 100 mg L^{-1} NO_3^--N was diluted to 100 mL by adding 0.5 M Na_2SO_4 solution.

d) Standard solutions: 0, 4, 6, 8, 10, 12, 14, 18 and 20 mL of the prepared 2 mg L^{-1} NO_3^--N were diluted to 20 mL by adding 0.5 M Na_2SO_4 solution respectively. And then 0, 0,4, 0.6, 0.8, 1.0, 1.2, 1.4, 1.6, 1.8 and 2.0 mg L^{-1} NO_3^--N standard solutions were obtained.

The experiments of NO_3^--N determination were carried out as following: 0.2 mL reagent (A) and 0.02 mL reagent (B) were added into 10 mL of the standard solutions stepwisely. After placing the mixed solution in a dark environment for 20 min, UV-vis spectra were recorded (the final absorbance= A (220 nm) - 2A (275 nm)). The concentration of the NO_3^--N in the electrolyte was also detected by the same method in the experiments, 0.2 mL of electrolyte was collected from the cathode cell and diluted to 10 mL to reach the detection range. The ultraviolet absorption and

absorbance-concentration curve was calibrated using a series of standard sodium nitrate solutions (**Figure 2.11**).

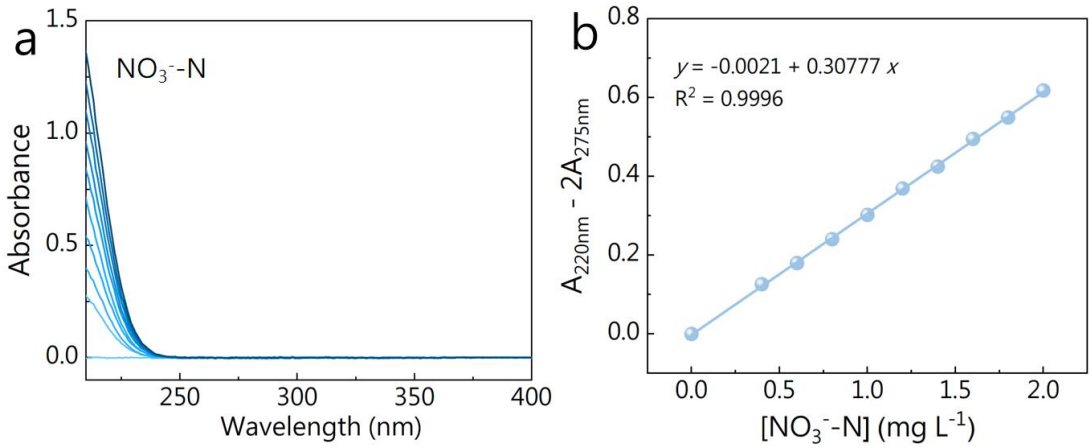


Figure 2.11 *The ultraviolet absorption spectra (a) and the absorbance-concentration calibration curve (b) of NO_3^-N. The fitting curve shows that the relationship between the absorbance, y (= A (220 nm) - 2A (270 nm)) and the concentration of NO_3^-, x, is in good linear relation and follows (y = -0.0021 + 0.30777x, R^2=0.9996)*

2.5.2 Determination of NO_2^--N

The concentration of the NO_2^--N was determined by the following procedure:

The color reagent was prepared by adding 5 g $C_6H_8N_2O_2S$ to a mixed solution of 50 ml water and 10 ml phosphoric acid where 0.2 g $C_{12}H_{14}N_2 \cdot 2HCl$ was dissolved. The resultant solution was finally diluted to 100 mL using distilled water.

The NO_2^--N standard solution was prepared to calibrate the concentration and absorbance curves of nitrite (NO_2^-) by the following procedure:

a) 1000 mg L^{-1} NO_2^--N of 0.5 M Na_2SO_4 solution: 0.4929 g $NaNO_2$ was first dried in the glass dryer for 2 h, and then dissolved to 100 mL 0.5 M Na_2SO_4.

b) 10 mg L^{-1} NO_2^--N in 0.5 M Na_2SO_4: 1 mL of the prepared 1000 mg L^{-1} NO_2^--N was diluted to 100 mL by adding 0.5 M Na_2SO_4 solution.

c) 1 mg L^{-1} NO_2^--N in 0.5 M Na_2SO_4: 10 mL of the prepared 10 mg L^{-1} NO_2^--N was diluted to 100 mL by adding 0.5 M Na_2SO_4 solution.

d) Standard solutions: 0, 0.2, 0.4, 0.8, 1.2, 1.4, 1.6, 1.8 and 2 mL of the prepared 1 mg L^{-1} NO_2^--N solution was diluted to 20 mL by adding 0.5 M Na_2SO_4 solution respectively. And then 0, 0.02, 0.04, 0.06, 0.08, 0.1, 0.12, 0.14, 0.16, 0.18 and 2.0 mg L^{-1} standard solutions were obtained.

The experiments of NO_2^- determination followed the below procedure: 0.2 mL color reagent was added into 10 mL of the standard solutions stepwisely. After placing the mixed solution in a dark environment for 20 min, the UV-vis measurements (the maximum λ= 540 nm) were conducted. The concentration of the synthesized in the electrolyte was also detected by the same methods. Here 0.1 mL of electrolyte was collected from the cathode cell and diluted to 10 mL to reach the detection range. The ultraviolet absorption spectra (**Figure 2.12 a**) and the absorbance-concentration curve was calibrated using a series of standard solutions (**Figure 2.12 b**).

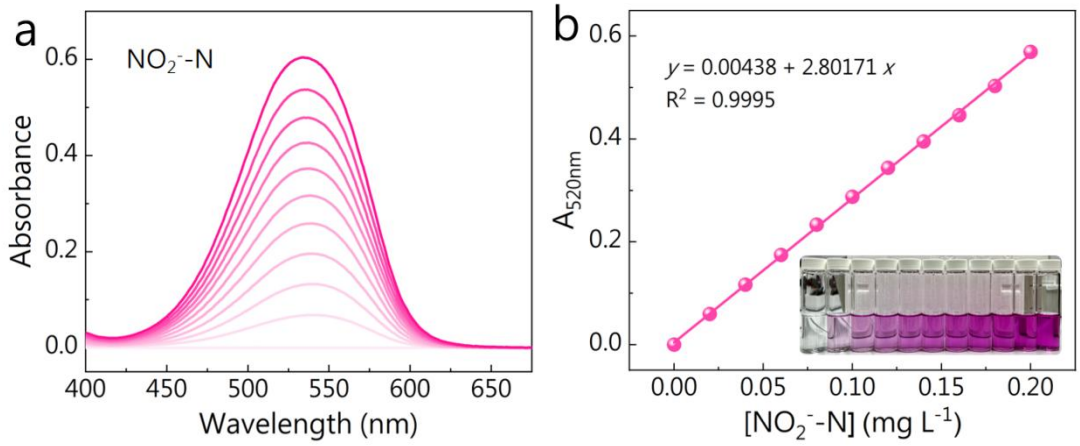


Figure 2.12 *The ultraviolet absorption spectra (a) and the absorbance-concentration calibration curve (b) of NO_2^--N. The maximum absorbance intensity (y) was measured at 540 nm and varied linearly with the NO_2^--N (x) in the linear form of y = 0.00438 + 2.80171 x, R^2=0.9996).*

2.5.3 Determination of NH_4^+-N

The NH_4^+-N concentration was determined by the Nessler's reagent as the color reagent. The reagents were prepared by the following procedure:

In the first step, two reagents were prepared: the reagent (A) - 500 g L^{-1} potassium sodium tartrate solution, and the reagent (B) - Nessler's regent.

The standard NH_4^+-N solution was prepared to calibrate NH_4^+ concentration and absorbance curves by the following procedures:

a) 1000 mg L^{-1} NH_4^+-N of 0.5 M Na_2SO_4 solution: 0.3821 g NH_4Cl was first dried in the glass dryer for 2 h, and then dissolved to 100 ml 0.5 M Na_2SO_4.

b) 100 mg L^{-1} NH_4^+-N in 0.5 M Na_2SO_4 solution: 10 mL of the prepared 100 mg L^{-1} NH_4^+-N was diluted to 100 mL by adding 0.5 M Na_2SO_4 solution.

c) 1 mg L^{-1} NH_4^+-N in 0.5 M Na_2SO_4 solution: 1 mL of the prepared 100 mg L^{-1} NH_4^+-N was diluted to 100 mL by adding 0.5 M Na_2SO_4 solution.

d) Standard solutions: 0, 2, 4, 6, 8 and 10 mL of the prepared 1 mg L^{-1} Na_2SO_4 solution were diluted to 10 mL by adding 0.5 M Na_2SO_4 solution respectively. And then 0, 0.2, 0.4, 0.6, 0.8 and 1.0 mg L^{-1} NH_4^+-N standard solutions were obtained.

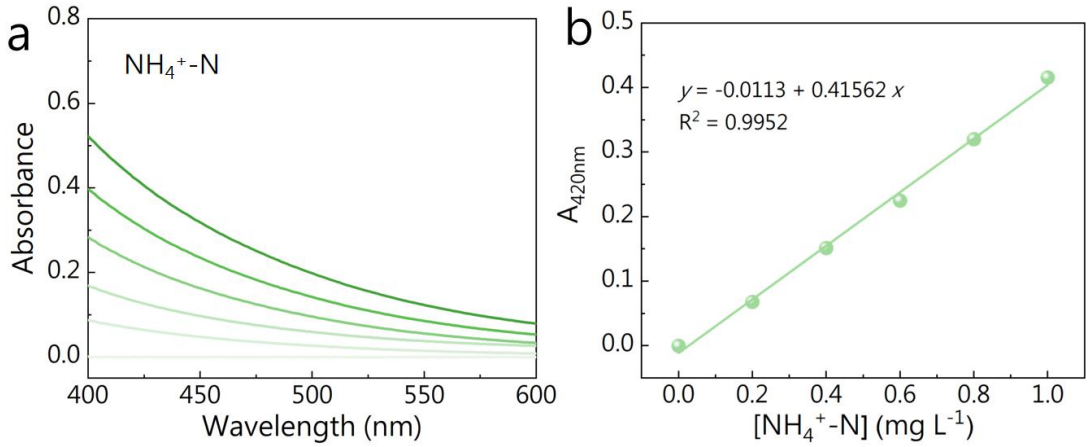


Figure 2.13 *Calibration curve of NH_4^+-N concentration and the maximum absorbance. The maximum absorbance intensity was measured at 420 nm, and the fitting curve shows good linear relation between the maximum absorbance intensity (y) and the NH_4^+ concentration (x) following the linear equation of y = 0.41562x - 0.0113 (R^2=0.9952).*

The experiments of NH_4^+ determination followed the below procedures: 0.2 mL reagent (A) and 0.2 mL reagent (B) were added into 10 mL of the standard solutions

consequently. After placing the mixed solution in a dark environment for 20 min, UV-vis measurements were conducted at 420 nm. The concentration of NH_4^+-N in the electrolyte was also detected by the same method. In more detail, 0.25 mL of electrolyte was collected from the cathode cell and diluted to 10 mL to reach the detection range. The ultraviolet absorption spectra (**Figure 2.13 a**) and the absorbance-concentration curve **(Figure 2.13 b**) was calibrated using a series of standard solutions.

2.6 Computer simulations

Computer simulations were based on Density Functional Theory (DFT) calculations, which were used to investigate the geometry, electronic properties, and interactions of the studied materials. By constructing appropriate models as well as performing geometry optimization and electronic structure calculations, the properties of diamond-metal and diamond-metal carbide interfaces were analyzed. Additionally, DFT simulations were conducted to reveal the catalytic properties of Cu_2O and Cu toward the NO_3RR.

2.6.1 Models construction for BNDD/Si, BNDD/TiN, and BNDD/TaC

The DFT calculations, including the calculations of geometry relaxation and electronic structures were conducted on the Vienna ab initio Simulation Package (VASP) with the exchange-correlation functions of Perdew-Burke-Ernzerhof (PBE) and generalized-gradient approximation (GGA). The plane-wave kinetic-energy cutoff was set at 450 eV effect. For all models, six layers of diamond (111) were combined with several layers of metal and metal carbide. A vacuum layer of 10 Å was adopted to avoid the interactions at the interface. The established size of the cell surface region was about 5 Å by 5 Å, reflecting the properties of a certain microscopic region of the periodic electrode structure. For geometry optimization, the Brillouin zone was settled with 3×3×1 *k* points. For electronic structure 9×9×1 *k* points were employed for

optimal results. Geometry optimization was employed for all systems until the residual forces were converged to 0.01 eV $Å^{-1}$ and the energy criterion was to 10^{-6} eV (**Figure 2.14**).

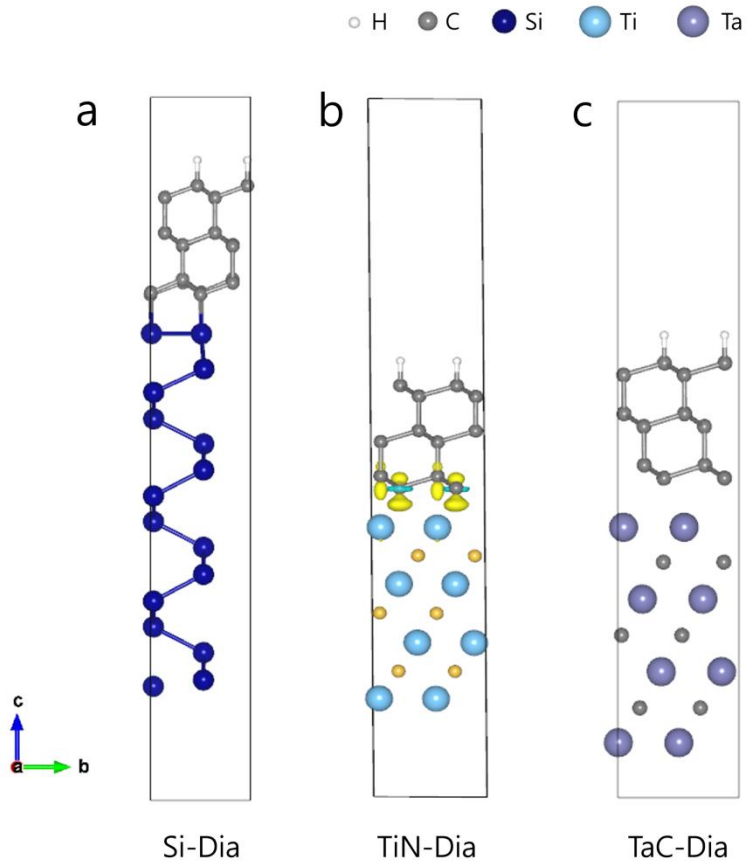


Figure 2.14 *The constructed models of (a) BNDD/Si, (b) BNDD/TiN, and (c) BNDD/TaC.*

2.6.2 Models construction for Cu and Cu_2O

The DFT calculations were employed with the plane-wave code implemented in the Vienna Ab Initio Simulation Package (VASP). The electron exchange and correlation were described with the generalized gradient approximation as parameterized by Perdew, Burke, and Ernzerhof (GGA-PBE). The interaction between ions and electrons was modelled by the projector augmented wave method (PAW). For all calculations, the kinetic cut-off energy was set to 400 eV. The self-consistent field (SCF) tolerance was limited to 1×10^{-6} eV and 0.03 eV $Å^{-1}$.

According to the TEM and XRD results, the (100) crystal facet of Cu_2O and (111) crystal facet of Cu were chosen. A vacuum region of 20 Å was set along the *z* direction to avoid the interaction between slabs (**Figure 2.15**). The *k*-point mesh was defined as 3× 3 × 1 for the structural relaxation and 9 × 9 × 1 for electronic structure calculations.

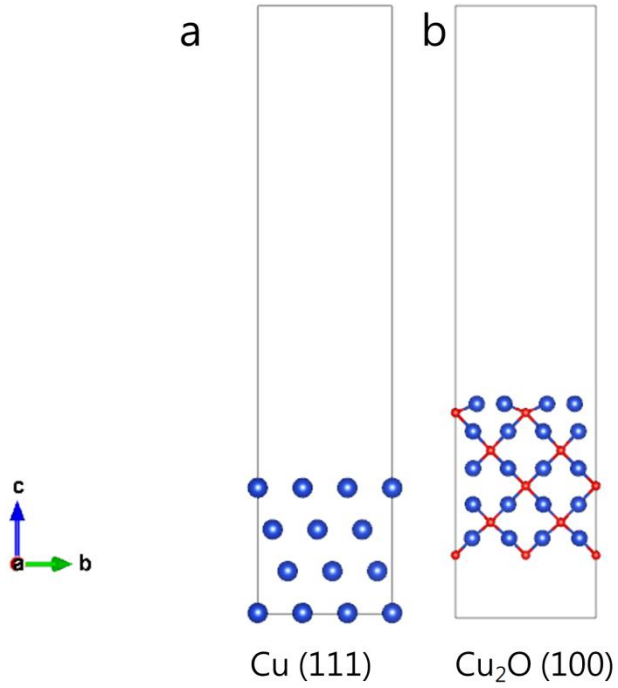


Figure 2.15 *The constructed models of (a) Cu (111) (b) Cu_2O (100).*

Chapter 3. BNDD/Metal/Si films for supercapacitors

Doped diamond, a well-known electrode candidate in the field of electrochemistry,[10] has been widely employed as an electrode to construct agrochemical sensors,[11,12] supercapacitors,[13,14] and for electromagnetically corrosion,[15] electrolysis (e.g., oxygen reduction reaction (ORR)),[16] and other electrochemical applications. This is due to the unique properties of doped diamond electrodes, such as low background currents in both aqueous and non-aqueous solutions, wide potential windows in different media, and long-term durability in harsh environments and under extreme conditions.[17] It is important to point out that these unique features strongly depend on the amount of sp^3-carbon and carbon impurities, surface terminations, and defects in diamond layers.[6-9] For example, a *p*-type boron-doped diamond (BDD) exhibits a metal-like conductivity once the boron doping level is above 10^{20} cm^{-3}. A *n*-type nitrogen-doped diamond (NDD) has a wider potential window in comparison to a BDD electrode.[6] Regarding the effect of dopants on these unique features, the electrochemistry of bi-element incorporated diamond films has been boosted, investigated and discussed very recently.[21,23-26]

Compared to single-doped diamond, co-doped diamond with an optimal B/N ratio enables more precise regulation of its electronic structure, significantly accelerating electron transfer rates and enhancing its activity in various electrochemical and catalytic reactions. In the B-N co-doping system, boron (B) acts as an acceptor dopant, providing holes, while nitrogen (N) serves as a donor dopant, supplying electrons. Their synergistic interaction optimizes the Fermi level position and modulates the density of states (DOS), thereby improving the material ' s conductivity and charge transfer kinetics.[27-29] This electronic structure optimization not only enhances the efficiency of BNDD in electrochemical energy storage and conversion but also significantly improves its selectivity and stability in catalytic reactions. For instance, BNDD films with a well-controlled B/N ratio have been

widely utilized in supercapacitor assemblies, offering excellent charge storage capabilities. Additionally, BNDD exhibits high catalytic activity in CO_2 reduction reactions (CO_2RR), where fine-tuning the B/N ratio can further optimize reaction selectivity and product distribution.[24] The BNDD films with adjustable nitrogen and boron dopant ratios exhibit similar performance toward the ORR as a commercial Pt/C catalyst, including high current densities for the ORR and its long-term durability during the ORR.[21] Beyond these applications, BNDD also demonstrates immense potential in fuel cells, water treatment, and other electrocatalytic fields, making it a promising material for next-generation energy and environmental technologies.

On the other hand, a mechanical robust substrate is frequently required to achieve high electrochemical performance of doped diamond electrodes, especially to have flexible diamond electrodes. However, diamond films are usually grown on silicon,[85,86] which is fragile and has poor mechanical properties.[87] To overcome the drawbacks of silicon, other substrates (e.g., metal, carbon fibers, carbon nanotubes) were used for the growth of doped diamond films.[88-90] In this way, as-grown diamond films are expected to possess low contact resistivities (using ohmic/nonrectifying contacts), good adhesion, high thermal stability, high corrosion resistances. Taking titanium as a promising substrate an example, a BDD electrode grown with Ti as the substrate has a maximum capacitance of 53.3 $mF \cdot cm^{-2}$ and a minimum charge transfer resistance (R_{ct}) of 4.8 Ω. Under the certain conditions, electrical conductivity and mechanical flexibility of as-grown diamond films have been further improved.[91,92] Recent reports have shown that metals like Ta, Nb or semi-metallic materials (e.g., Ge), exhibit better electrochemical performance than a Ti substrate.[86,93,94] It is thus of significance to employ them as a substrate to grow doped diamond films. Surprisingly, neither the growth of diamond films on these interlayers nor the electrochemistry of such diamond electrodes has been investigated thoroughly, probably due to the fact that diamond films peel off from these metal interlayers

easily.[95]

In this thesis, CVD growth of B,N-co-doped diamond on Ti and Ti/Ta interlayers that were sputtered on Si substrates has been tested. The characterizations of these as-grown diamond films with scanning electron microscope (SEM), Raman spectroscopy, secondary ion mass spectrometry (SIMS), X-ray photoelectron spectroscopy (XPS), electron energy loss spectroscopy (EELS) were conducted, confirming the presence of C,O-doped TiN and TaC within the interlayer. The electrochemical properties of these diamond films were systematically evaluated in both $[Fe(CN)_6]^{3-/4-}$ or $[Ru(NH_3)_6]^{3+/2+}$ redox systems, including their potential difference of oxidation and reduction peaks, electrochemical effective active areas, double layer capacitances (C_{dl}), potentials towards oxygen evolution reaction (OER) and hydrogen evolution reaction (HER). To explain these electrochemical results, density functional theory (DFT) calculations were done to determine the density of states at different interlayers between Si and diamond. To further explore electrochemical properties of these diamond films, diamond supercapacitors have been fabricated.

3.1 Characterization for BNDD/Metal/Si films

The SEM images of the BNDD/Si (**Figure. 3.1 a**), BNDD/Ti/Si (**Figure. 3.1 b**), and BNDD/Ta/Ti/Si (**Figure. 3.1 c**) were recorded. These films exhibit the typical morphology of polycrystalline diamond films. The surface crystal grains are clear and dense. Their grain sizes were calculated from the statistical results of grain size distribution. Specifically, for the BNDD/Si, BNDD/Ti/Si, and BNDD/Ta/Ti/Si, the respective sizes are 173 nm (**Figure 3.1 d**), 162 nm (**Figure 3.1 e**), and 144 nm (**Figure 3.1 f**). Consequently, it can be inferred that the different interlayers may affect the morphologies of the particle sizes of the BNDD films.

The scanning transmission electron microscope-electron energy loss spectroscopy (STEM-EELS) elemental mapping of C, Si, and Ti together with the

simultaneously acquired high angle annular dark field (HAADF) images of the BNDD/Si (**Figure 3.2 a)**, BNDD/Ti/Si (**Figure 3.5 b)**, and BNDD/Ta/Ti/Si (**Figure 3.2 c)** were also recorded, where different interlayers were clearly shown. The diamond layer has a thickness of about 180 nm, while the Ti and Ta sputter layers are about 30 nm and 27 nm in their thickness, respectively.

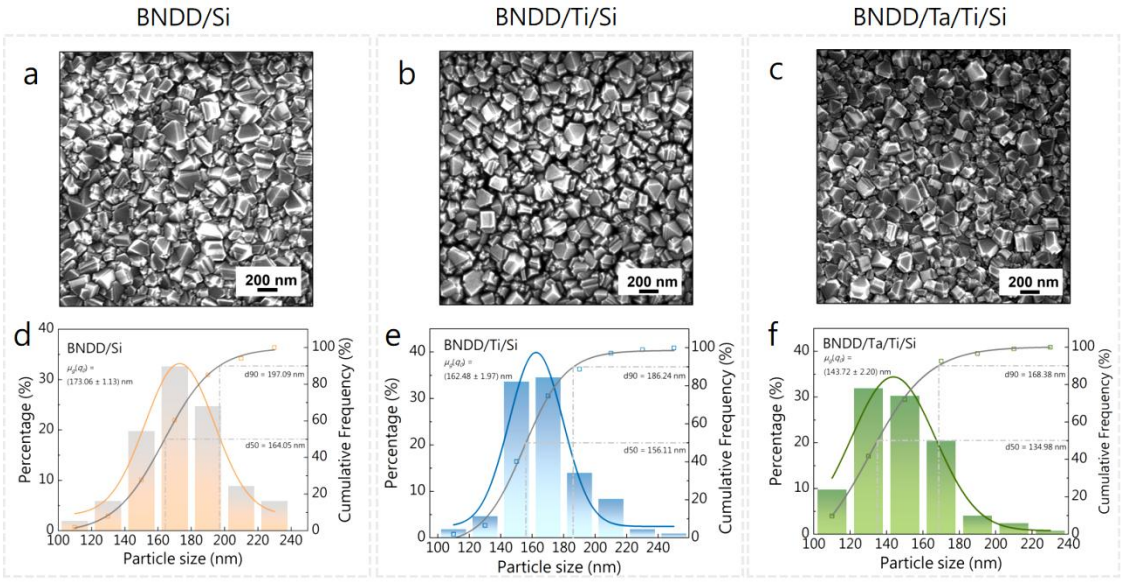


Figure 3.1 *SEM images (a, b, c), grain size statistics (d, e, f) of the BNDD/Si, BNDD/Ti/Si, and BNDD/Ta/Ti/Si, respectively.*

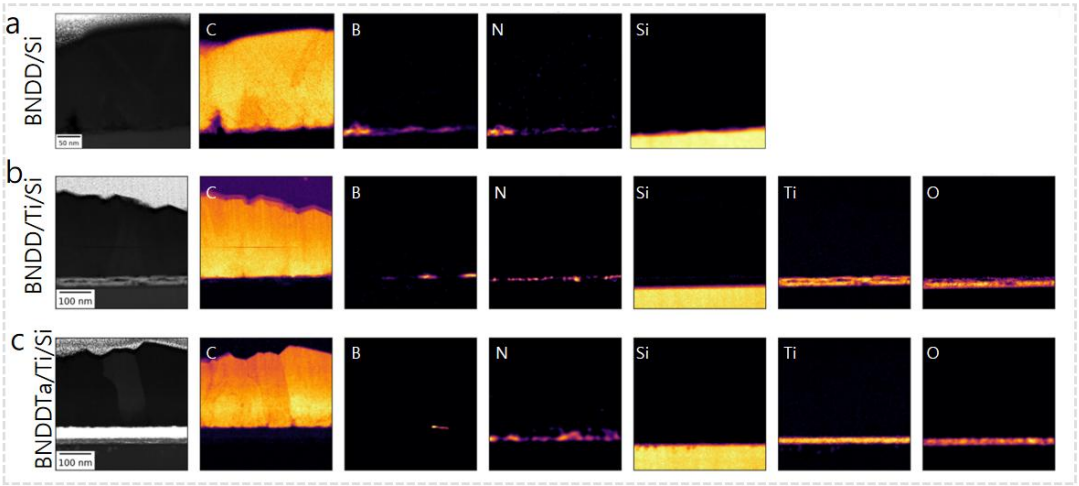


Figure 3.2 *Side view and STEM-EELS elemental mapping of the BNDD/Si (a), BNDD/Ti/Si (b), and BNDD/Ta/Ti/Si (c), respectively.*

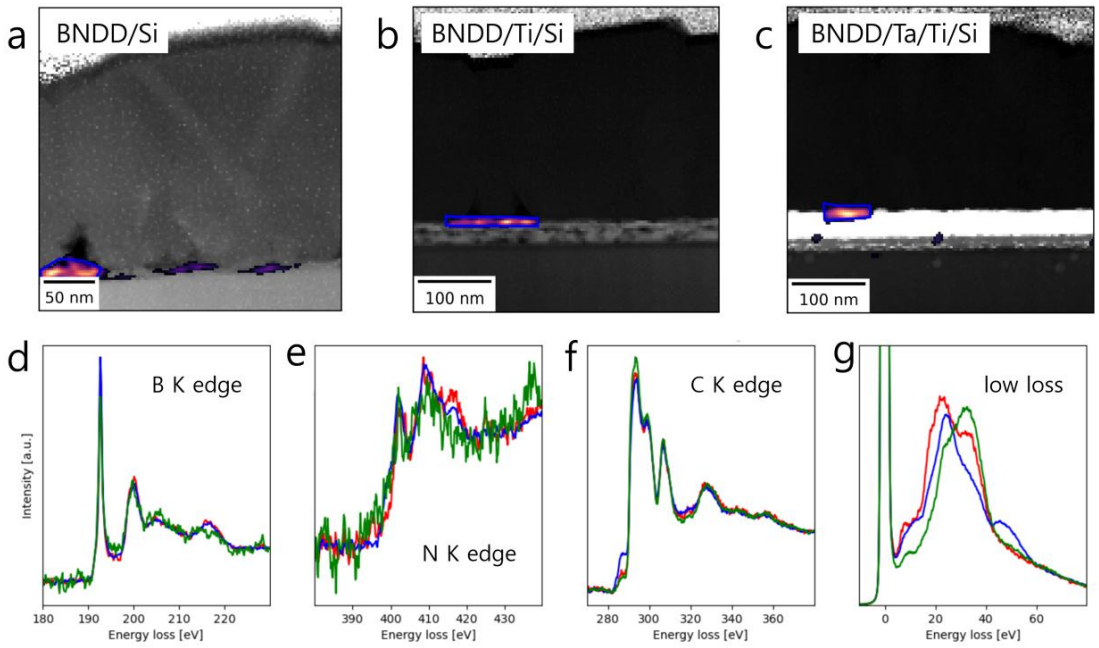


Figure 3.3 *Analysis of the BN regions present at the interface between the BNDD and the coated/uncoated Si substrate. Overlay of the B-elemental map with the HAADF image for BNDD/Si (a), BNDD/Ti/Si (b), and BNDD/Ta/Ti/Si (c) the respective spectra of the B K edge (d), N K edge (e), C K edge (f) and the plasmon region (g) are reported for BNDD/Si (red), BNDD/Ti/Si (blue), and BNDD/Ta/Ti/Si (green).*

At the interface of the Si substrate and nanodiamond crystals, as well as within defect regions at grain boundaries, the co-presence of B and N dopants as BN was identified based on the strong π * peak of hexagonal boron nitride[96] or graphitic BC_2N[97] with EELS fine structure exhibiting nearly indistinguishable characteristics[98] (**Figure 3.3 a, d, e**). When a Ti buffer layer is sputtered on the Si substrate, the presence of a similar BN layer at the interface between Ti and BNDD is also present. A separation within the Ti layer between a bottom O-rich layer close to the Si-substrate is probably related to the presence of a SiO_x oxidized layer on the substrate surface and an N-rich layer above (**Figure 3.3 b**). Finally, for the bottom panels of the BNDD/Ta/Ti/Si, the BN layer is only present in asperities of the growing film and the N seems to be segregating at the interface between Ta and Ti layers (**Figure 3.3 c**). Consequently, an almost continuous BN layer present is clearly

identified at the interface between the BNDD and the Si substrate, as well as between the BNDD and Ti layer, but it is nearly absent for the TaC layer (**Figure 3.3**).

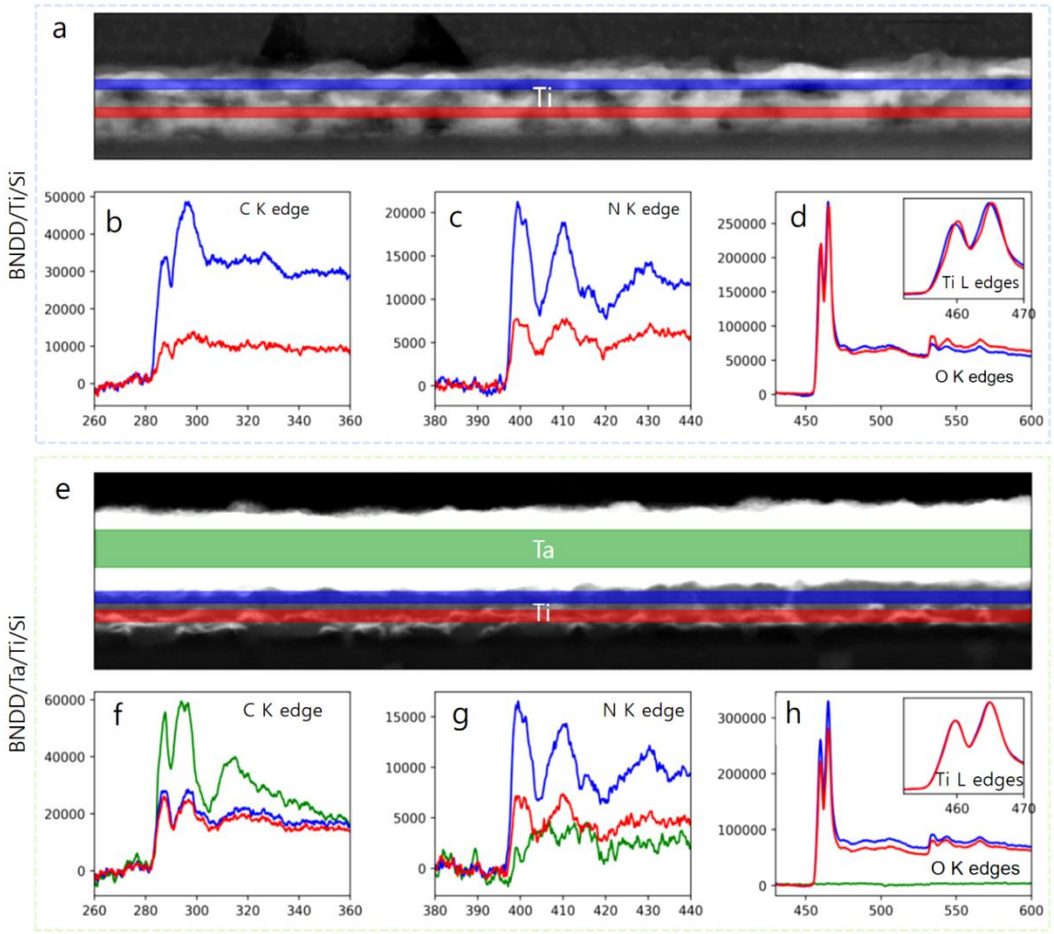


Figure 3.4 *ELNES analysis of the BNDD/Ti/Si and BNDD/Ta/Ti/Si interfaces. (a) HAADF image of the interface of the BNND/Ti/Si together with the C K edge (b), N K edge (c) and Ti L and O K edges (d) for two distinct regions close to the Si-substrate in red and close the BNDD in blue. (e) HAADF image of the interfacial region of the BNDD/Ta/Ti/Si with the fine structures of the C K edge (f), N K edge (g) and Ti L and O K edges (h) extracted the Ta layer in green, and the same two blue and red regions.*

Energy-loss near edge structure (ELNES) analysis was further performed to provide a clearer illustration of the elemental distribution in these diamond films at the interfaces of BNDD/Ti/Si and BNDD/Ta/Ti/Si. The region of the interface between the BNND/Ti/Si is represented in **Figure 3.4 (a)**, along with the C *K* edge

(**Figure 3.4 b**), N *K* edge (**Figure 3.4 c**), Ti *L* and O *K* edges (**Figure 3.4 d**) for two distinct regions close to the Si-substrate in red and close the BNND in blue. A clear shift of the Ti L edge between the two regions as well as a higher O content of the region close to the Si substrate while the blue region is richer in C and N are noticed. The fine structure of the N *K* edge in the Ti layers is a clear indication of the presence of TiN type bonding.[99] The shift to higher energy observed when getting close to the Si substrate is correlated with the increase in oxygen content of the C,O-containing TiN layer.[100] On the other hand, for the interfaces BNDD/Ta/Ti/Si (**Figure 3.4 e**), the fine structures of the C *K* edge (**Figure 3.4 f**), N *K* edge (**Figure 3.4 g**) and Ti *L* and O K edges (**Figure 3.4 h**) are extracted for the same two blue and red regions as well as the Ta layer in green. The shift previously observed in the Ti L edge between the blue and red regions is now absent and their carbon and oxygen content became similar while the N content of the Ti layer close to the Ta layer remains very high. The carbon fine structure in the green Ta region is a clear indication of the presence of TaC, in other words the TaC layer is clearly identified in the BNDD/Ta/Ti/Si compound.[99]

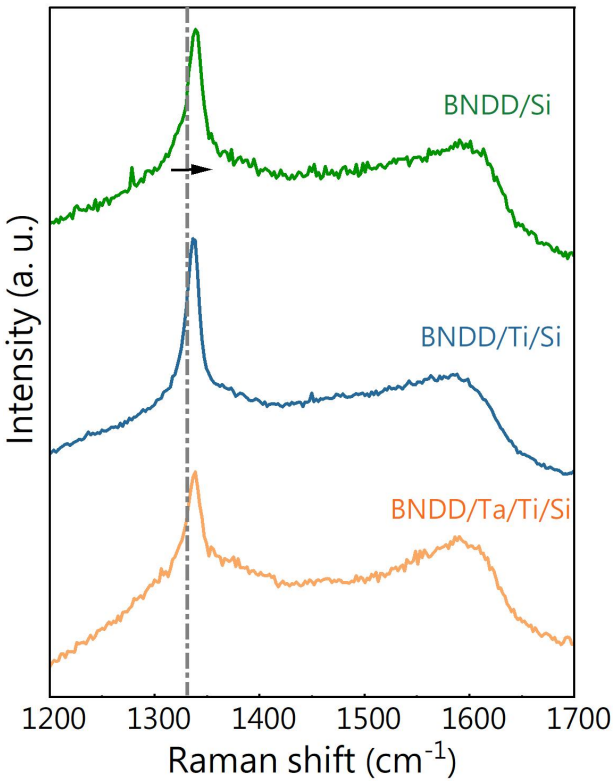


Figure 3.5 *Raman spectra of the BNDD/Si, BNDD/Ti/Si, and BNDD/Ta/Ti/Si films.*

The Raman spectra of these BNDD films were also recorded (**Figure 3.5**). The Raman peak of high-quality diamond is usually located at 1332 cm^{-1}. This characteristic peak of our BNDD films shifts to higher wavenumbers, due to nitrogen and boron doping.[101]

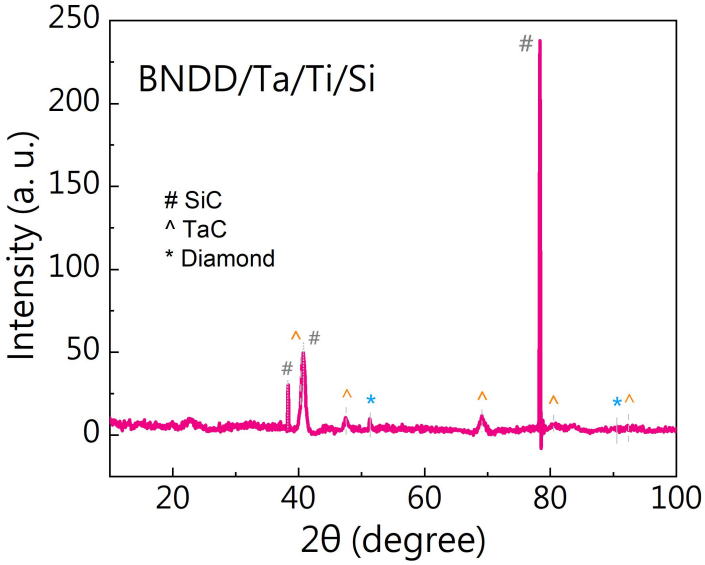


Figure 3.6 *Micro-XRD patterns of a BNDD/Ta/Ti/Si film.*

The crystal structures and phase purities of these BNDD/Ta/Ti/Si films were investigated by means of XRD (**Figure 3.6**). The comparison of diffraction peaks and relative intensities of the crystal surfaces confirms that all the films have good purity, crystallinity and similar crystal shapes. For the BNDD/Ta/Ti/Si, the diffraction peaks of (330), (212), (200) crystalline surfaces of Ta appear at the 2θ of 38.0°, 39.2°, 50.8°, respectively. Therefore, the formation of corresponding carbide layers is again confirmed during the diamond growth on Si, Ti/Si and Ta/Ti/Si substrates.

The surface analysis of these diamond films was performed using XPS, focusing on the high resolution C1s spectra (**Figure 3.7**). In these spectra, the binding energies of diamond sp^3-carbon peaks are centered at 285.2, 285.3, and 285.3 eV for BNDD/Si, BNDD/Ti/Si, and BNDD/Ta/Ti/Si, respectively. The peaks located at 283.3, 283.8, and 283.6 eV are attributed to sp^2-carbon, while those at 286.3, 286.8, and 286.3 eV

are assigned to carbon bonded to oxygen (C−O).[102,103] Note that the BNDD films with different interlayers exhibit no effect on the ratio of sp^2/sp^3 carbon (**Table 3.1**). Such a constant sp^2 content shown in XPS C1s spectra may be arisen from the in-plane stretching modes at the grain boundaries, while the dominant content in the bulk phase remains as sp^3 carbon.

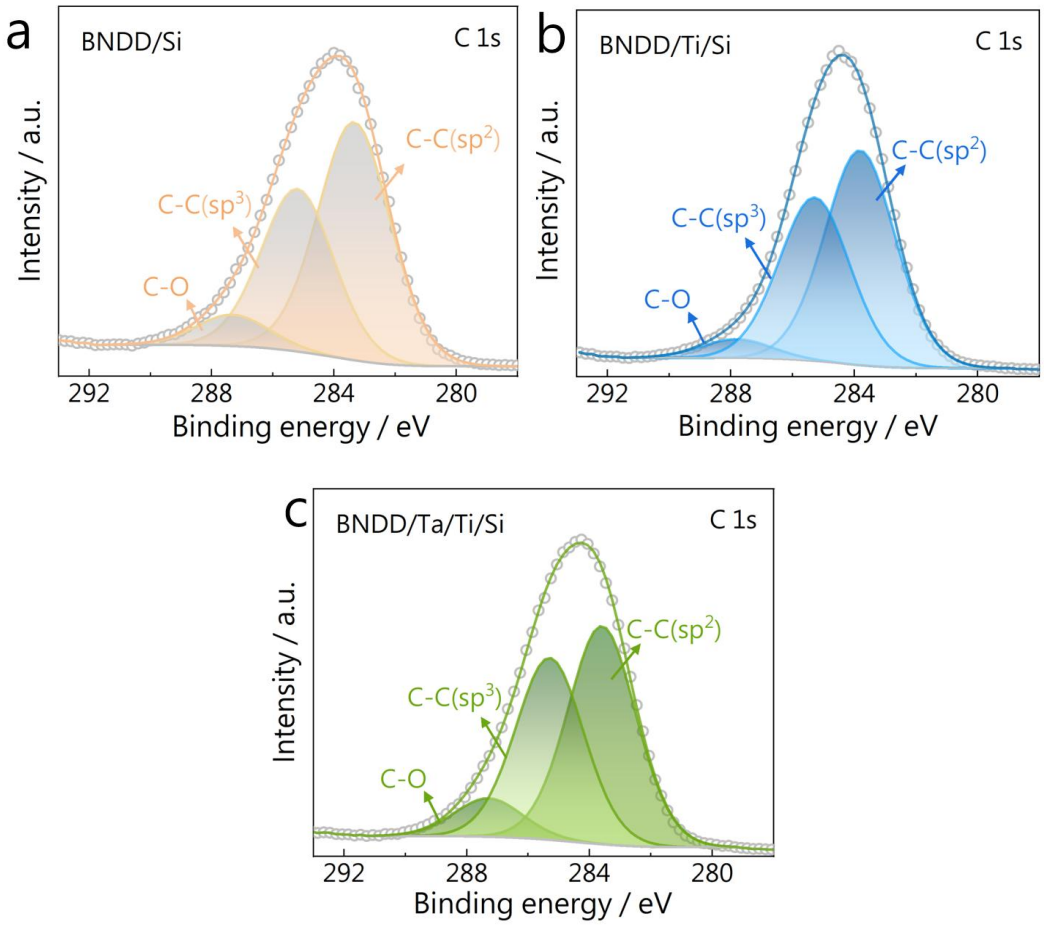


Figure 3.7 *C1s XPS spectra of the (a) BNDD/Si, (b) BNDD/Ti/Si, and (c) BNDD/Ta/Ti/Si.*

To further illustrate the carbon sp^2/sp^3 hybridization in the cross section of these films, their ELNES analysis was conducted. In **Figure 3.8**, three regions of each sample were recorded: on top (red), center (blue), and bottom (green). The center region clearly shows sp^2 and sp^3 content. Additionally, the ratio between the gray (sp^2) and yellow (sp^3) regions indicated on the spectrum was a measure of sp^2/sp^3 hybridization. Therefore, sp^2/sp^3 hybridization is minimal in the bulk material,

indicating that it consists predominantly of diamond.

Table 3.1 *Relative abundance of the carbon components in the BNDD/Si, BNDD/Ti/Si, and BNDD/Ta/Ti/Si*[*]*.*

	sp^2 C	sp^3 C	C-O	sp^2 C/sp^3 C
BNDD/Si	46.38	31.71	6.11	1.46
BNDD/Ti/Si	48.08	36.72	10.64	1.31
BNDD/Ta/Ti/Si	43.75	36.56	7.74	1.20

[*] These atomic ratios were estimated from their high resolution C1s XPS spectra.

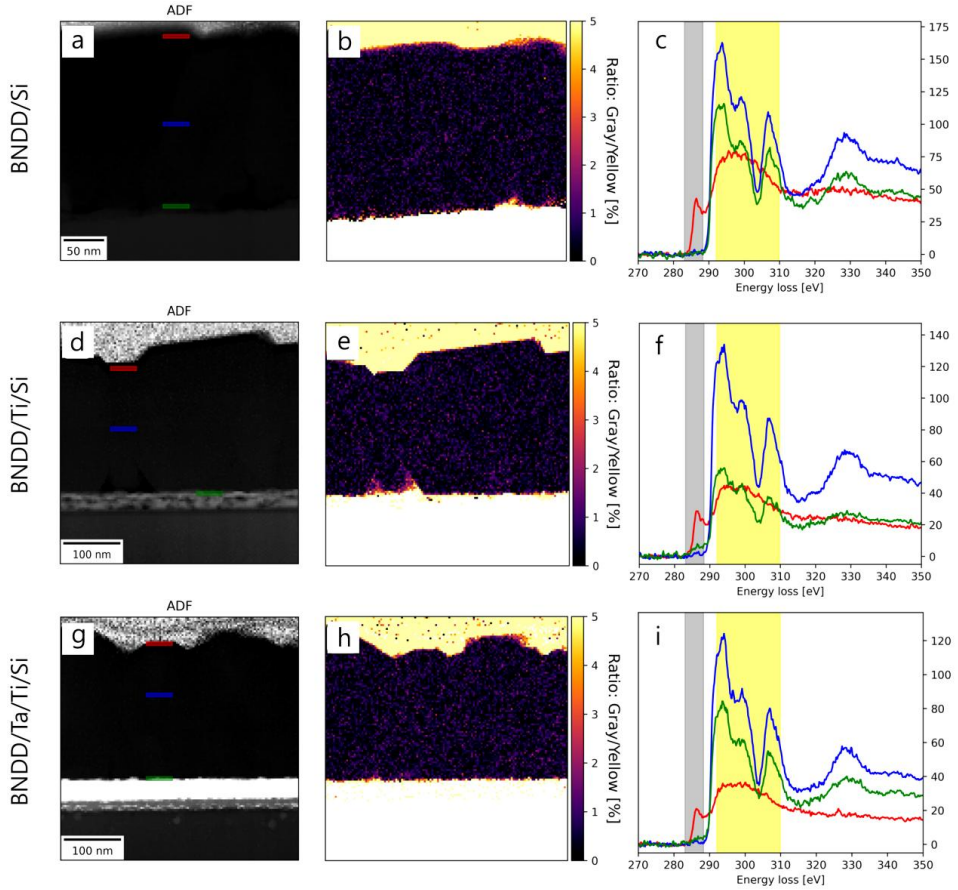


Figure 3.8 *Analysis of the sp^2/sp^3 hybridization regions by top (red), center (blue), and bottom (green) (a, d, g). The ratio between the gray (sp^2) and yellow (sp^3)(b, e, h), the respective spectra of the C K edge (c, f, i) are reported for top (red), center (blue),*

and bottom (green) for BNDD/Si, BNDD/Ti/Si, and BNDD/Ta/Ti/Si.

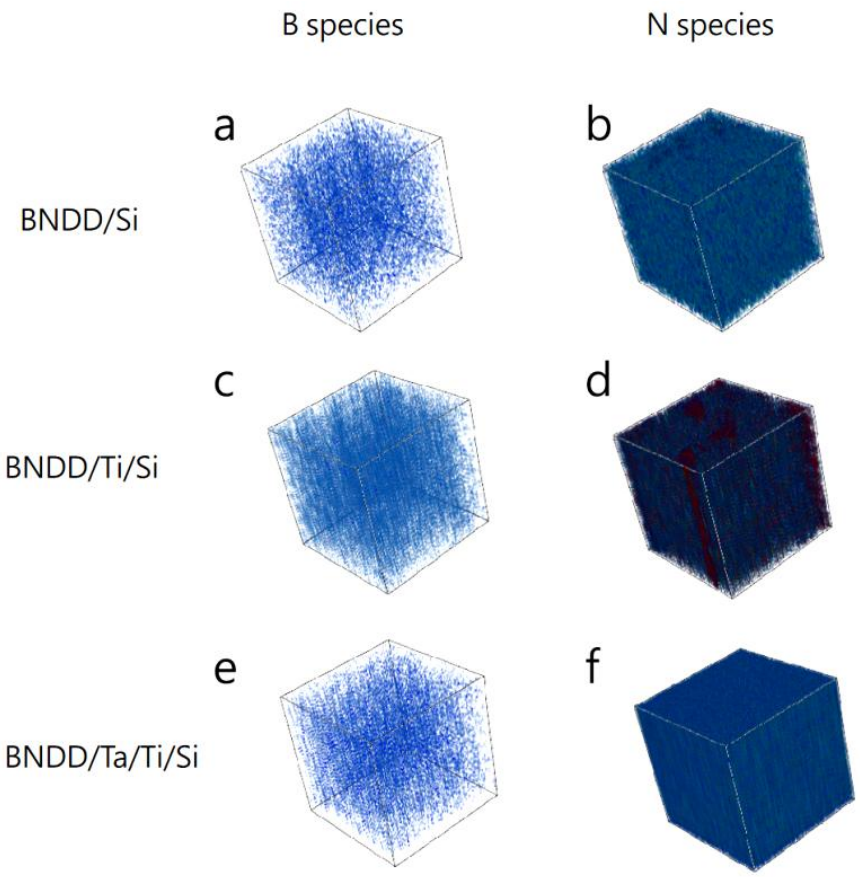


Figure 3.9 *3D render overlay SIMS of boron- and nitrogen-doped species in (a,b) BNDD/Si, (c,d) BNDD/Ti/Si, and (e,f) BNDD/Ta/Ti/Si.*

Furthermore, all of the detected boron element (re-bonding as B^+, $^{10}B^+$, CH_3NB^+, CH_3OB^+) and nitrogen element (re-bonding as re-bonding as N^+, N_2^+, $N_2H_3^+$, CH_3N^+, $C_3H_9N_2^+$, CH_3NB^+, $C_7H_{19}N_2O^+$) are found to be homogeneously and uniformly distributed throughout the diamond surface, as confirmed from SIMS with a 3D render overlay version in these three films (**Figure 3.9**). According to EELS characterization data, although BN mostly exists in the growth cracks in the form of compounds, a small amount of B and N are uniformly doped in other forms in the diamond (**Figure 3.9**), the co-doping of these small amounts of boron and nitrogen elements will introduce additional energy levels and change the electronic structure of the diamond. This may affect the electrical conductivity and electron transport

properties of diamond materials.

To check the electrochemical performance of these BNDD films grown on the different interlayers, they were investigated using both outer (**Figure 3.10 a**) and inner (**Figure 3.10 b**) redox probes. In these cyclic voltammograms, a pair of well-defined redox peaks are clearly observed. However, their peak currents and peak potentials are different on these BNDD films. In both $[Ru(NH_3)_6]Cl_3$ and $K_3[Fe(CN)_6]$ redox systems, the redox peak currents follow the order of BNDD/Si < BNDD/Ti/Si < BNDD/Ta/Ti/Si. On the BNDD/Ta/Ti/Si film, the difference in the anodic peak potential from the cathodic one is the smallest. Consequently, the BNDD/Ta/Ti/Si electrode has better electrochemical activity, toward both outer- and inner-sphere redox probes.

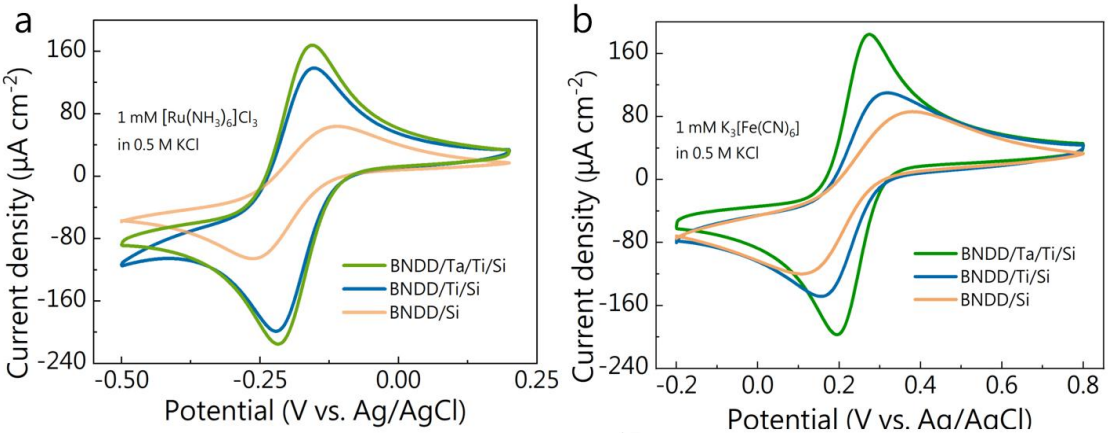


Figure 3.10 *CVs of (a) 1 mM $[Ru(NH_3)_6]Cl_3$ and (b) 1 mM $K_3[Fe(CN)_6]$ in 0.5 M KCl on three BNDD films at a scan rate of 100 mV s^{-1}.*

To further examine electrode kinetics of such redox probes on these diamond films, their CVs of $K_3Fe(CN)_6$ (**Figure 3.11 a, b, c**) were further recorded at different scan rates. The anodic peak currents are proportionally enhanced as a function of the square roots of scan rates (**Figure 3.11 d**), confirming a reversible and diffusion-controlled electrode process on all these electrodes. According to the Randles-Sevčik equation and the slopes, the electrochemically active areas of the BNDD/Si, BNDD/Ti/Si and BNDD/Ta/Ti/Si film electrodes were calculated, which

are 0.19, 0.34, and 0.85 cm^2, respectively. These film electrodes thus have different electrochemically different active areas participate in the electrochemical reaction, apparently depending on the used interlayers.

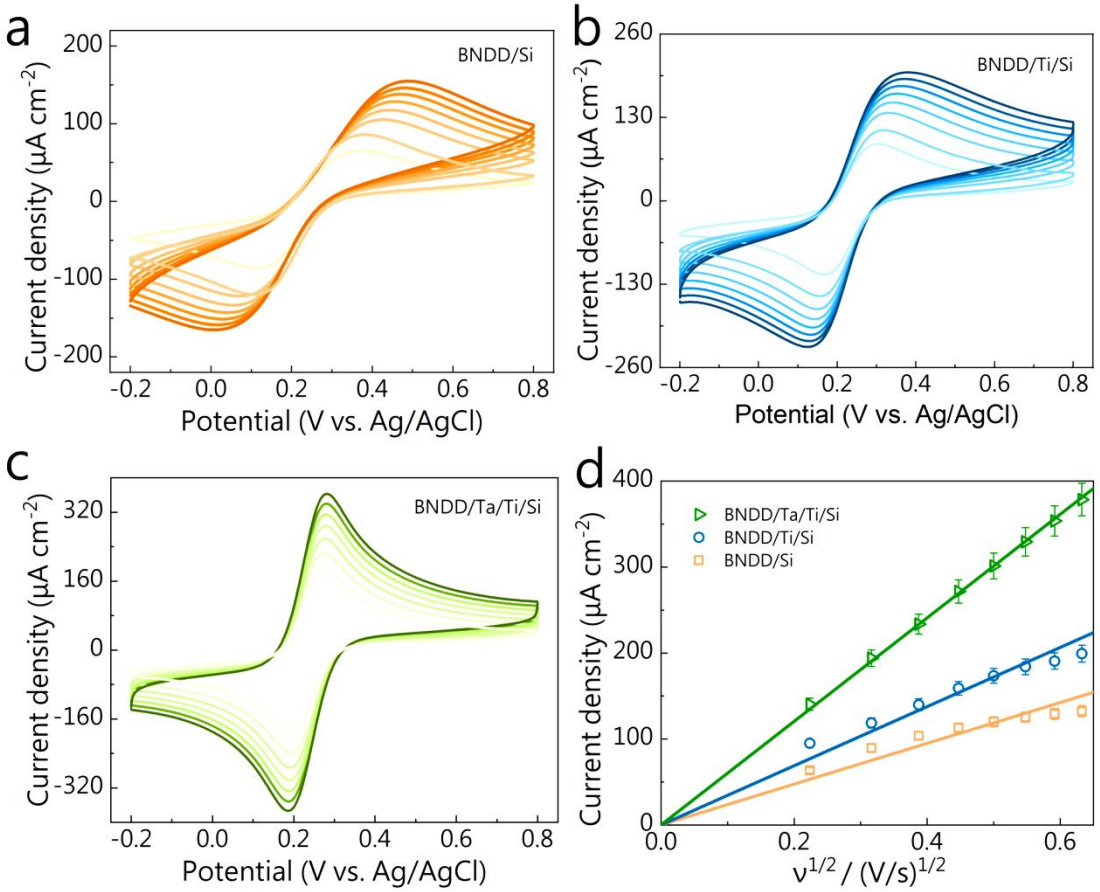


Figure 3.11 *CVs of (a) the BNDD/Si, (b) BNDD/Ti/Si and (c) BNDD/Ta/Ti/Si electrodes in 1 mM $K_3Fe(CN)_6$ and 0.1 M KCl at different scan rates. (d) The variation of anode peak currents with square roots of scan rates on these films.*

The ohmic resistances of three diamond films were estimated by use of electrochemical impedance spectroscopy (EIS). The Nyquist plots recorded in 1 mM $K_3Fe(CN)_3$ + 0.5 M KCl solution (**Figure 3.12a**) were further fitted using the Randles equivalent electric circuit (inset in **Figure 3.12a**), where C_{dl} is an electric double layer capacitance, Z_w is a mass transfer impedance and related to the diffusion rate of the redox material, and R_s is the internal resistance. The value of R_s is determined by the intrinsic resistance of the active material, the ionic resistance of the electrolyte, and

the contact resistance at the electroactive material/current collector interface. The calculated intrinsic resistance of BNDD/Si, BNDD/Ti/Si/, and BNDD/Ta/Ti/Si are 14.7, 8.4, 5.3 Ω, respectively. This indicates the intrinsic conductivities of these films are dependent on the interlayers that were applied during diamond growth. The variation tendency of such a value was further co-related with peak currents of redox probes on these films. Meanwhile, the charge transfer resistances (R_{ct}) of these electrodes were calculated. For the BNDD/Si, BNDD/Ti/Si/, and BNDD/Ta/Ti/Si, they are 212, 145, and 59 Ω, respectively. Namely, the BNDD/Ta/Ti/Si film has the highest intrinsic conductivity and the fastest electron transfer rate.[40]

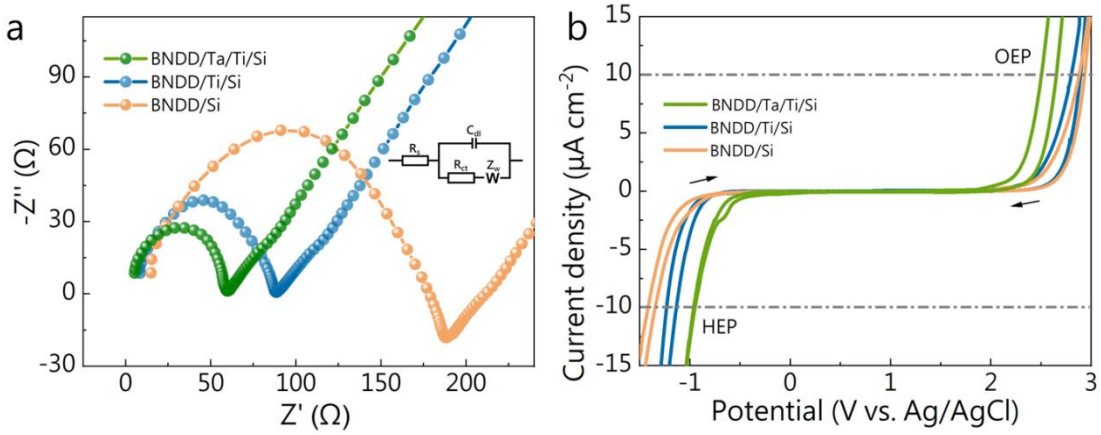


Figure 3.12 *(a) Nyquist plots of 1 mM $K_3Fe(CN)_3$ in 0.5 M KCl on the BNDD films and the fitting of the equivalent circuit (inset). (b) The OEP and HEP of the BNDD/Si, BNDD/Ti/Si, and BNDD/Ta/Ti/Si electrodes in 0.5 M H_2SO_4 solution at a scan rate of 100 mV s^{-1}.*

The electrochemical potential windows of these diamond films were evaluated. This window was defined by the potential difference in the voltammograms when the current density reached an absolution value of 10 mA cm^{-2} at a scan rate of 100 mV s^{-1}. The potential at the negative potential range was named as the hydrogen evolution potential (HEP) and at the positive potential range as the oxygen evolution potential (OEP). In 0.5 M H_2SO_4 solution (**Figure 3.12 b**), the OEPs of the BNDD/Si, BNDD/Ti/Si, and BNDD/Ta/Ti/Si electrodes are 2.88, 2.80, and 2.50 V (*vs*. Ag/AgCl), respectively. Their HEPs are −1.35, −1.14 and −0.95 V (*vs*. Ag/AgCl), respectively.

The BNDD/Ta/Ti/Si electrode does have lower potentials toward both hydrogen evolution and oxygen evolution.

The electrochemical active surface area (ECSA) was then proceeded based on the double-layer capacitance (C_{dl}). The CVs of these three electrodes were further recorded within a non-Faraday domain, namely from −0.1 to +0.1 V (**Figure 3.13a**). From these CVs recorded different scan rates in 1 M Na_2SO_4 solution (**Figure 3.14**), the electric double layer capacitances of these electrodes were estimated by plotting out the variation of the current densities as a function of scan rates (**Figure 3.13b**). The calculated C_{dl} of the BNDD/Si, BNDD/Ti/Si and BNDD/Ta/Ti/Si electrodes are 1.87, 5.70 and 8.94 μF cm^{-2}, respectively.

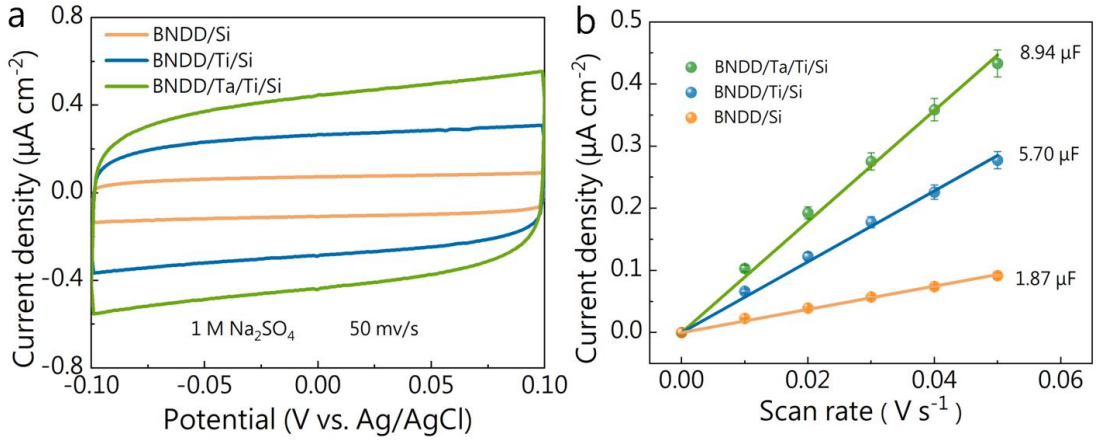


Figure 3.13 *(a) CVs of three electrodes at a scan rate of 50 mV s^{-1} in 1 M Na_2SO_4, (b) The variation of the current densities at 0.00 V with the applied scan rates.*

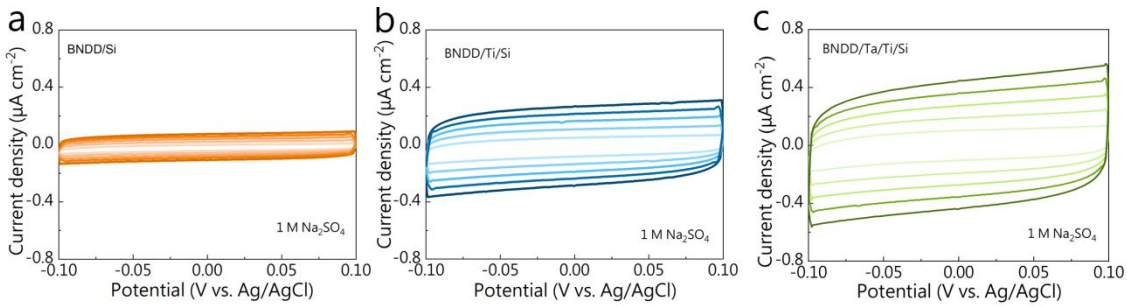


Figure 3.14 *CVs of the (a) BNDD/Si, (b) BNDD/Ti/Si and (c) BNDD/Ta/Ti/Si electrodes in 1 M Na_2SO_4 at different scan rates.*

3.2 Theoretical simulation of the BNDD films

It has been proved in previous session that the BNDD/Ta/Ti/Si electrode exhibits faster electron transfer processes, smaller electron transfer resistances of redox probes for both $[Fe(CN)_6]^{3-/4-}$ and $[Ru(NH_3)_6]^{3+/2+}$, a larger electrochemically effective active area, and more potential electrocatalytic activity than the other two diamond electrodes. The interlayer determines the intrinsic activity and reaction kinetics of diamond films (namely BNDD/Si and BNDD/Ti/Si electrodes), thus enhancing the electrochemical performance of these electrodes. Such enhanced electrochemical performance of the electrodes was further studied using theoretical simulation of its interface band structure with aid of DFT calculations.

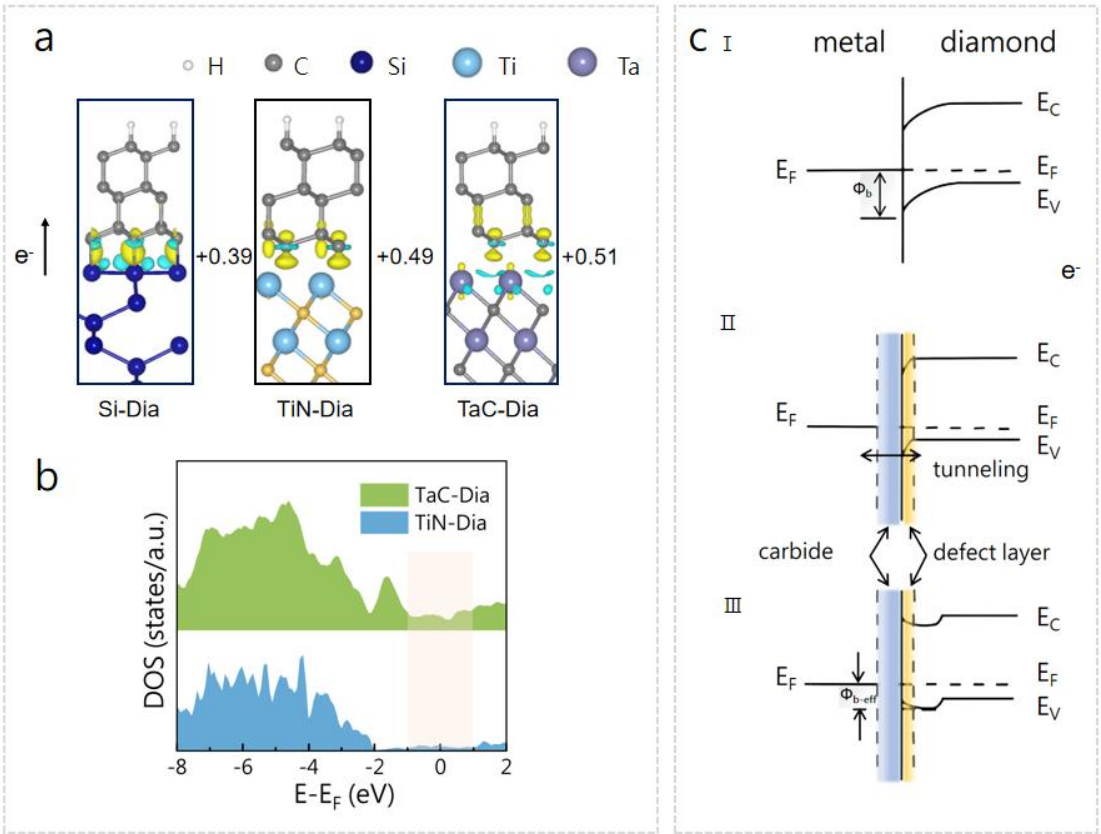


Figure 3.15 *(a) Charge density differences of BNDD/Si, BNDD/TiN, and BNDD/TaC interface. (b) Comparison of the DOS for BNDD/TiN and BNDD/TaC interface. (c) Interface band diagrams of metal layer on diamond.*

It is known that a C,O-doped TiN is present as an interlayer for BNDD/Ti/Si,

while the presence of a TaC interlayer for BNDD/Ta/Ti/Si is confirmed. The DFT calculations were thus conducted to investigate the influence of different interlayers on the interface band structures of three diamond films. For these simulations, six-layers of diamond slabs with ideal (111) surfaces were extracted from the bulk diamond structure. The number of layers applied was found to be large enough to capture the change in the electronic structure from the surface to its bulk.[104] For BNDD/Si, BNDD/TiN, and BNDD/TaC electrodes, several models of monolayers were constructed, the difference of the Bader charges and charge densities on the interfaces were then calculated (**Figure 3.15a**).

From the calculated electron density of state (DOS), one can see that the charge transfer is induced from the metal atoms to the BNDD. The charge densities at the BNDD/TaC interface are stronger than those at both BNDD/TiN and BNDD/Si interfaces, namely with a value shift from +0.39 to +0.51 eV^{-1}. To further investigate the influence of metal nitride/carbides, the DOS of the BNDD/TiN and BNDD/TaC interfaces were calculated and compared (**Figure 3.15b**). The DOS near the Fermi level appears to exhibit an increase between TaC and the diamond layer, where a more pronounced effect is observed when TaC is present. This enhanced charge transfer significantly impacts the electronic structures of bonding atoms. An increase in the density of states means more charge transfer at the interface, indicating better electrical contact. Furthermore, the metal carbides from tantalum have been utilized to achieve an ohmic contact on the diamond surface.[105]

The formation of such an ohmic contact was speculated by the defect generation at and near the diamond surface *via* the carbide-forming reaction. The presence of such defects either narrows the depletion width, thereby increasing the probability of tunneling, or reducing the effective barrier height (**Figure 3.15c**).[98] In other words, the presence of metal carbides is mainly responsible for the difference in the electrochemical properties of as-grown diamond films.

3.3 BNDD/Metal/Si films for supercapacitor fabrication

It is known that compared to electrical-double-layer capacitors (EDLCs), pseudocapacitors (PCs) rely on surface-controlled faradaic reactions of redox-active materials at the electrode/electrolyte interface. The additional charge transfer resulting from these redox reactions leads to higher capacitances in pseudocapacitors. Taking the capacitance of a pseudocapacitor using $Fe(CN)_6^{3-/4-}$ redox couples as an example, it is about four order higher than that of a diamond EDLC.[9,14]

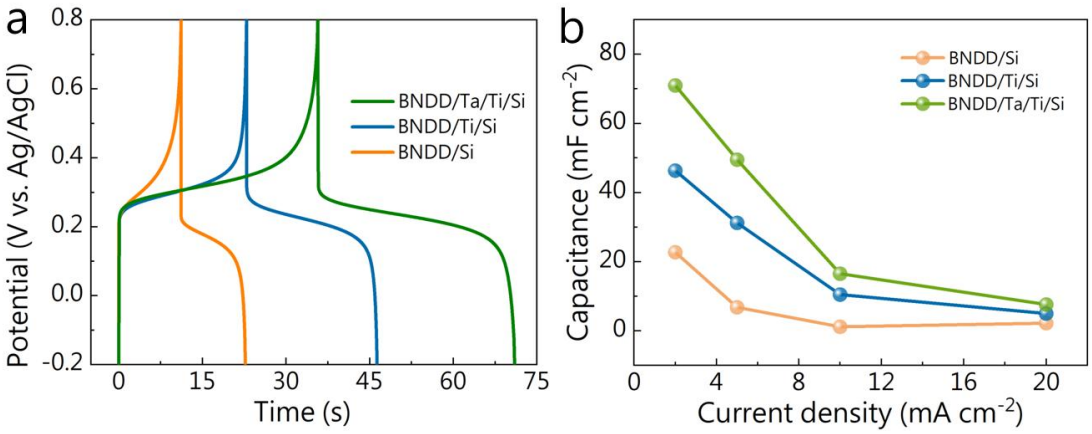


Figure 3.16 *Capacitive performance of the BNDD electrodes in 0.05 M* $Fe(CN)_6^{3-/4-}$ *+ 1.0 M* Na_2SO_4*: (a) Charge/discharge curves of the BNDD/Si, BNDD/Ti/Si, and BNDD/Ta/Ti/Si electrodes at a current density of 2 mA* cm^{-2}*. (b) The variation of the specific capacitances with current densities.*

As a case study, the potential of the BNDD films grown on different metal interlayers as a capacitor electrode, namely BNDD/Si, BNDD/Ti/Si, and BNDD/Ta/Ti/Si electrodes, have been evaluated for the construction of a supercapacitor as the capacitor electrodes. In a three-electrode system, the GCD curves of these BNDD electrodes were recorded at different current densities (**Figure 3.16a**). These electrodes have good reversibility, as evidenced by the nearly equal charge and discharge times in these GCD curves. The calculated specific capacitances for the BNDD/Si, BNDD/Ti/Si, and BNDD/Ta/Ti/Si electrodes at a current density of 2 mA cm^{-2} are 22.7, 46.3 and 71.0 mF cm^{-2}, respectively. From the GCD curves of

the BNDD/Ta/Ti/Si electrodes recorded at the current densities of 2, 5, 10, 20 mA cm^{-2}, its calculated capacitances are 71.0, 49.5, 16.5 and 7.6 mF cm^{-2}, respectively (**Figure 3.16b, Figure 3.17c**). They are higher than the BNDD/Ti/Si electrode (e.g., 46.3, 31.2, 10.4 and 5.0 mF cm^{-2}, respectively) (**Figure 3.16b, Figure 3.17b**) and the BNDD/Si electrode (e.g., 22.7, 17.0, 5.8 and 2.2 mF cm^{-2}, respectively) (**Figure 3.16b, Figure 3.17a**).

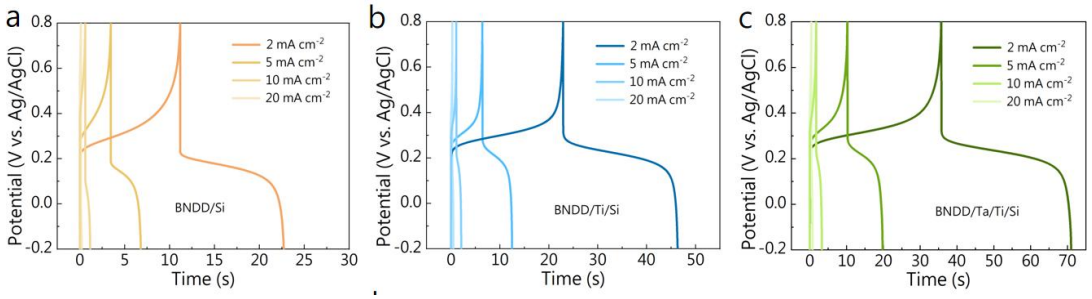


Figure 3.17 *GCD curves of the (a) BNDD/Si, (b) BNDD/Ti/Si, and (c) BNDD/Ta/Ti/Si electrodes in 0.05 M* $Fe(CN)_6^{3-/4-}$ *+ 1.0 M* Na_2SO_4 *at different current densities.*

The CVs of these diamond electrodes are compared at the same redox electrolyte at a scan rate of 10 mV s^{-1} (**Figure 3.18a**). From these CVs, the capacitances of the BNDD/Ta/Ti/Si electrode were calculated. At the scan rates of 10, 20, 50, and 100 mV s^{-1}, they are 95.3, 74.9, 46.6, and 32.2 mF cm^{-2}, respectively (**Figure 3.18b,** (**Figure 3.19a**), which are higher than those of the BNDD/Ti/Si electrode (72.1, 58.2, 35.1, and 23.9 mF cm^{-2}, respectively) (**Figure 3.19a**) and the BNDD/Si electrode (41.9, 33.2, 20.4, and 17.3 mF cm^{-2}, respectively) (**Figure 3.19b**).

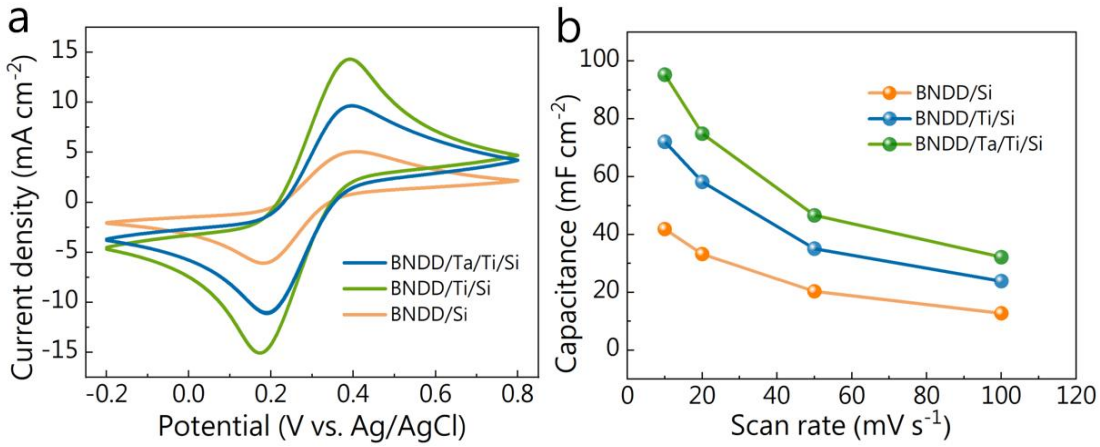


Figure 3.18 *(a) CVs recorded on the BNDD/Si, BNDD/Ti/Si, and BNDD/Ta/Ti/Si electrodes at a scan rate of 10 mV* s^{-1}*. (c) The variation of the specific capacitances with scan rates.*

As controlled experiments, the CVs of these electrodes were recorded in 1.0 M Na_2SO_4 at different scan rates. The estimated capacitances of the BNDD/Si(**Figure 3.20a**), BNDD/Ti/Si (**Figure 3.20b**), and BNDD/Ta/Ti/Si (**Figure 3.20c**) electrodes at a scan rate of 10 mV s^{-1} are only 53.1, 9.5, 7.5 μF cm^{-2}, respectively. Therefore, the addition of redox electrolytes into the solution enhances about 1000 times of the capacitances of these electrodes, as expected for such redox-electrolytes enhanced PCs.[105-107]

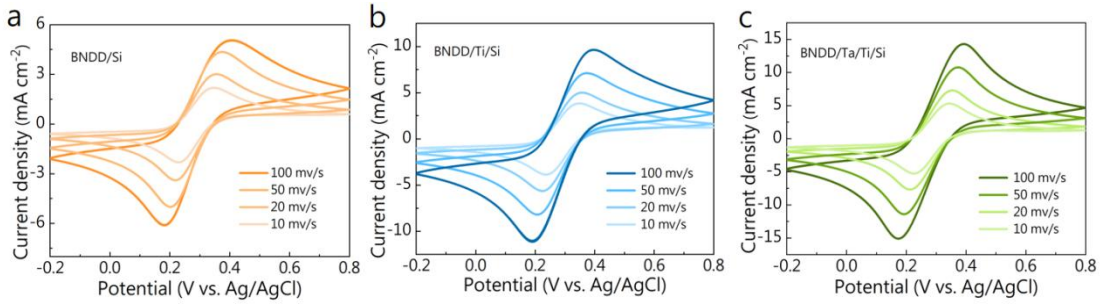


Figure 3.19 *CVs of the (a) BNDD/Si, (b) BNDD/Ti/Si, and (c) BNDD/Ta/Ti/Si electrodes in 0.05 M* $Fe(CN)_6^{3-/4-}$ *+ 1.0 M* Na_2SO_4 *at different scan rates.*

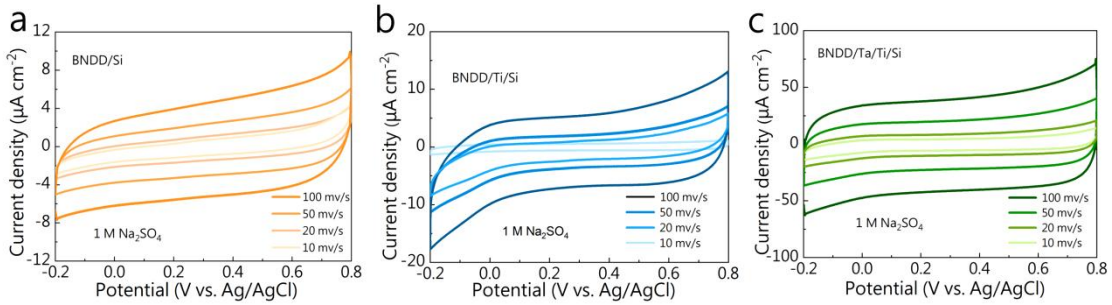


Figure 3.20 *Capacitive performance of three electrodes in 1.0 M* Na_2SO_4*: (a) CVs of the BNDD/Si, BNDD/Ti/Si, and BNDD/Ta/Ti/Si electrode at a scan rate of 100 mV* s^{-1}*; (b) the variation of the specific capacitances with scan rates; CVs of the (c) BNDD/Si, and (d) BNDD/Ti/Si and (e) BNDD/Ta/Ti/Si electrodes at different scan rates.*

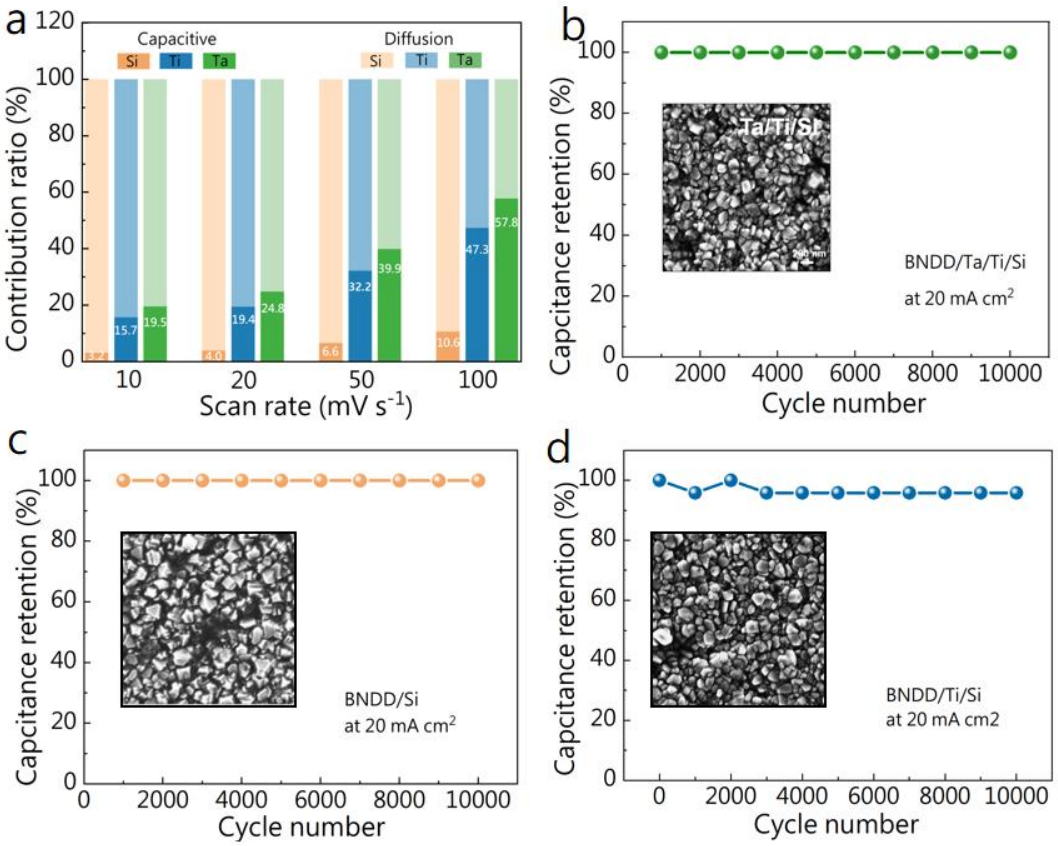


Figure 3.21 *(a) The contribution ratios of capacitive and diffusion capacities as a function of scan rates; (b-d) The capacitance retention of the BNDD/Ta/Ti/Si (b), BNDD/Si (c), BNDD/Ti/Si (d), electrode at a current density of 20 mA cm^{-2} after 10000 cycles. The inset is a SEM image of these BNDD electrodes after 10000 charge/discharge cycles at a current density of 20 mA cm^{-2}.*

For such redox-electrolytes enhanced PCs, their kinetics can be further analyzed. Namely the contributions of diffusion-bound and surface-bound species can be further quantitatively discretized using the equation of $i(v) = k_1v + k_2v^{1/2}$, where k_1v and $k_2v^{1/2}$ correspond to the capacitive effect and diffusive contribution, respectively.[108,109] The constants of k_1 and k_2 were then calculated based on the simplified equation of $i(v)/v^{1/2} = k_1v^{1/2} + k_2$ at various scan rate (v) (**Figure 3.21a**). As the scan rate increases, the capacitive contribution gradually increases. Specifically, the BNDD/Ta/Ti/Si electrode shows a higher capacitive contribution than the BNDD/Si and BNDD/Ti/Si electrodes. This reveals the better potential of the BNDD/Ta/Ti/Si electrode for electrochemical

energy storage applications. The long-term cycling stability of the BNDD/Si (**Figure 3.21b**), BNDD/Ti/Si (**Figure 3.21c**), and BNDD/Ta/Ti/Si (**Figure 3.21d**) electrodes was further tested using the GCD method at a current density of 20 mA cm^{-2}. All these electrodes exhibit high and stable capacitances, as confirmed from the SEM images for these electrodes after long-term tests (e.g., 10000 GCD cycles at a current density of 20 mA cm^{-2}).

Further comparisons of the capacitor performance of BNDD/Ta/Ti/Si electrode reported by using other doping diamond-based electrode materials are summarized in **Table 3-2**. It can be concluded that such a modified co-doped diamond electrode exhibits better capacitor performance. Therefore, all these results confirm the suitability of co-doped diamond films grown on the metal interlayers for electrochemical energy storage.

Table 3-2 *Comparison of performance on different diamond-based electrodes. (As measured using a three-electrode system in 0.05 M $Fe(CN)_6^{3-/4}$ and 1.0 M Na_2SO_4.)*

Electrode	Capacitance	Lifetime	Ref.
BDD	41.51 mF cm^{-2} (10 mV s^{-1})	100% (6 000 cycles, 5 mA cm^{-2})	110
BDD network	73.42 mF cm^{-2} (10 mV s^{-1})	100% (12 000 cycles, 5 mA cm^{-2})	110
PDD (post-thermal treatment)	63.56 mF cm^{-2} (20 mV s^{-1})	-	13
TiC/BDD	42.6 mF cm^{-2} (10 mV s^{-1})	92% (10 000 cycles, 20 mA cm^{-2})	39
Porous BDD	78.23 mAh g^{-1} (10 mV s^{-1})	92.6% (5 000 cycles, 200 mV s^{-1})	111
NBD	87.8 mF cm^{-2} (10 mV s^{-1})	- (Stable after 10 000 cycles)	23
Graphite@NDD nanoneedles	66.65 mF cm^{-2} (10 mV s^{-1})	100.0% (10 000 cycles, 10 mA cm^{-2})	14
3D diamond/graphite	889 mF cm^{-2} (3 mA cm^{-2})	118.0% (50 000 cycles, 30 mA cm^{-2})	112
core-shell diamond-graphite hybrid nano-needles	190 mF cm^{-2} (3 mA cm^{-2})	96.1% (10 000 cycles, 3 mA cm^{-2})	113
sp^3 and sp^2 carbon hybrids	400 mF cm^{-2} (10 mV s^{-1})	95% (10 000 cycles, 3 mA cm^{-2})	114
BNDD/Ta/Ti/Si	**95.3 mF cm^{-2} (10 mV s^{-1})**	**100% (10 000 cycles, 20 mA cm^{-2})**	**This work**

3.4 Conclusions

The influence of interlayers on the electrochemistry of B,N-co-doped diamond films has been revealed experimentally and theoretically. The diamond films grown on a Ta/Ti/Si interlayer exhibited better electrochemical response toward inner-spherical and outer-spherical redox systems than those grown on a Si substrate and a Ti interlayer. The reasons behind are assumed to stem from its smaller electrochemical fitting resistance and its faster electron transfer rate. Additionally, the B,N co-doping effect further enhances electrochemical performance by optimizing the electronic structure, improving charge carrier density, and facilitating more efficient electron transfer at the electrode interface. The improvement of electrochemical performance of the BNDDTa/Ti/Si film is related to the smaller grain size and the presence of TaC between the Si and the diamond layer. This film is promising to be applied to the assembling of high-performance supercapacitors. Future work can be conducted in the fields of electrocatalysis where a low potential of the hydrogen evolution reaction is required, such as for electrochemical CO_2 reduction reaction (CO_2RR), and electrochemical nitrogen fixation. Meanwhile, such an electrode is attractive for environmental applications where a high potential of the oxygen evolution reaction is required (e.g., pollutant degradation).

Chapter 4. Cu_2O@CNF-BNDD composites for NO_3RR and Zn-NO_3^- batteries

Electrochemical nitrate reduction (NO_3RR), as a waste-to-resource strategy, offers an appealing solution for sustainable ammonia production, compared with the conventional energy-intensive Haber-Bosch process.[115,116] The design and synthesis of various electrocatalysts for NO_3RR has thus received widespread attention. These catalysts have been developed by means of numerous approaches, including alloying strategy,[117,118] crystal facet engineering,[119-121] defect engineering,[122-124] and heteroatom doping[125]. To study their NO_3RR performance, they have to be mixed with other materials (e.g., organic linkers, carbon black) to form catalyst inks which need to be cast onto the current collector (e.g., carbon paper,[126] carbon cloth,[127] carbon felt). It is obvious that this method significantly affects the performance and stability of the catalysts and the resultant electrodes, especially during continuous long-term ammonia production.[128] In this regard, it is crucial to design a highly stable collector that can better meet the needs of an actual production environment, or an integrated catalyst/electrode system, eventually extending the lifespan of catalysts/electrodes.

Among various current collectors, conductive diamond was selected in this thesis since sp^3-configured diamond has a unique combination of outstanding physical and chemical properties compared to other carbon materials and metals. For example, it possesses good stability, high corrosion resistance in harsh electrochemical environments.[129,130] Their extremely wide electrochemical potential windows, which are favorable for suppressing the HER and meanwhile the occurrence of side reactions is potentially reduced, further enhancing the selectivity for nitrate reduction and the Faraday efficiency of ammonia production.[131] However, the semi-conductive characteristics of diamond electrodes are disadvantageous to electron transfer and hinder efficient electrolysis/electronsynthesis processes.[132] In addition, diamond, as a thin film electrode material, usually has a small specific surface area. Namely, the

number of active sites on its surface is limited. A flat diamond film is thus not conducive to the effective adsorption and reduction reaction of nitrate.

Driven by these facts, novel strategies to fabricate high stability and effective diamond composite electrodes have been exploited and the applications of these electrodes for NO_3RR have also been examined. Namely, in this thesis, a three-dimensional structure (BNDD-CNF) was designed and constructed, combining a metal sandwich controlled co-doped diamond film with CNFs. Note that the electrochemical enhancement effect of the metal interlayer between diamond and a Si substrate has been confirmed.[40] Regarding to the BNDD-CNF structure, the covalent bond between sp^2-carbon (CNFs) and sp^3-diamond is expected to enable the formation of mechanically stable and well-conductive composites, ensuring stable performance of as-fabricated electrodes during long electrolysis processes.[133] In addition, the three-dimensional structure of the BNDD-CNF composite provides a multi-dimensional electron and ion transport path, an increased specific surface area or more active sites. Compared with a flat BNDD, the ammonia production on the BNDD-CNF composite is nearly 2 times higher, confirming the positive contribution of the 3D BNDD-CNF composite toward efficient nitrate reduction.

Despite this BNDD-CNF composite designed with the synergistic effect of "1+1 > 2" strategy improved both Faradaic Efficiency (FE) and NH_3 yield rates, its catalytic activity toward nitrate reduction is still low, probably steaming from the inherent limitations of pure carbon-based materials. In other words, co-catalysts need to be added onto such 3D BNDD-CNF composites. In this context, Cu_2O, a typical and efficient catalyst for nitrate reduction, was then deposited onto its surface with an aim to further improve Faraday efficiency (FE) and product selectivity for the nitrate reduction. As an extend application, the Zn-NO_3^- battery was assembled with the Cu_2O@CNF-BNDD as cathode, which can supply energy and convert NO_3^- to NH_3 concurrently.

4.1 Characterization of Cu_2O@CNF-BNDD

A strategy has been developed for the formation of CNF-BNDD and Cu_2O@CNF-BNDD. A metal interlayer has been added in these used BNDD films, as demonstrated previously. **Figure 4.1(a)** shows one typical SEM image of a BNDD film grown on a Ta/Ti/Si substrate, exhibiting the typical morphology of polycrystalline diamond, namely with clear and dense surface crystal grains. As a potential candidate for further applications, CNFs are grown on this BNDD in a TCVD reactor using Cu catalyst.[9] In this thesis, Cu-based catalyst was electrochemically deposited on BNDD. The SEM image of as grown CNFs on the BNDD is presented in **Figure 4.1(b)**, revealing their random growth, or fibers predominantly growing in two or more directions. The diameter of these CNFs is varied in the range from 300 to 400 nm and their length can reach up to a few micrometers. Subsequently, Cu_2O nanocubes were coated on the CNF-BNDD with aid of an electrochemical deposition technique. From its SEM image (**Figures 4.1c**), it is evident that Cu_2O particles exhibit a cubic morphology, of which size is around 50 nm. Moreover, the STEM mapping images (**Figure 4.2**) confirm homogeneous distribution of all elements inside Cu_2O@CNF, peeled from diamond surface.

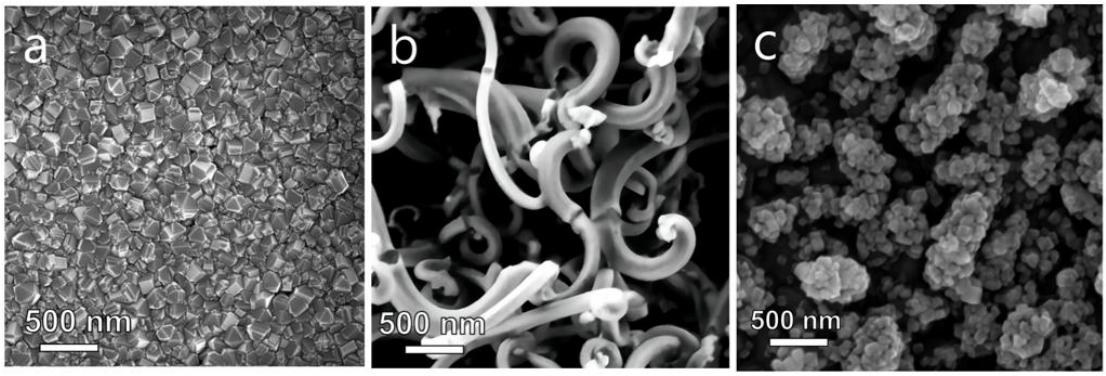


Figure 4.1 *SEM images of the (a) BNDD, (b) CNF-BNDD, (c) Cu_2O@CNF-BNDD.*

Raman spectroscopy was employed to analyze the phase structures of both CNF-BNDD and Cu_2O@CNF-BNDD composites (**Figure 4.3**). In both Raman spectra, three major Raman bands are noticed: a BNDD peak at $\approx$ 1310 cm^{-1}, a *D*

band at ≈ 1370 cm^{-1} and a *G* band at ≈1650 cm^{-1}. All of them are clearly related to CNF-BNDD.[134-136] In addition, the presence of Cu_2O was confirmed in the spectrum of Cu_2O@CNF-BNDD composite, with Cu_2O peaks at 147 cm^{-1}, 228 cm^{-1} and 638 cm^{-1}. [137,138]

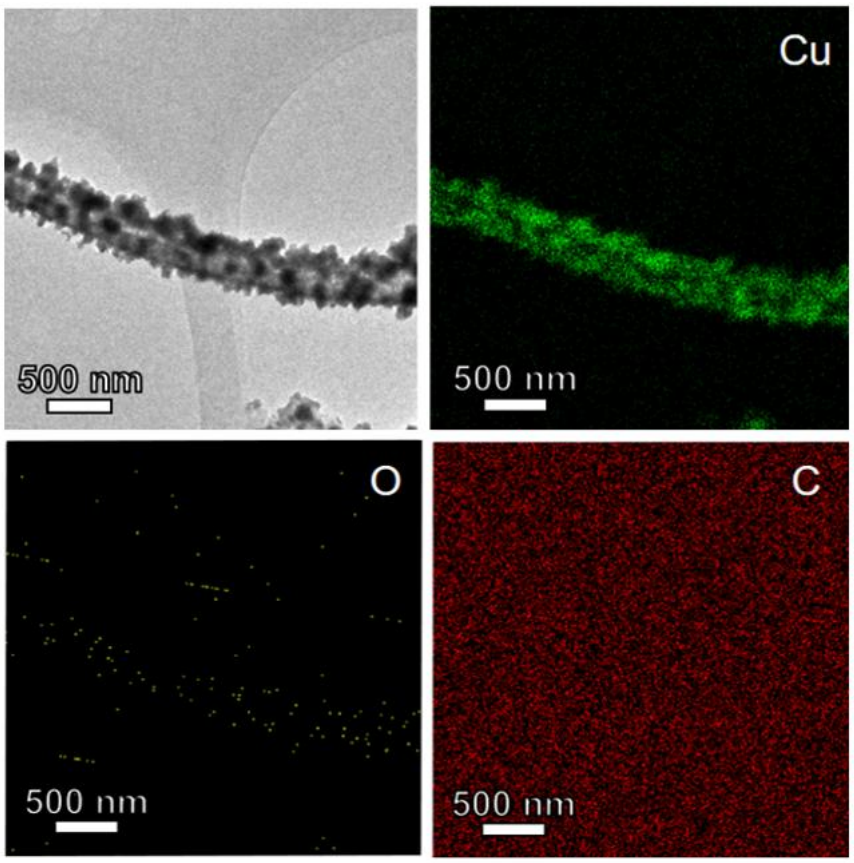


Figure 4.2 *STEM mapping of Cu, O, and C elements in Cu_2O@CNF*

Their micro-X-ray diffraction (μ-XRD) patterns were also collected (**Figure 4.4**), where the diffraction peaks at 43.9° and 78.1° are indexed to the (111) and (220) planes of diamond, respectively.[139] The peak at 51.5° is ascribed to graphite.[140] Three peaks at 50.8°, 59.3°, and 88.7° are attributed to the (111), (200), and (220) planes of Cu (JCPDS 70-3038), respectively. This is because Cu acts as the catalyst for the CNF growth.[141] Moreover, in the XRD pattern of the Cu_2O@CNF-BNDD composite (the inset in **Figure 4.4**) Cu_2O (111) and (200) peaks are visible at 42.6° and 49.5° (JCPDS 77-0199).[142] Note that some minor features of CuO are also observed for the Cu_2O@CNF-BNDD composite, such as the Raman peaks of CuO at 288 cm^{-1},

336 cm^{-1}, and 630 cm^{-1}. In its μ-XRD patterns, two peaks corresponding to CuO are identified at 42.3° and 49.8°, associated with the (111) and (200) planes, respectively (JCPDS 78-0428). The presence of CuO probably results from the oxidation of Cu_2O nanoparticles when their exposure to air.

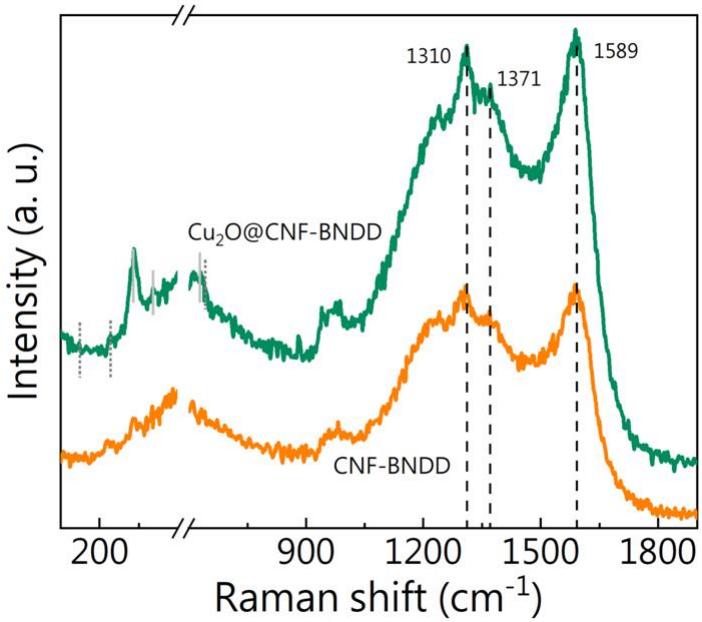


Figure 4.3 Raman spectra of CNF/BNDD and Cu_2O@CNF-BNDD.

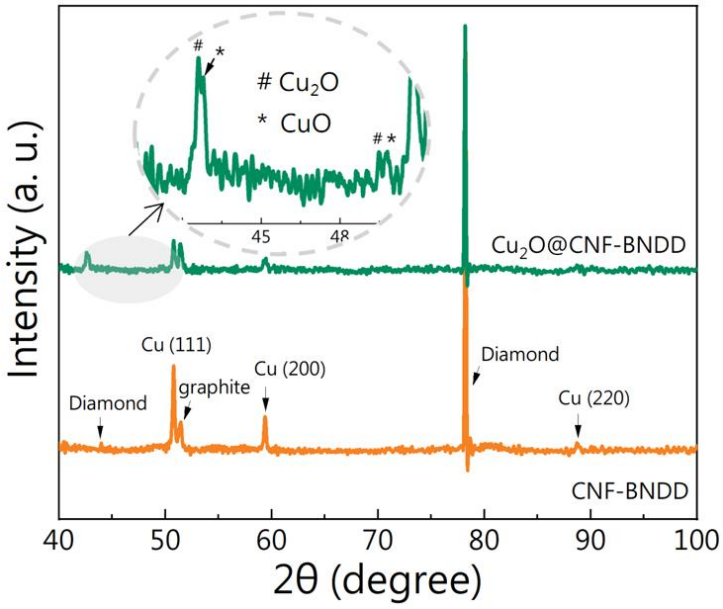


Figure 4.4 μ-XRD patterns of CNF/BNDD and Cu_2O@CNF-BNDD.

4.2 Electrochemical NO_3RR performance of Cu_2O@CNF-BNDD

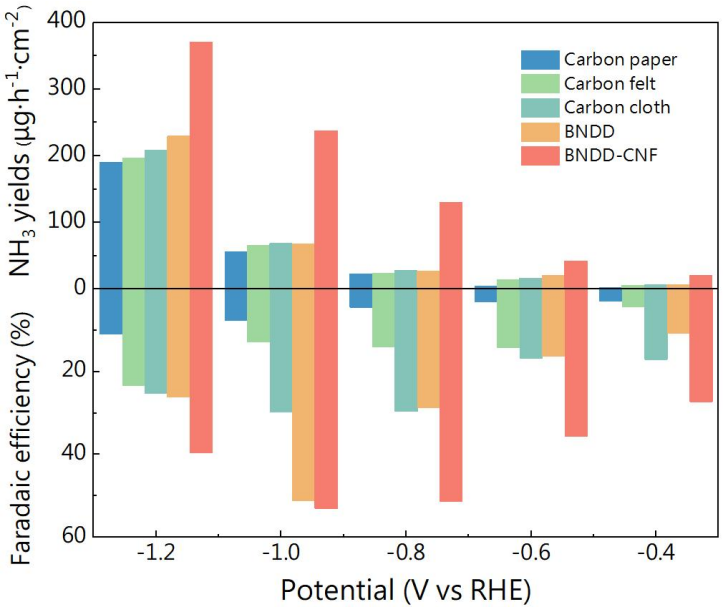


Figure 4.5 *NH_3 yield rates and FEs of BNDD, CNF-BNDD and several other electrodes toward nitrate reduction.*

To investigate the electrocatalytic activity and kinetics of NO_3RR of above-mentioned electrodes, various electrochemical measurements were conducted in 0.5 M Na_2SO_4 electrolyte inside a H-type cell where a three-electrode system was placed. Their activity of the NO_3RR was evaluated by product analysis with aid of long-term electrolysis processes, namely *i-t* tests at different potentials for 2 h. In more detail, the concentrations of reactants and products (nitrate and ammonia) were quantified by well-established colorimetric methods (or using UV-vis spectroscopy). The preparation of calibration curves for each reactant were already described in the experimental section. The NH_3 yield and its Faradaic efficiency (FE) on BNDD, CNF-BNDD and several other electrodes which utilize other carbon-based collectors (e.g., carbon paper, carbon flet, carbon cloth) were estimated and compared (**Figure 4.5**). On all these electrodes the NH_3 yield gradually increases when the potential is changed from -0.4 to -1.2 V (vs. RHE). On the CNF-BNDD, the ammonia production is 370.7 μg h^{-1} cm^{-2} at -1.2 V, which is nearly 2 times higher compared with BNDD. While the FE of ammonia on the CNF-BNDD exhibits a volcanic shape curve and

reaches the maximum value of 53.0% at −1.0 V (vs. RHE). When the potential continues increasing lower than -1.2 V, charge consumption by the HER starts severely occuring.[143] In short, the BNDD-CNF has a positive effect on improving ammonia production.

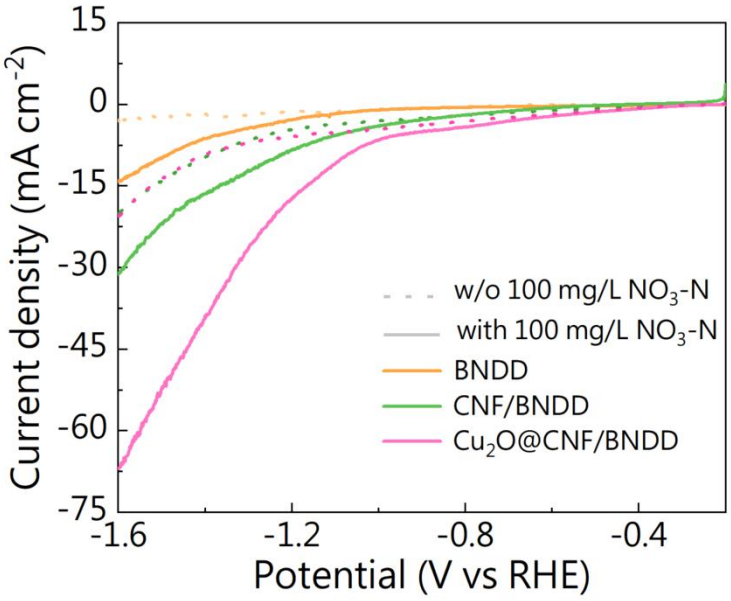


Figure 4.6 *LSVs of different electrodes in 0.5 M Na_2SO_4 before and after the addition of 100 mg L^{-1} NO_3^--N at a scan rate of 5 mV s^{-1}.*

The electrochemical activity of NO_3RR on the Cu_2O@CNF-BNDD electrode, of which characterization has been shown previously, was then evaluated and compared with other electrodes. **Figure 4.6** shows their linear sweep voltammetry curves under conditions with and without nitrate (NO_3^--N). On all electrodes in pure 0.5 M Na_2SO_4 electrolyte without nitrate (dashed lines), the current response is very small, showing a high overpotential for HER. In contrast, when nitrate is added to the electrolyte (solid lines) a significant increase in current density is seen when the potential is negative than -0.6 V (vs. RHE). This difference indicates the occurrence of the nitrate reduction reaction. On the Cu_2O@CNF/BNDD electrode (pink line), the current density is the highest. Particularly when potentials are below -1.0 V, the current density increases rapidly, demonstrating its superior catalytic activity for nitrate reduction.

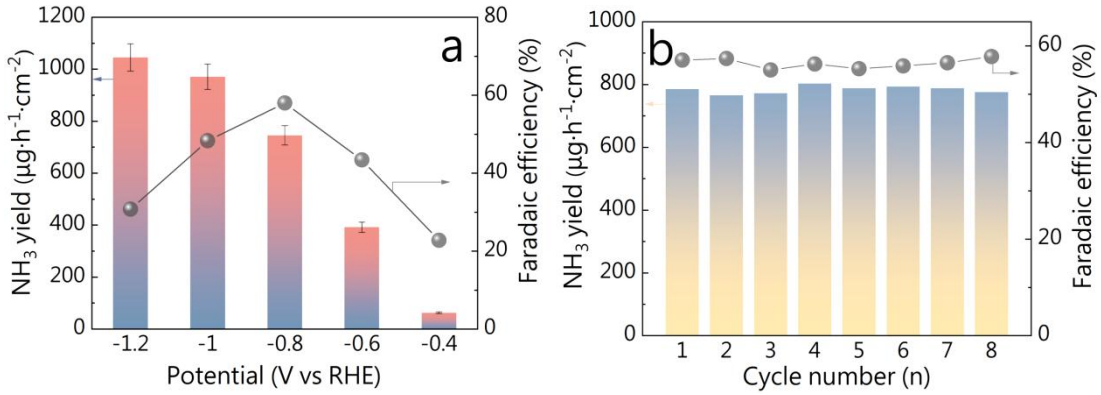


Figure 4.7 *(a) The NH_3 yields and FEs of the* Cu_2O@CNF/BNDD electrode *in* 0.5 M Na_2SO_4 after the addition of *100 mg L^{-1} NO_3^--N at different potentials as well as (b) their variation as function of cycle number.*

To gain deep insight into the catalytic performance of the Cu_2O@CNF/BNDD electrode toward the NO_3RR, its NH_3 yields and FEs were analyzed at various and constant potentials (**Figure 4.7a**). It manifests a significant NH_3 yield up to 1045 $\mu g \cdot h^{-1} \cdot cm^{-2}$ at −1.2 V (vs. RHE), while the highest FE is 58.1% at −0.8 V (vs. RHE). Furthermore, both the NH_4^+ yield rate and the FE present minor fluctuations during five consecutive cycles (**Figure 4.7b**), indicating the excellent stability of the Cu_2O@CNF/BNDD electrode.

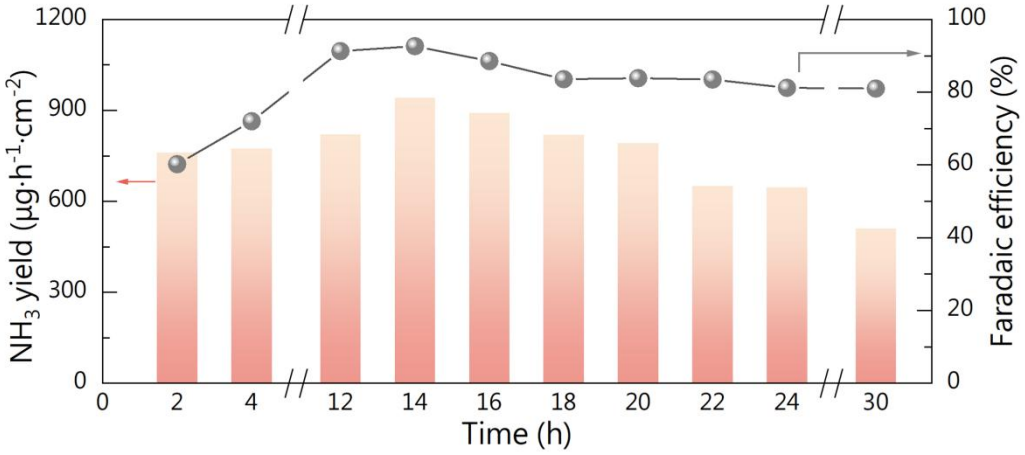


Figure 4.8 *The variation of the NH_3 yields and FEs of the Cu_2O@CNF/BNDD electrode in 0.5 M Na_2SO_4 after the addition of 100 mg L^{-1} NO_3^--N at -0.8 V as function of electrolysis time.*

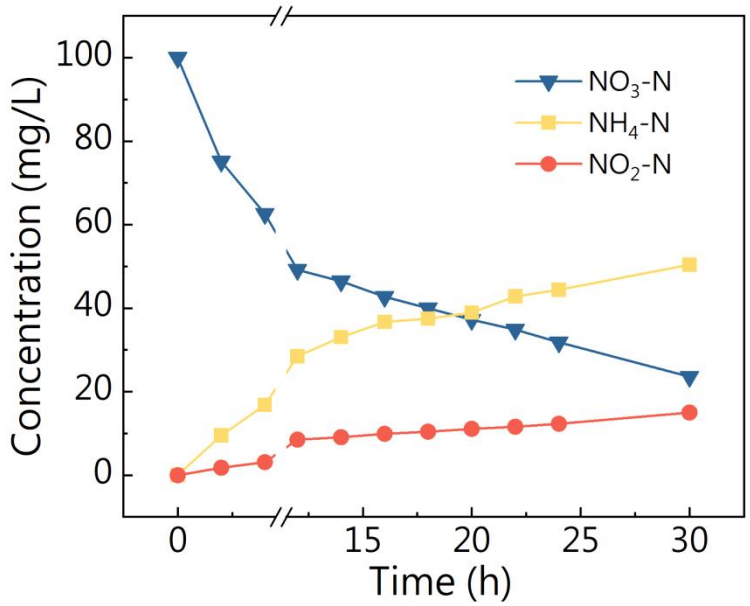


Figure 4.9 *Nitrate conversion during 30 h long-term reduction with 100 mg/L NO_3^--N.*

The efficiency of nitrate removal and electrode stability during a continuous prolongated process were further evaluated through complete nitrate electroreduction conducted at -0.8 V using the solution with 100 mg L^{-1} NO_3^--N (**Figure 4.8**). This consecutive stability measurement reveals both the ammonia yield rate and FE steadily increase within the first12 h; a highest yield rate of 941.72 $\mu g \cdot h^{-1} \cdot cm^{-2}$ and the biggest FE of 92.6% are obtained after 14 h; they then decline, probably because of the nitrate depletion. For such a long-term electrolysis process (namely within 30 h), 77% nitrate conversion was achieved (**Figure 4.9**).

The characterization of Cu_2O/CNF-BNDD electrodes was conducted after its application of electrolysis for about 30 h. These results were further compared with one before such electrolysis experiments. Before such tests, one can see clearly in its TEM image and SAED pattern (**Figure 4.10a**) some typical crystallographic features of cuprous oxide (Cu_2O). The interplanar spacings (0.306 nm, 0.249 nm, 0.215 nm, and 0.182 nm), corresponding to the (110), (111), (200), and (220) planes of Cu_2O, respectively, indicate high crystallinity and a typical polycrystalline structure of Cu_2O.

After a long-term electrolysis test, its cubic morphology is no longer retained, reconstructing into smaller, irregularly shaped nanoparticles (**Figure 4.10b**). Their sizes are ranging from tens to hundreds of nanometers, presenting a polycrystalline or aggregate structure. Their SAED pattern shows typical polycrystalline diffraction rings, with measured interplanar spacings (e.g., 0.112 nm, 0.132 nm, 0.19 nm, 0.21 nm, 0.36 nm), corresponding to the characteristic planes of metallic copper, such as (111), (200), and (100). In short, the reconstruction of Cu_2O to Cu happens during the long-term NO_3RR, similar as those reported during long-term electrochemical CO_2 reduction on Cu_2O catalysts.

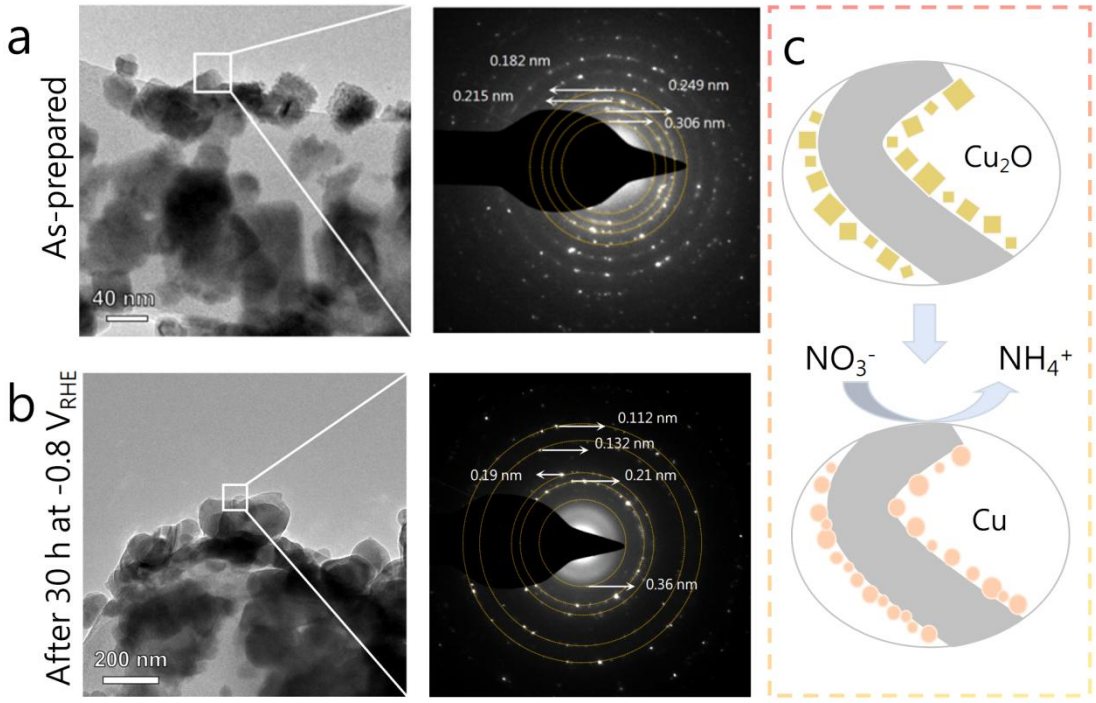


Figure 4.10 *TEM images and SAED patterns of Cu_2O on the CNF-BNDD (a) before and (b) after 30 h NO_3RR. (c) schematic of the reconstruction of Cu_2O to Cu.*

To obtain more evidence, XPS analysis of the Cu 2p spectrum of a Cu_2O@CNF-BNDD electrode before and after 30 h NO_3RR was carried out (**Figure 4.11**). Before this test, its XPS spectrum exhibits distinct Cu^{2+} and Cu^{+} peaks, especially for Cu $2p_{3/2}$ and $2p_{1/2}$, which are located at approximately 935 eV and 955 eV, respectively. The prominent Cu^{2+} (blue) and Cu^{+} (green) peaks at the $2p_{3/2}$

position suggest the presence of both CuO and Cu_2O. The presence of satellite peaks (Sat.) further confirms the Cu^{2+} signals associated with CuO. After the reaction, the Cu^{2+} peak nearly disappears in its XPS spectrum and only a weak Cu^{+} signal is left, indicating that CuO is almost completely reduced. The most significant feature is the emergence of a Cu^0 $2p_{3/2}$ peak at approximately 933 eV and a Cu $2p_{1/2}$ peak at approximately 953 eV. Furthermore, the disappearance of the satellite peaks corroborates the near-complete reduction of Cu^{2+}. In summary, Cu_2O is believed to be gradually reduced to metallic copper (Cu^0) nanoparticles, aligning with the reports in other studies.[144,145]

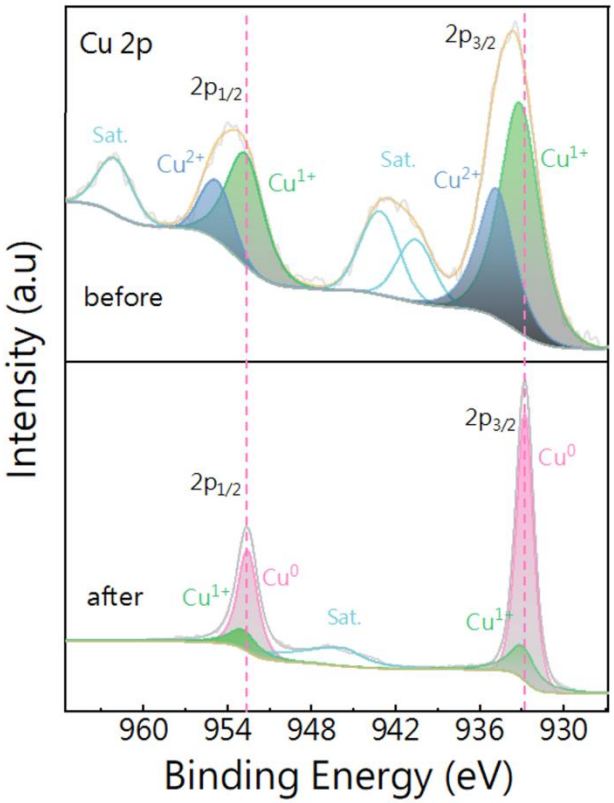


Figure 4.11 *XPS spectra of Cu 2p for a Cu_2O@CNF-BNDD electrode before and after 30 h NO_3RR.*

4.3 DFT simulations

To further reveal that the reconstructed Cu^0 is the active site for nitrate reduction reaction or the NO_3RR mechanism, DFT calculations were performed. In the first step, the interface features of a Cu_2O@CNF-BNDD electrode were examined. Here, Cu_2O

(100) and Cu (111) facet models were constructed. The choose of these two facets is because they were proved to be the most active facets for NO_3RR in neutral environment.[146,147] As shown in **Figure 4.12** (**a**), the lattice constant of Cu (111) is 2.56 Å, whereas the nearest Cu-Cu bond in Cu_2O (100) is 2.36 Å and the Cu-O bond is 1.91 Å. To analyze the electronic structure of surface Cu atoms, 3*d* electronic states of Cu_2O (100) and Cu (111) were calculated (**Figure 4.12b**). According to the *d*-band center theory proposed by Nørskov et al.[148], the *d*-band center of Cu (111) is shifted to -2.47 eV, while that of Cu_2O (100) is at -1.94 eV, indicating that Cu (111) has a lower adsorption to intermediates.

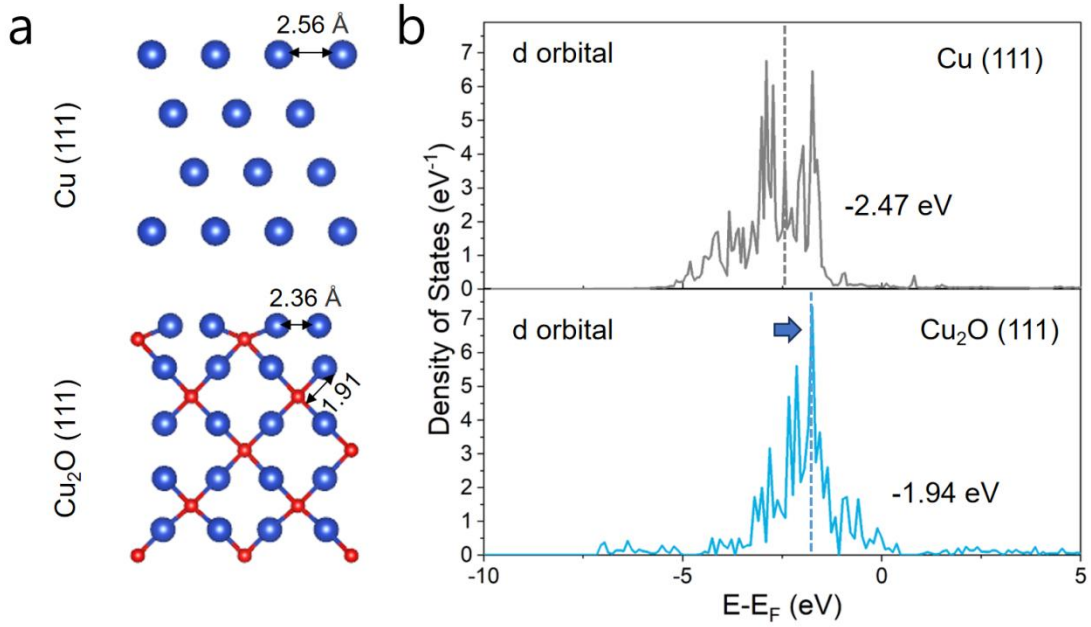


Figure 4.12 *(a) Constructed models of Cu_2O (100) and Cu (111), (b) Cu 3d orbitals projected density of states and d-band centers of Cu_2O (100) and Cu (111).*

The speculated reaction pathways of NO_3RR on Cu_2O (100) and Cu (111) are then hypothesized as: $NO_3^- \rightarrow *NO_3 \rightarrow *NO_2 \rightarrow *NO \rightarrow *N \rightarrow *NH \rightarrow *NH_2 \rightarrow *NH_3 \rightarrow NH_3(g)$, according to reported minimize energy barriers (**Figure 4.13**).[146,149] Note that all adsorption sites were calibrated to the minimum value, ensuring the accuracy of subsequent energy calculations of each step.

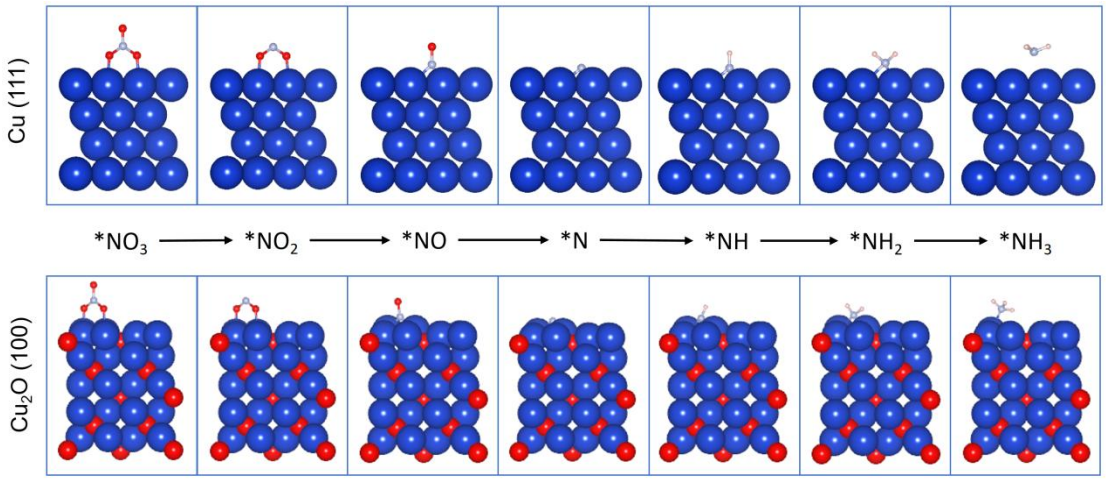


Figure 4.13 *Reaction pathways of NO_3RR on Cu (111) and Cu_2O (100).*

Table 4-1 *Adsoprtion Gibbs free energy along the NO_3RR pathways on Cu_2O (100) in solutions with pH = 0 and 7.*

	*E** (eV)	*G** (eV)	Δ*G** (eV)	pH = 0 (eV)	pH=7 (eV)
slab	-271.60	-271.60	-2.69	-2.69	-2.69
NO_3	-297.66	-297.33	-2.02	-4.71	-3.89
NO_2	-292.10	-291.93	-1.34	-6.05	-4.41
NO	-285.95	-285.85	0.03	-6.02	-3.56
N	-278.47	-278.40	-1.83	-7.85	-4.98
NH	-283.98	-283.63	-1.53	-9.39	-6.11
NH_2	-289.18	-288.57	0.74	-8.64	-4.95
NH_3	-292.12	-291.22	0.09	-8.55	-4.45

After the structural optimization, the adsorption Gibbs free energy on different surface sites were determinate using the equation of:

$\Delta G^* = \Delta E^* + \Delta ZPE - T\Delta S$

where ΔE^* is the energy change during nitrate reduction process. ΔZPE and ΔS are the difference in zero-point energy and entropy, respectively. T is the system temperature (298.15 K, in our calculation). For intermediates adsorbed on different surface sites, all 3N degrees of freedom are treated as vibrational motions while neglecting the contributions from the material surfaces. The ΔG^* was calculated using the Vaspkit software[150] from ΔE^*, T and calculated vibrational energy. The used pH calibration method was referenced to the one reported.[146] All the original data are listed in **Table 4-1 and 4-2**.

Table 4-2 *Gibbs free energy along the NO_3RR pathways on Cu (111) in solutions with pH = 0 and 7.*

	E^* (eV)	G^* (eV)	ΔG^* (eV)	pH=0 (eV)	pH=7 (eV)
slab	-138.77	-138.77	-2.13	-2.13	-2.13
NO_3	-164.27	-163.95	-1.90	-4.03	-3.21
NO_2	-158.64	-158.49	-1.10	-5.13	-3.49
NO	-152.26	-152.11	-0.73	-5.86	-3.40
N	-145.47	-145.41	-1.23	-7.09	-4.22
NH	-150.40	-150.05	-0.55	-7.65	-4.37
NH_2	-154.62	-153.92	-0.92	-8.56	-4.87
NH_3	-159.18	-158.24	-0.06	-8.62	-4.52

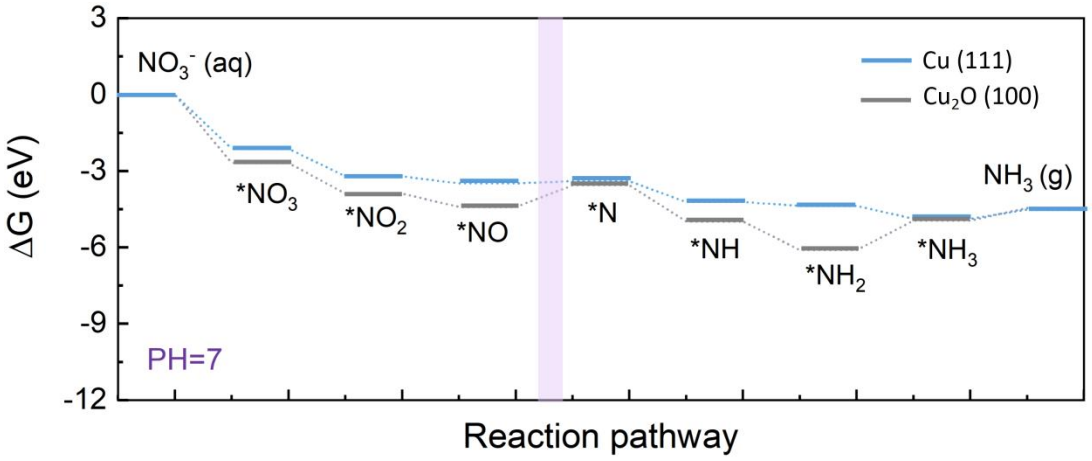


Figure 4.14 *Adsorption Gibbs energy of different intermediates during NO_3RR on the active site of Cu_2O (100) and Cu (111) in solutions with pH = 7.*

Furthermore, the Gibbs energies of different intermediates along the nitrate reduction reaction have been calculated in neutral electrolyte (pH=7). For Cu_2O (100), there exists two energy barriers: *NO-*N (0.88 eV) and $*NH_2$-$*NH_3$ (1.11 eV). On Cu (111) facet, the NO_3RR is always spontaneous and there is only a small energy barrier of 0.15 eV (**Figure 4.14**). This may be due to the strong adsorption of *NO and $*NH_2$ on Cu_2O (100) or the difficulty to desorb them from the catalyst surface. Consequently, a Cu (111) facet featuring an optimal *d*-band center has the lowest overpotential towards NO_3RR, indicating that it is the main active site for the NO_3RR on the reconstructed surface. Such assumption based on these DFT results is in line with the observation in their TEM images.

4.4 Rechargeable Zn-nitrate batteries

Nowadays, the energy crisis is one of the most pressing challenges faced by humanity. To address this, energy storage is thus becoming crucial. Among various energy storage strategies, electrochemical energy storage by use of devices such as supercapacitors and batteries have been proved to be extremely promising, due to high energy density, efficiency, and scalability of these electrochemical devices.[151] For example, lithium-ion, sodium-ion, and potassium-ion batteries have garnered extreme

attention and have witnessed extensive applications in portable electronics, electric vehicles, and grid storage.[151] However, these systems have shortcomings such as metal resource scarcity, their safety concerns, and their long-term environmental impact.[152] Very recently, zinc battery, which either harnesses a zinc metal plate or zinc ions as the primary active material, has been considered as their promising alternative, thanks to abundant and non-toxic zinc materials, excellent safety profiles of these batteries, and their cost-effectiveness. For example, zinc batteries can operate in aqueous electrolytes, reducing the risk of fire hazards associated with organic solvents in lithium-ion batteries.[153] Additionally, they exhibit a long cycle life and are highly versatile in their applications. Taking a Zn-nitrate battery as an example, it leverages nitrate ions (NO_3^-) in the electrolyte, enabling efficient energy storage and under specific conditions electrochemical conversion of nitrate waste into valuable chemicals.[154] This multifunctional capability positions Zn-nitrate batteries as a cutting-edge solution with significant potential in energy storage and environmental applications.[155]

Motivated by the excellent NO_3RR performance on the Cu_2O@CNF-BNDD electrode, a "two birds with one stone" strategy was applied to construct a Zn-NO_3^- battery, where Cu_2O@CNF-BNDD was used as the cathode and a Zn plate as the anode. The chemical energy of zinc metal can drive the cathode NO_3RR to produce NH_3 as well as output electrical power. In this Zn-NO_3^- battery system, 3 M KOH was used at the anode and 0.5 M Na_2SO_4 + 100 mg L NO_3-N^{-1} was at the cathode. A Nafion 117 membrane was added to separate two cells (**Figure 4.17a**). The maximum power density of such a Zn-NO_3^- battery reaches 2.75 mW cm^{-2} (**Figure 4.17b**). Furthermore, it is very stable at different current densities, as confirmed from its the time-dependent discharging curves (**Figure 4.17c**). where the increase of the current density from 0 mA cm^{-2} to 10 mA cm^{-2} only generates the stepped voltage profiles with a stable discharge plateau. In this battery, its FEs and NH_3 yield were detected at different discharging current densities with an electrolysis time of 1 h. As shown in

Figure 4.17d, NH_3 yield increases with a bigger current density, and FE reaches the highest value of 36.14% at a current density of 8 mA cm^{-2}. This Zn-NO_3^- battery shows an open-circuit voltage (OCV) of 1.904 V (**Figure 4.18**), the theoretical voltage of 1.907 V. Therefore, the Cu_2O@CNF-BNDD based Zn-NO_3^- battery efficiently converts nitrate to ammonia at ambient conditions and meanwhile is a potential energy storage device.

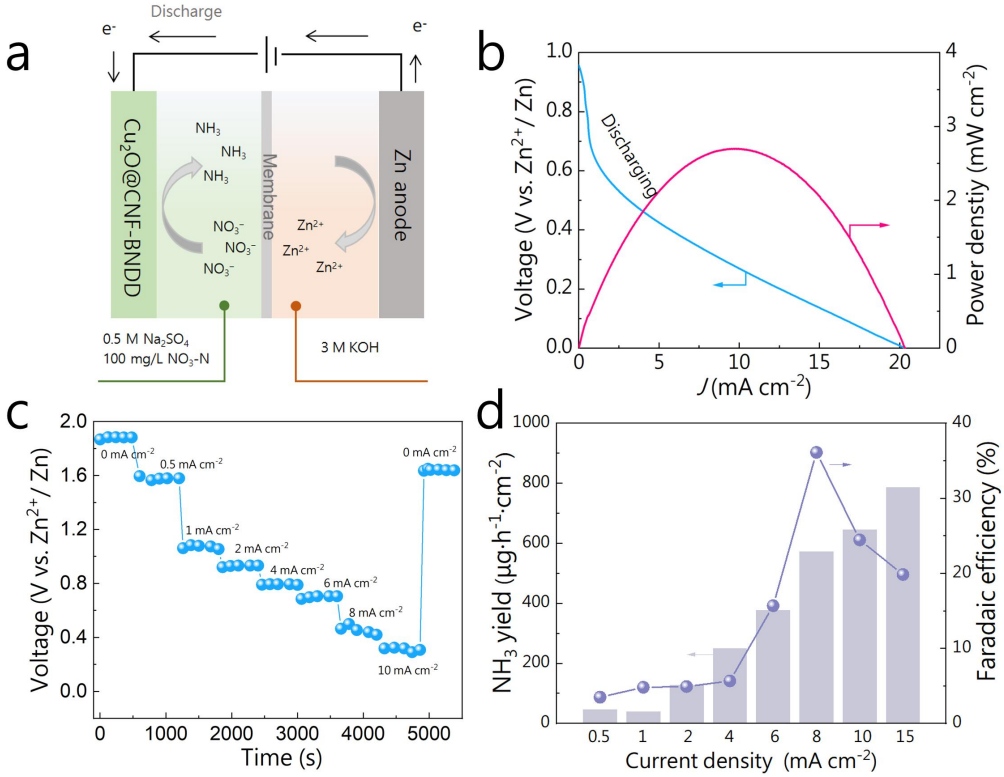


Figure 4.17 *(a) Schematic illustration of a Zn-NO_3^- battery. (b) Discharging polarization curves and the resulting power densities of this battery. (c) Chronoamperometric response at varied current densities. (d) NH_3 yields and corresponding FEs at varied current densities of a Zn-NO_3^- battery.*

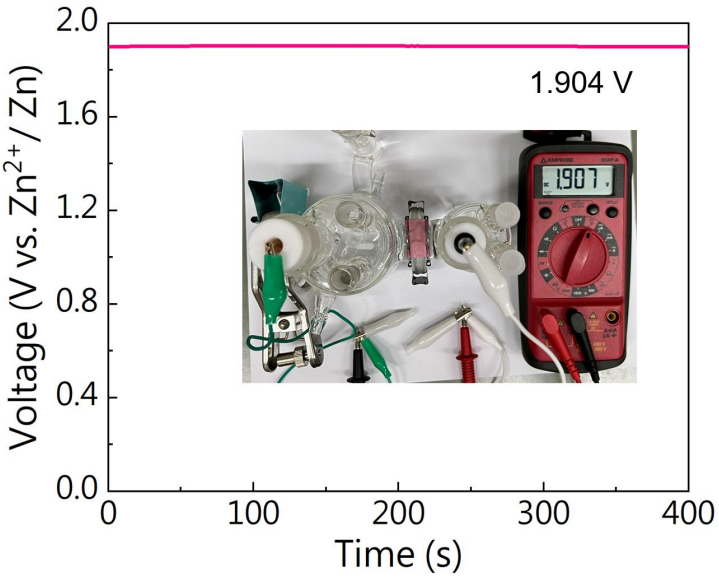


Figure 4.18 *The OCV measurement of a Zn-nitrate battery using a Cu_2O@CNF-BNDD electrode.*

4.5 Conclusions

In summary, a Cu_2O@CNF-BNDD electrode has been successfully designed and applied for efficient electrochemical nitrate reduction reaction (NO_3RR). The unique combination of boron and nitrogen co-doped diamond (BNDD) with carbon nanofibers (CNFs) and Cu_2O nanoparticles plays a critical role in enhancing the NO_3RR performance. The Cu_2O component, with its favorable electron donation properties, significantly boosts NO_3^- adsorption and reduction efficiency, while the BNDD provides mechanical stability and resistance to HER side reactions. The integration of CNFs with the BNDD film improves electrical conductivity and increases the electrode's active surface area, further enhancing the catalytic performance. The Cu_2O@CNF-BNDD catalyst delivers a high ammonia yield of 1056 $\mu g \cdot h^{-1} \cdot cm^{-2}$ and an impressive Faradaic efficiency of 92.6%. Our results indicate that during the electrochemical nitrate reduction reaction (NO_3RR), Cu_2O transforms into Cu nanoparticles after 30 hours of reaction. This transformation may promote reaction kinetics and enhances catalytic activity. This conclusion is further supported by density functional theory (DFT) simulations, which reveal that the

optimized *d*-band center of -2.46 eV on Cu nanoparticle active sites reduces the overpotential from 1.11 eV to 0.15 eV. This reduction further lowers the activation energy, accelerates reaction kinetics, and improves nitrate adsorption, contributing to the system's overall efficiency. The proposed Zn-NO_3^- battery system further exemplifies the potential of this electrode for practical applications, demonstrating both efficient energy conversion and NH_3 production with a maximum power density of 2.7 $mW \cdot cm^{-2}$. This work provides a potential pathway for repurposing waste nitrate as a resource for ammonia synthesis, with implications for sustainable energy conversion systems. While these findings are promising, they serve as an initial step toward further exploration and application in the fields of electrochemical nitrate reduction and energy storage technologies.

Chapter 5. NO_3RR using electrons generated from MO oxidation

A typical electrocatalytic NO_3RR system includes a cathodic NO_3RR and anodic oxygen evolution reaction (OER, >1.23 V vs. RHE).[156] As a kinetically sluggish, multi-step reaction, OER typically requires a significant overpotential, resulting in reduced reaction efficiency and increased energy consumption.[157] This poses a significant bottleneck for the broader applications of the NO_3RR. Therefore, improving the overall efficiency and economic viability of NO_3RR necessitates innovative strategies focused on optimizing the anodic reaction.[158] In other words, to fully utilize the electrical energy, the OER is better to be replaced with another kinetically favorable oxidation reaction such as oxidation of pollutants which will meanwhile generate value-added products during such oxidation processes.[159-161]

Therefore, in this thesis, traditional OER was replaced with the photoelectrocatalytic oxidation of a model organic pollutant - methyl orange (MO). The reason behind is that unlike OER, the photoelectrocatalytic oxidation of MO is kinetically faster and less energy-intensive.[162] This dual-purpose strategy integrates waste treatment and resource recovery into a powerful electrochemical system, significantly enhancing both environmental benefits and system functionality.

In this integrated system, electrons are generated at the anode through the oxidation/degradation of MO, while the cathode utilizes these electrons to efficiently reduce nitrate to ammonia. Specifically, the cathode employs Cu_2O@CNF-BNDD composite electrode, of which carefully designed structure significantly enhances catalytic activity and selectivity for nitrate reduction, minimizing the formation of undesirable byproducts. Meanwhile, the anode, made of BNDD/Ti/Si-3, facilitates the efficient oxidation of MO molecules, but also provides a stable and effective electron transport pathway. This synergistic design ensures high electron transfer efficiency between the anode and cathode, enabling the entire electrochemical system to operate

with remarkable efficiency and reduced energy consumption.

5.1 Characterization of BNDD/Ti/Si films

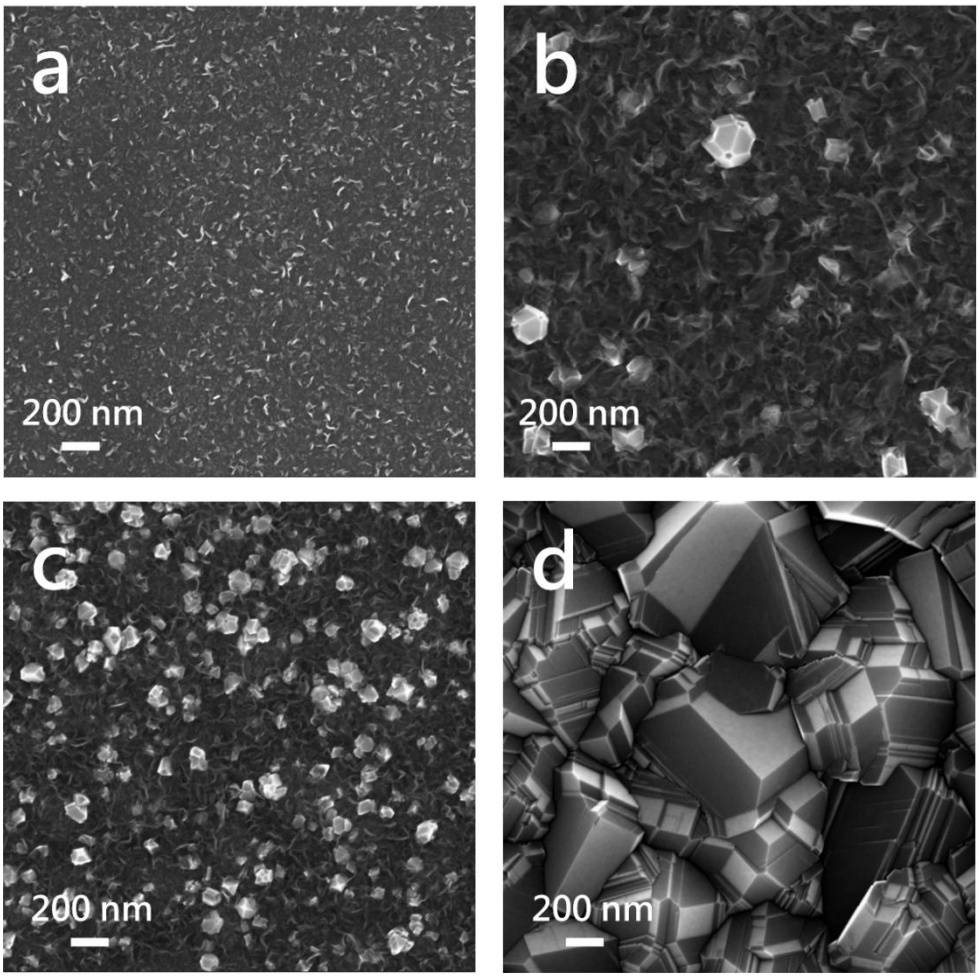


Figure 5.1 *SEM images of a BNDD film with different growth times on a Ti/Si substrate: (a) BNDD/Ti/Si-1 (0.50 h), (b) BNDD/Ti/Si-2 (0.75 h), (c) BNDD/Ti/Si-3 (1.5 h), (d) BNDD/Ti/Si-4 (16.5 h).*

The growth a BNDD film on a Ti/Si substrate has been tested as different growth times. From their SEM images (**Figure 5.1**), one can find a gradual increase in the coverage of diamond nanoparticles on the Ti layer and the corresponding evolution of surface morphology. It is obvious that as the coverage increases, both the number of particles and the surface coverage density progressively rises, eventually forming a complete, dense, and close structure. In more detail, at an initial stage the surface is

nearly free of particles **(Figure 5.1a**), exhibiting smooth appearance. With an increase of growth time, sparse diamond nanoparticles begin to appear (**Figure 5.1b**), leading to the diamond growth. A prolonged growth time makes the number of particles increase significantly, with a more uniform distribution and denser surface coverage (**Figure 5.1c**). Finally, the surface is entirely covered by diamond particles (**Figure 5.1d**), which have grown into a continuous polyhedral diamond film, forming a highly compact and pin-hole free structure. This progression demonstrates that as the coverage of diamond nanoparticles increases, the morphology evolves from sparse distribution to a densely packed and fully covered structure. Notably, as the growth time increases, the particle size is enlarged, transitioning from approximately 200 nm (**Figure 5.1b, c**) to micrometers (within a range of 0.5–1 μm, **Figure 5.1d),** again an indication of the correlation between growth time and particle morphology evolution.

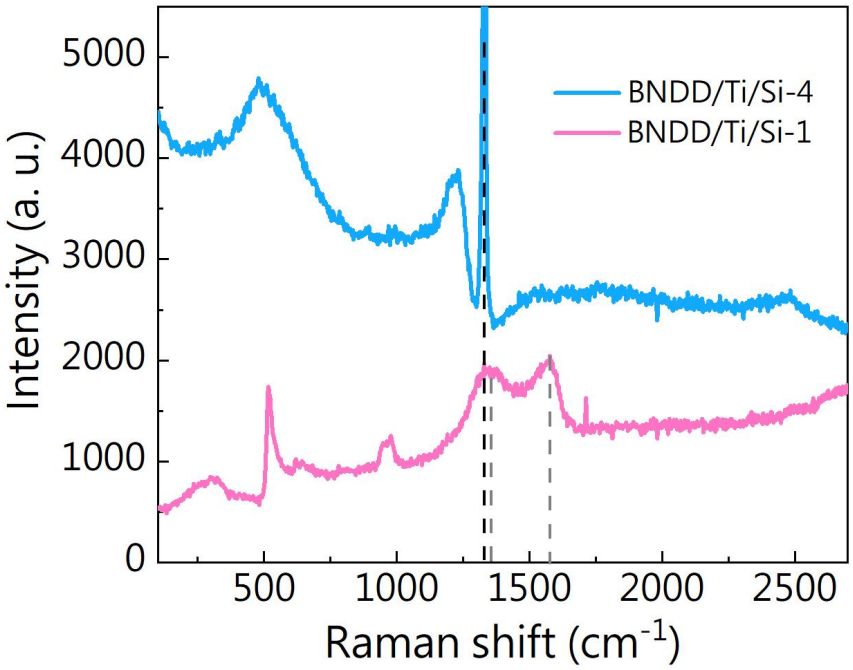


Figure 5.2 *Raman spectra of* BNDD/Ti/Si-1 *and* BNDD/Ti/Si-4.

The Raman spectra of one initial film — BNDD/Ti/Si-1 (pink curve) and final BNDD film - BNDD/Ti/Si-4 (blue curve) were recorded (**Figure 5.2**). It is important to note that the spectra of BNDD/Ti/Si-2 and BNDD/Ti/Si-3 are not fully represented

here because diamond nanoparticles on their surfaces directly reflect the laser signal, making it challenging to effectively collect related Raman data. In the Raman spectrum of a BNDD/Ti/Si-4 film (blue curve) there exhibits a sharp and intense peak at 1332 cm^{-1}. It is the hallmark of sp^3-bonded diamond and indicates high crystallinity of this BNDD film. In addition, a weak and broad peak in the 1500-1600 cm^{-1} region is observed adjacent to the 1332 cm^{-1} peak, likely corresponding to graphitic carbon or sp^2-bonded impurities. However, the relatively low intensity of this peak suggests that minor content of such an impurity. In other words, the BNDD film predominantly consists of high-quality sp^3-bonded diamond.

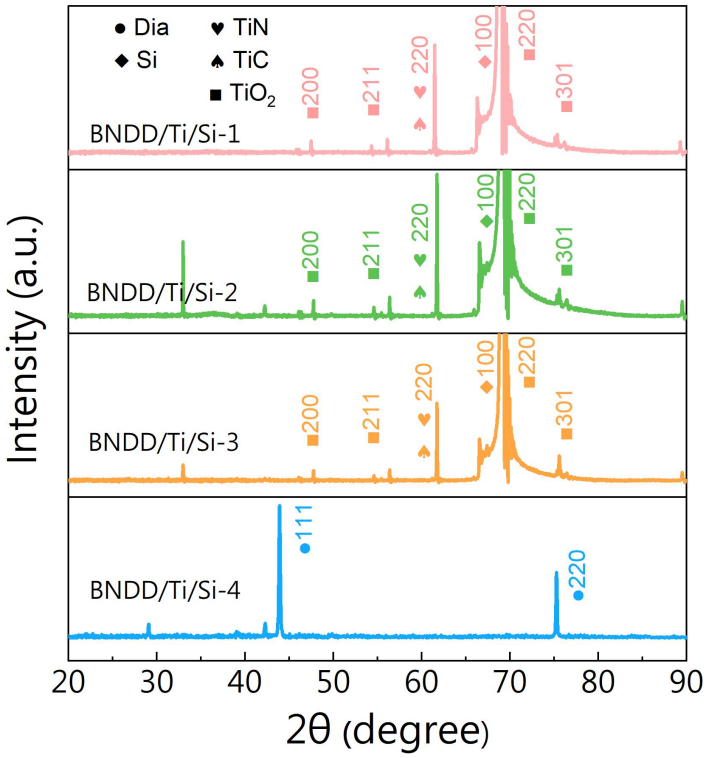


Figure 5.3 *XRD pattern of BNDD with different cover range on Ti/Si substrate.*

In contrast, the Raman spectrum of the BNDD/Ti/Si-1 (pink curve) lacks the prominent diamond Raman peak at 1332 cm^{-1}, indicating an absence of crystalline diamond structure in this sample. Therefore, there is little or even no sp^3-bonded diamond presented. The broad peak in the range of 700 to 900 cm^{-1} along with additional broad features around 1350 and 1580 cm^{-1} verifies that this sample is

primarily composed of amorphous materials, in line with the characterization results of different BNDD/Ti/Si samples using EELS in Section 3.1.1. Meanwhile, the presence of TiN, TiC, or TiO_2 is implied, while their Raman signals are not pronounced. This is because TiC typically shows a broad peak in the wavenumber of 700-900 cm^{-1}, simply overlapping with amorphous components in this sample. For TiN, it generally exhibits weak but broad background signals that are difficult to clearly differentiate *via* Raman spectroscopy. In addition, TiO_2 might contribute weak Raman signals in the lower frequency range, but these are generally not prominent. Conversely, the broader features around 1350 and 1580 cm^{-1} in the Raman spectrum of the BNDD/Ti/Si-1 strongly indicate the presence of amorphous carbon. These peaks are known to correspond to the *D*-band and *G*-band of disordered and graphitic carbon, respectively. Based on the Raman characteristics, amorphous carbon appears to dominate, while the contributions of TiC and TiN are likely less pronounced.

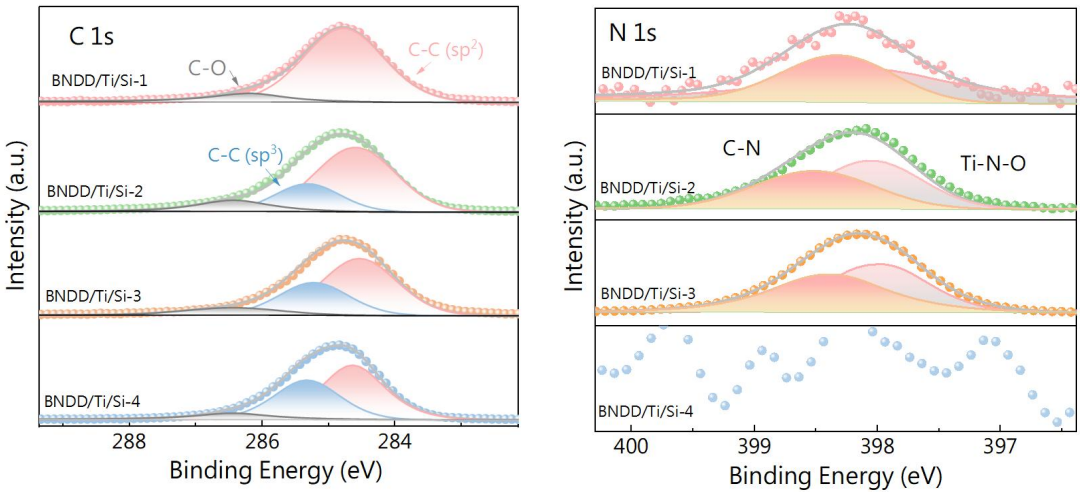


Figure 5.4 *XPS pattern of four BNDD samples with different diamond coverages on a Ti/Si substrate.*

To reveal the crystal structures of different BNDD/Ti/Si composite films, their XRD patterns were recorded and shown in **Figure 5.3.** The diffraction peak at 2θ = 69.1° originates from silicon (100). Two peaks at 2θ = 43.9° and 75.3° are indexed to the (111) and (220) planes of diamond, respectively. Other three peaks at

2θ = 48.1°, 54.6° and 75.3° are ascribed to the (200), (211) and (220) planes of TiO_2, respectively. The peak at 2θ = 61.5° corresponds the TiC or TiN formation.

The C 1s XPS spectra of these samples were collected with an aim to reveal the evolution of carbon chemical bonding on the surface of BNDD/Ti/Si samples. As shown in the XPS spectrum of BNDD/Ti/Si-2, a C-C (sp^3) peak appears at approximately 284.8 eV. Its peak area gradually increases from BNDD/Ti/Si-2 to BNDD/Ti/Si-4, indicating the progressive formation of diamond nanoparticles. Meanwhile, the C-C (sp^2) peak at 284.1 eV and the C–O peak at 286.3 eV demonstrate the contributions of graphitic carbon and oxidized carbon structures in these samples. This variation highlights the transition from sp^2 to sp^3 bonding, providing strong evidence about the formation of diamond nanoparticles.

Meanwhile, the relevant N 1s XPS spectrum of these samples exhibit two main peaks, attributed to C-N bonds and Ti-N-O bonds. In the XPS spectra of BNDD/Ti/Si-1, BNDD/Ti/Si-2, and BNDD/Ti/Si-3 samples, these peaks are also clearly visible, indicating the presence of nitrogen bonded to carbon and titanium oxide on the surface. However, in the XPS spectrum of the BNDD/Ti/Si-4 sample, the intensity of these signals decreases significantly. This is because as the diamond coverage increases, the Ti-N-O and related surface species are effectively shielded by the diamond layer, or their exposure is much reduced. This demonstrates that the diamond deposition significantly alters the surface chemical environment by masking the underlying Ti layer and its associated components.

To investigate the electrochemical activity of these four BNDD films grown on a Ti/Si substrate, their CVs and EIS plots were recorded in 0.1 M Na_2SO_4 aqueous solution containing 1 mM $[Fe(CN)_6]^{3-/4-}$. In the CVs of four samples (**Figure 5.5 a**), a well-defined pair of redox peaks is observed. These peak currents were then utilised to compare the electrochemical performance of these BNDD/Ti/Si films. When there is no diamond coverage (BNDD/Ti/Si), almost no electrochemical redox activity is found. As the BNDD coverage increases, the electrochemical activity is gradually

improved and the best performance (namely the highest peak currents) is seen until the surface is completely covered, demonstrates that the different diamond coverage has a noticeable impact on the electrochemical performance of the BNDD films.

The relationship between the reduction peak currents and the square root of the scan rates for various electrodes was further studied in the $[Fe(CN)_6]^{3-/4-}$ solution within the scan rate range of 10 to 50 mV s^{-1}. As shown in **Figure 5.5b**, the reduction peak current (I_p) is proportional to the square root of the scan rate (v), confirming the presence of a diffusion-controlled process at all electrodes in the $[Fe(CN)_6]^{3-/4-}$ solution. The Randles-Sevčik equation was then used to calculate the effective electrochemical active surface area of the electrodes.

$$I_p = (2.69\times10^5)\, n^{3/2} A D^{1/2} c v^{1/2} \quad (3\text{-}1)$$

where I_p is the peak current, n is the number of electrons transferred v is the scan rate ($V\cdot s^{-1}$), A is the electrode active surface area (cm^2), c is the concentration (mol cm^{-3}), D is the diffusion coefficient (6.7×10^{-6} $cm^2\cdot s^{-1}$). The calculated effective electrochemical active surface areas were 0.008, 0.025, 0.032, and 0.036 cm^2 for four electrodes, with the BNDD/Ti/Si-4 showing the largest active surface area.

The Nyquist plots of four electrodes were recorded in 0.5 M KCl aqueous solution containing 1 mM $[Fe(CN)_6]^{3-/4-}$ (**Figure 5.5c**). It is known that in the EIS spectra the diameter of a semicircle in the high-frequency region directly reflects the charge transfer resistance (R_{ct}) at the electrode/electrolyte interface. A bigger diameter indicates a higher resistance or a slower electron transfer rate, and vice versa. To obtain such R_{ct} values, these plots were fitted using a Randles equivalent circuit, yielding the R_{ct} values of 119 kΩ, 6.3 kΩ, 3.5 kΩ and 0.5 kΩ for BNDD/Ti/Si-1, BNDD/Ti/Si-2, BNDD/Ti/Si-3, and BNDD/Ti/Si-4, respectively. This confirms that the BNDD/Ti/Si-4 has the smallest resistance and the fastest electron transfer rate among four studied composites.

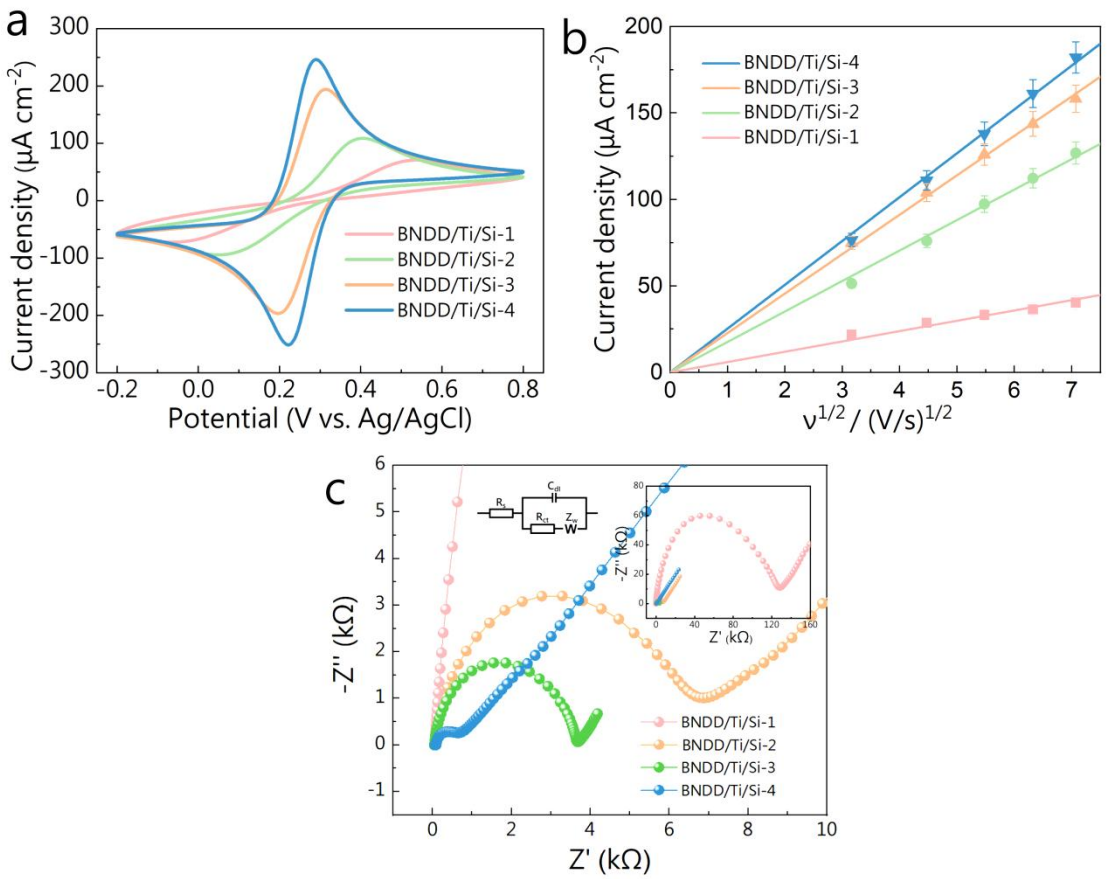


Figure 5.5 *(a) CVs of 1 mM $K_3[Fe(CN)_6]$ in 0.5 M KCl on four BNDD films at a scan rate of 100 mV s^{-1}. (b) The variation of cathodic peak currents with square root of scan rates on these films. (c) Nyquist plots of 1 mM $[Fe(CN)_6]^{3-/4-}$ in 0.5 M KCl on the BNDD films and the fitting of the equivalent circuit (inset). The terms of R_s, R_{ct}, Z_w, and C_{dl} stand for solution resistance, charge transfer resistance, warburg impedance (diffusion), double-layer capacitance, respectively.*

The photoelectrochemical response of four BNDD films grown on a Ti/Si substrate were then assessed in 0.5 M Na_2SO_4 solution under irradiation. All four electrodes exhibit prompt and reproducible photocurrent responses upon each illumination, implying the fast charge transport process in the integrated photoanodes. More importantly, their photoelectrochemical response or their photocurrent density varies with diamond coverage of these electrodes. From the tests about the variation in photocurrent density over time under light on/off cycles **(Figure 5.6a)**, one can see

that the BNDD/Ti/Si-1 (without diamond coverage) exhibits the lowest photocurrent density, due to the presence of oxide, nitride, and carbide species in the Ti layer and probably also its poor conductivity and electrochemical activity. As the diamond coverage increases (BNDD/Ti/Si-2 and BNDD/Ti/Si-3), or when BNDD partially covers these low-activity oxide species and introduces a highly conductive and chemically stable interface, the photocurrent density of BNDD/Ti/Si-2 and BNDD/Ti/Si-3 improves progressively. It is believed that the synergistic effect between the partially oxidized species in the Ti layer and BNDD plays a key role in enhancing electrode performance, while the high diamond coverage ensures stability and further improvement in photoelectrochemical performance. This synergy is a critical factor driving the highest performance enhancement for the BNDD/Ti/Si-3 electrodes.

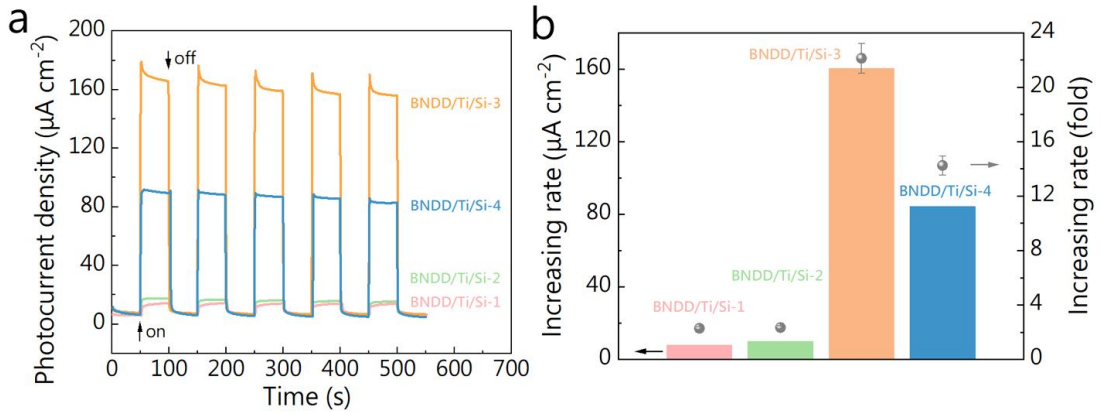


Figure 5.6 *(a) The photocurrent density versus time curves for four BNDD/Ti/Si electrodes (BNDD/Ti/Si-1 to BNDD/Ti/Si-4) with/without light illumination; (b) Comparison of increasing rates of their photocurrent density and fold enhancements for the corresponding electrodes.*

In the case of BNDD/Ti/Si-4 where the surface is fully covered with a diamond layer, its photocurrent density is slightly lower than that of BNDD/Ti/Si-3. This is because for the BNDD/Ti/Si-3 electrode the oxidized species on the Ti surface are almost entirely covered, and the highly conductive and chemically stable diamond layer dominates the electrode's photoelectrochemical behavior, significantly

increasing the photocurrent density. However, for BNDD/Ti/Si-4 electrode, the excessive diamond coverage suppresses the synergistic effect between the oxidized species and the doped diamond, leading to its slight decrease in performance compared to the BNDD/Ti/Si-3 electrode. More precisely, its photocurrent density reaches approximately 170 μA cm^{-2}, with an enhancement factor of up to 22 times.

The increase rates of related photocurrent densities (left y-axis) and fold enhancements (right y-axis) of these four electrodes were further compared **(Figure 5.6b)**. The BNDD/Ti/Si-3 electrode achieves the highest photocurrent density and the most significant performance improvement. Again, this is because as the diamond coverage increases the photoelectrochemical performance of the BNDD/Ti/Si electrode improves progressively, reaching its optimal performance near complete coverage.

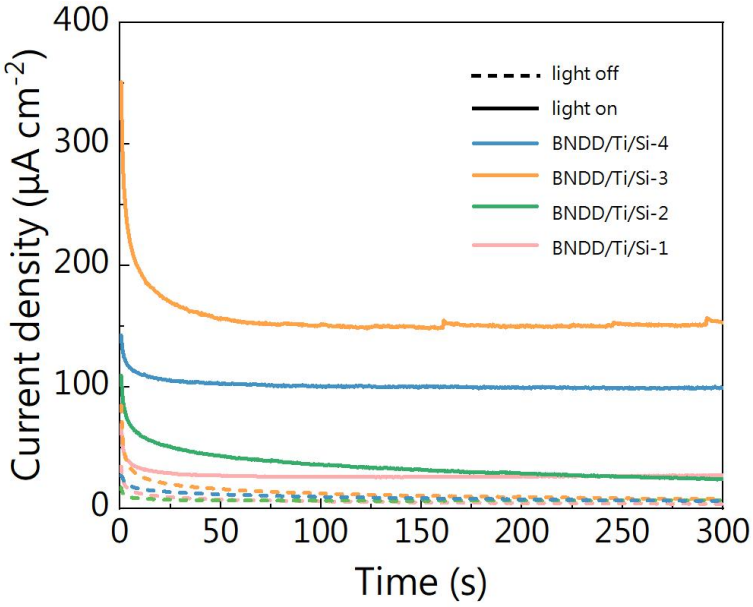


Figure 5.7 *Electrochemical and photoelectrochemical performances of four BNDD/Ti/Si electrodes with/without light illumination.*

The variation in current density over time for four BNDD/Ti/Si electrodes was examined with/without light illumination in a 0.5 M Na_2SO_4 solution when a bias of 1.5 V was applied (**Figure 5.7**). The dashed lines represent the electrochemical performance, while the solid lines refer to the photoelectrochemical performance. The

BNDD/Ti/Si-3 demonstrates the best photoelectrochemical performance, which is attributed to the synergistic effect between the oxidized species in the Ti layer and the diamond under partial coverage conditions, as discussed previously. This synergy significantly improves the interfacial conductivity and electrochemical stability. When the light is turned off, the current density of all electrodes decreases rapidly, indicating the dependence of the photocurrent on light. Additionally, as the diamond coverage increases, the dark current density slightly improves, perhaps due to enhanced interfacial conductivity. In summary, the BNDD/Ti/Si-3 electrode achieves the best photoelectrochemical performance under a bias voltage of 1.5 V in a 0.5 M Na_2SO_4 electrolyte.

5.2 Photo-electrcatalytic methyl orange oxidation of BNDD/Ti/Si

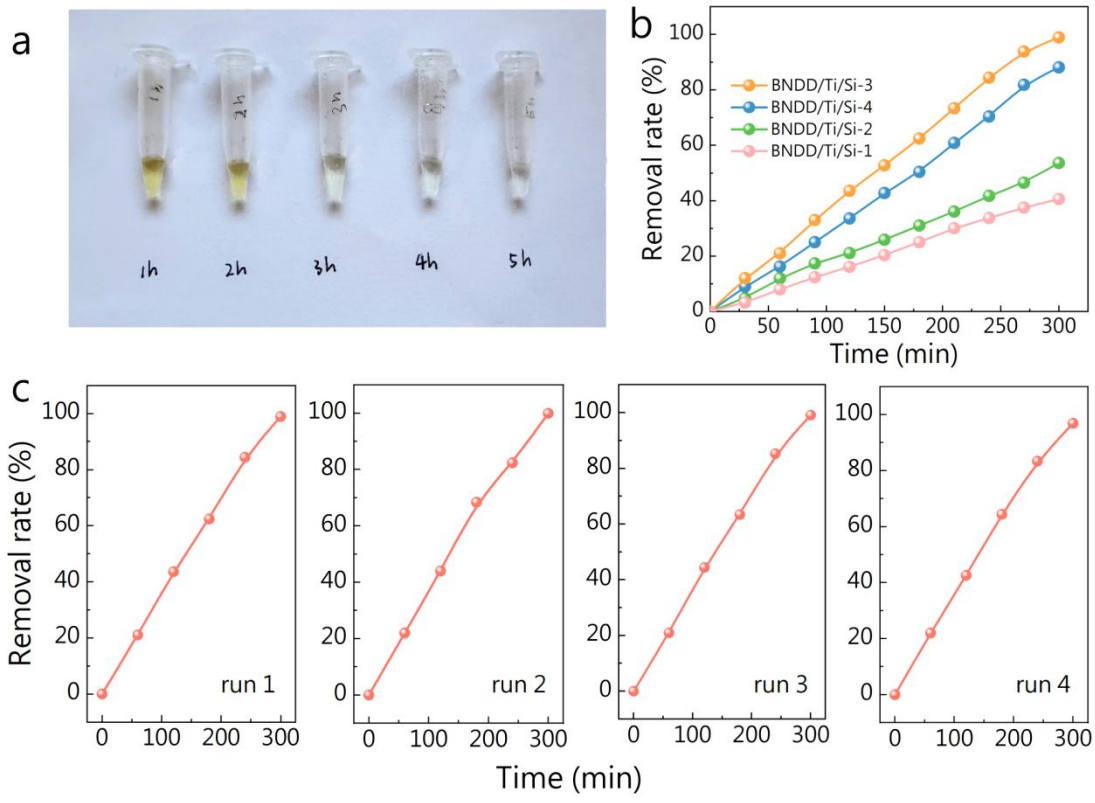


Figure 5.8 *PEC catalytic performance of BNDD/Ti/Si electrodes with different diamond coverage levels: (a) photographs of MO solutions at different PEC degradation times, (b) MO removal rates of different BNDD/Ti/Si electrodes, (c) four repeated MO degradations.*

Photoelectrocatalytic (PEC) degradation of dye molecules (here MO) was first investigated using a BNDD/Ti/Si electrode - as a representative example. **Figure 5.8(a)** shows photographs of MO solutions at different PEC degradation times, where the color transition of these solution: from orange to colorless indicates the reaction progress, namely the MO degradation. More specifically, the BNDD/Ti/Si-3 electrode, as a photoelectrocatalyst can degrade 200 mg/L MO within 5 hours. **Figure 5.8(b)** presents the variation of MO removal rates over time using the BNDD/Ti/Si electrodes with different diamond coverages (BNDD/Ti/Si-1, 2, 3, and 4 having diamond coverage of 0%, partial coverage, extensive coverage, and full coverage with pin-hole free, respectively). Among them, BNDD/Ti/Si-3 achieves the highest MO removal rate, reaching 100% within 300 min, while the other electrodes exhibit slower degradation rates, highlighting the importance of optimized diamond coverage for enhanced PEC efficiency. **Figure 5.8(c)** displays the results of four repeated experiments (runs 1 to 4) using the BNDD/Ti/Si-3 electrode. Consistent degradation trends in MO removal rates are found, or complete MO degradation within the same timeframe, confirming excellent stability and reusability of the BNDD/Ti/Si-3 photoelectrode.

5.3 Coupling of anodic methyl orange oxidation and cathodic NO_3RR

The NO_3RR was then coupled with photoelecatalytic MO oxidation, namely to assemble Cu_2O@CNF-BNDD featuring the highest efficiency for NO_3RR catalyst with BNDD/Ti/Si-3 showing the highest activity for the MO into a H-type electrolyzer (**Figure 5.9a**).

The LSVs (**Figure 5.9b)** compare the performance of different cells when the OER/HER, OER/NO_3RR, and MO/NO_3RR are considered. As expected, The OER/HER cell requires the highest applied potential at a cell voltage of 4.123 V to reach 10 mA cm^{-2}. When the anodic MO oxidation using BNDD/Ti/Si-3 is coupled

with cathodic NO_3RR using Cu_2O@CNF-BNDD, a low cell voltage of 3.768 is required to achieve a current density of 10 mA cm^{-2}. It is 194 mV lower than that of OER/NO_3RR, significantly reducing the required input potential, due to the faster kinetic reaction rates of MO and NO_3^-RR compared to the OER and HER, respectively.

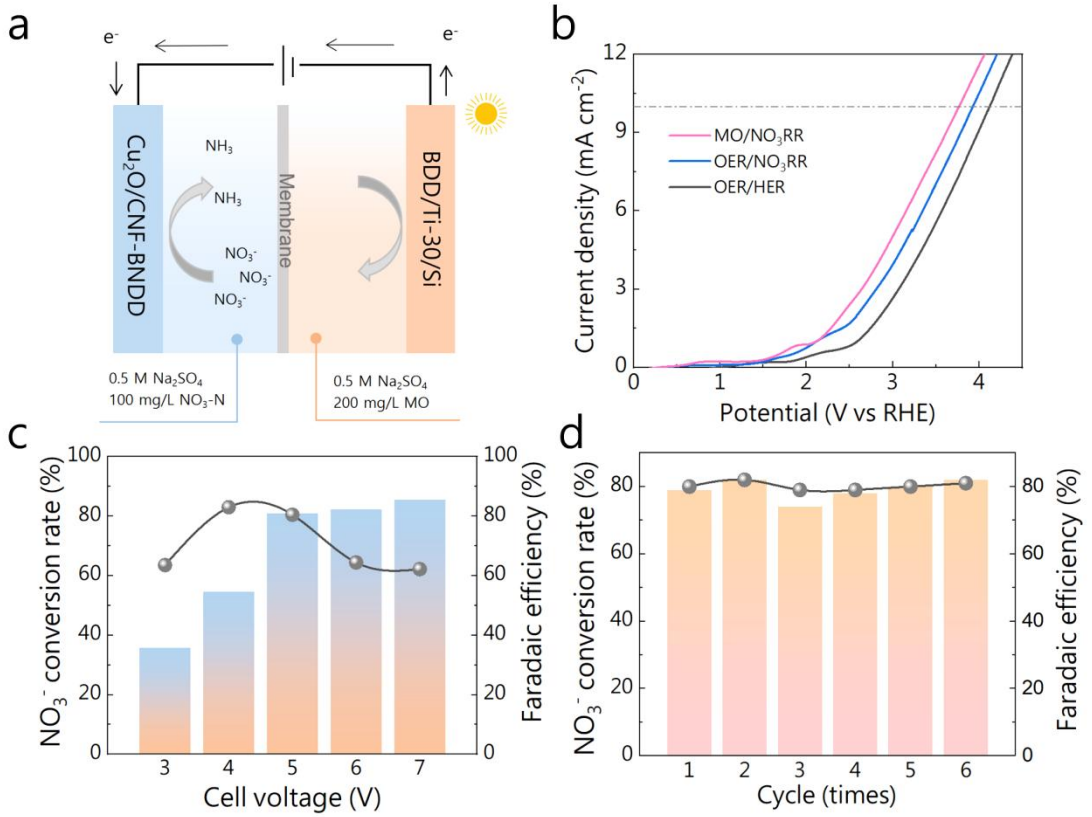


Figure 5.9 *(a) Schematic illustration for the two-electrode cell including anodic MO/BNDD/Ti/Si-3 oxidation and cathodic NO_3RR/Cu_2O@CNF-BNDD reduction. (b) LSVs of a two-electrode electrolyzer in 0.5 M Na_2SO_4 (0.5 M MO) and the catholyte including 0.5 M Na_2SO_4 (100 mg L^{-1} NO_3-N). (c) NO_3 conversion rates and FEs for this integrated cell at various potentials for 2 h. (d) The cycling tests at 5 V for 2 h.*

Because of the significantly lower potential for the MO in comparison with the OER, excellent NO_3RR performance was realized on the Cu_2O@CNF-BNDD surface, displaying 85.47% NO_3^- conversion rate and a FE of 82.96% at the cell voltage of 5.0 V (**Figure 5.9c**). The stability of this catalyst was tested (**Figure 5.9d**), where the

NO_3^- conversion rates and FEs were estimated over 6 cycles. The NO_3^- conversion rate remains consistently high (around 78-82%), while the FE stays close to 80%. These results highlight the catalyst's outstanding durability and stable performance, making it highly suitable for practical applications.

5.4 Conclusions

This study proposes an innovative and efficient electrochemical strategy that combines photoelectrocatalytic methyl orange (MO) oxidation with nitrate reduction reaction (NO_3RR). By replacing the traditional oxygen evolution reaction (OER) with MO oxidation, the system achieves a cell voltage of only 3.768 V at a current density of 10 mA cm^{-2}, which is 194 mV lower than OER/NO_3RR, thereby substantially reducing energy consumption. The system integrates dual functionalities of waste treatment and resource recovery, effectively degrading organic pollutants (MO) while converting nitrate into high-value ammonia (NH_3), achieving a synergy of pollution control and resource utilization. This integrated system, with its highly efficient electron transport pathways, minimizes byproduct formation and energy loss, offering a multifunctional solution for pollution remediation and resource recovery. Future research will focus on further optimizing electrode materials and expanding the system's adaptability to other pollutants, paving the way for practical applications in sustainable pollution control and resource utilization.

Chapter 6. Summary and outlook

6.1 Summary

This thesis systematically investigates boron and nitrogen co-doped diamond (BNDD) films grown on the metal layers, focusing on their design, synthesis, characterization, and applications in electrochemical processes. Advanced deposition techniques such as magnetron sputtering, electrodeposition, and microwave plasma chemical vapor deposition (MPCVD) were employed to ensure uniform doping and interface optimization, maximizing the performance of BNDD materials. Combining experimental methods and density functional theory (DFT) simulations, the study demonstrates that metal interlayer between diamond and Si substrate exhibit significant advantages in electron transfer rates, active site optimization, and stability, laying a solid foundation for developing next-generation efficient electrochemical materials.

The research explores various BNDD-based electrode systems, including BNDD/Metal/Si, BNDD/Ti/Si, BNDD/Ta/Ti/Si, and Cu_2O@CNF-BNDD, to optimize their electrochemical performance. Experiments revealed that the introduction of interlayers such as Ti and Ta played a crucial role in reducing resistance, enhancing charge transport, and facilitating the formation of conductive TaC phases. Additionally, the B-N co-doping effect further enhanced the electrochemical performance by optimizing the electronic structure, increasing the charge carrier density, and promoting more efficient electron transfer at the electrode interface, further boosting the superior performance of BNDD/Ta/Ti/Si films. For example, BNDD/Ta/Ti/Si electrodes exhibited excellent performance in redox reactions and were successfully applied to supercapacitors. In a 0.05 M $[Fe(CN)_6]^{3-/4-}$ + 1.0 M Na_2SO_4 aqueous solution, the fabricated supercabattery achieved a capacitance of 95.25 $mF \cdot cm^{-2}$ at a scan rate of 10 $mV \cdot s^{-1}$ and demonstrated stability over 10,000 charge/discharge cycles. These findings highlight the critical role of interlayer design

in optimizing the properties of co-doped diamond materials and reveal that the intrinsic activity, reaction kinetics, and electrochemical applications of diamond films are highly dependent on the substrate used during diamond growth.

Furthermore, surface functionalization expanded the application potential of BNDD films. A Cu_2O@CNF-BNDD composite was developed by integrating carbon nanofibers (CNF) and Cu_2O onto the BNDD surface, significantly enhancing its efficiency in the electrochemical nitrate reduction reaction (NO_3RR). The composite delivered a high ammonia yield of 1056 $\mu g \cdot h^{-1} \cdot cm^{-2}$ with an impressive Faradaic efficiency of 92.6%. During prolonged NO_3RR, Cu_2O was observed to transform into Cu nanoparticles after 30 hours of reaction, as confirmed by post-reaction characterization. Leveraging these properties, the composite was incorporated into a Zn-NO_3^- battery system, demonstrating both efficient energy conversion and NH_3 production with a maximum power density of 2.7 $mW \cdot cm^{-2}$, exemplifying its potential for practical applications.

To address the sluggish kinetics of NO_3RR, an integrated photo-electrocatalytic system was developed. BNDD/Ti/Si electrodes served as photo-anodes for degrading methyl orange (MO), providing electrons for the cathodic reduction of nitrate to ammonia using Cu_2O@CNF-BNDD electrodes. This system achieved an 85.47% NO_3^- conversion rate and a Faradaic efficiency of 82.96% at a cell voltage of 5.0 V. Stability tests over six cycles revealed consistently high NO_3^- conversion rates (around 78-82%) and Faradaic efficiencies near 80%, demonstrating the robustness of the system. This "three birds with one stone" strategy integrated dye degradation, nitrate reduction, and valuable chemical synthesis into a single system, significantly improving efficiency and functionality.

In conclusion, this thesis demonstrates the vast potential of co-doped diamond films in diverse electrochemical applications, including energy storage, pollutant degradation, and sustainable chemical production. The findings provide critical

insights into the design of advanced co-doped diamond materials and establish a strong foundation for future innovations in energy and environmental technologies.

6.2 Outlook

Although this research achieved significant progress in the electrochemical applications of BNDD composites, there remain numerous directions for future exploration. Firstly, optimizing growth conditions to achieve precise control over morphology, grain size, and doping distribution will be crucial for enhancing material performance. Additionally, precise control over catalyst crystal planes could further optimize BNDD composite selectivity toward intermediate adsorption, thus boosting catalytic efficiency and stability. For instance, refining growth control techniques to accurately regulate the size of carbon nanofibers and the crystal plane structure of catalysts could further enhance electrocatalytic activity and stability.

Beyond innovative synthesis methods, characterization of DCs, especially their atomic-phase structure, requires advanced in situ and ex situ techniques, such as in situ electrochemical Raman, infrared, and impedance spectroscopy. These techniques are essential for a deeper understanding of interactions between the diamond phase and incorporated components, including potential chemical bond formations.

Based on the ammonia synthesis results in Chapter 4.2, adding a secondary reactant holds promise for synthesizing higher-value products, such as urea. The design of a flow reactor with product collection could further extend the practical applications of diamond-based composites in small-molecule electrocatalysis.

References

(1) Bundy, F. P.; Hall, H. T.; Strong, H. M.; Wentorfjun., R. H. Man-Made Diamonds. *Nature* **1955**, *176* (4471), 51–55.

(2) Matsumoto, S.; Sato, Y.; Tsutsumi, M.; Setaka, N. Growth of Diamond Particles from Methane-Hydrogen Gas. *J. Mater. Sci.* **1982**, *17* (11), 3106–3112.

(3) Gracio, J. J.; Fan, Q. H.; Madaleno, J. C. Diamond Growth by Chemical Vapour Deposition. *J. Phys. Appl. Phys.* **2010**, *43* (37), 374017.

(4) Angus, J. C. Diamond Synthesis by Chemical Vapor Deposition: The Early Years. *Diam. Relat. Mater.* **2014**, *49*, 77–86.

(5) Stachel, T.; Luth, R. W. Diamond Formation — Where, When and How? *Lithos* **2015**, *220–223*, 200–220.

(6) Yang, N.; Foord, J. S.; Jiang, X. Diamond Electrochemistry at the Nanoscale: A Review. *Carbon* **2016**, *99*, 90–110.

(7) Pleskov, Yu. V. Electrochemistry of Diamond: A Review. *Russ. J. Electrochem.* **2002**, *38* (12), 1275–1291.

(8) Yu, S.; Yang, N.; Zhuang, H.; Meyer, J.; Mandal, S.; Williams, O. A.; Lilge, I.; Schönherr, H.; Jiang, X. Electrochemical Supercapacitors from Diamond. *J. Phys. Chem. C* **2015**, *119* (33), 18918–18926.

(9) Yu, S.; Yang, N.; Vogel, M.; Mandal, S.; Williams, O. A.; Jiang, S.; Schönherr, H.; Yang, B.; Jiang, X. Battery-like Supercapacitors from Vertically Aligned Carbon Nanofiber Coated Diamond: Design and Demonstrator. *Adv. Energy Mater.* **2018**, *8* (12), 1702947.

(10) Rao, T. N.; Fujishima, A. Recent Advances in Electrochemistry of Diamond. *Diam. Relat. Mater.* **2000**, *9* (3–6), 384–389.

(11) Härtl, A.; Schmich, E.; Garrido, J. A.; Hernando, J.; Catharino, S. C. R.; Walter, S.; Feulner, P.; Kromka, A.; Steinmüller, D.; Stutzmann, M. Protein-Modified Nanocrystalline Diamond Thin Films for Biosensor Applications. *Nat. Mater.* **2004**, *3* (10), 736–742.

(12) Carabelli, V.; Gosso, S.; Marcantoni, A.; Xu, Y.; Colombo, E.; Gao, Z.; Vittone, E.; Kohn, E.; Pasquarelli, A.; Carbone, E. Nanocrystalline Diamond Microelectrode Arrays Fabricated on Sapphire Technology for High-Time Resolution of Quantal Catecholamine Secretion from Chromaffin Cells. *Biosens. Bioelectron.* **2010**, *26* (1), 92–98.

(13) Yu, S.; Xu, J.; Kato, H.; Yang, N.; Schulte, A.; Schönherr, H.; Jiang, X. Phosphorus-doped Nanocrystalline Diamond for Supercapacitor Application. *ChemElectroChem* **2019**, *6* (4), 1088–1093.

(14) Yu, S.; Sankaran, K. J.; Korneychuk, S.; Verbeeck, J.; Haenen, K.; Jiang, X.; Yang, N. High-Performance Supercabatteries Using Graphite@diamond Nano-Needle Capacitor Electrodes and Redox Electrolytes. *Nanoscale* **2019**, *11* (38), 17939–17946.

(15) Marciano, F. R.; Almeida, E. C.; Bonetti, L. F.; Corat, E. J.; Trava-Airoldi, V. J. Improvement of Diamond-like Carbon Electrochemical Corrosion Resistance by Addition of Nanocrystalline Diamond. *J. Colloid Interface Sci.* **2010**, *342* (2), 636–637.

(16) Jiang, M.; Zhang, Z.; Chen, C.; Ma, W.; Han, S.; Li, X.; Lu, S.; Hu, X. High Efficient Oxygen Reduced Reaction Electrodes by Constructing Vertical Graphene Sheets on Separated Papillary Granules Formed Nanocrystalline Diamond Films. *Carbon* **2020**, *168*, 536–545.

(17) Zhai, Z.; Huang, N.; Jiang, X. Progress in Electrochemistry of Hybrid Diamond/Sp^2-C Nanostructures. *Curr. Opin. Electrochem.* **2022**, *32*, 100884.

(18) Hu, X. J.; Li, R. B.; Shen, H. S.; Dai, Y. B.; He, X. C. Electrical and Structural Properties of Boron and Phosphorus Co-Doped Diamond Films. *Carbon* **2004**, *42* (8–9), 1501–1506.

(19) Sultana, M.; Karmakar, S.; Haque, A. N- and p-Type Doping of Diamonds: A Review. *Mater. Sci. Semicond. Process.* **2025**, *186*, 109024.

(20) Lloret, F.; Sankaran, K. J.; Millan-Barba, J.; Desta, D.; Rouzbahani, R.; Pobedinskas, P.; Gutierrez, M.; Boyen, H.-G.; Haenen, K. Improved Field Electron

Emission Properties of Phosphorus and Nitrogen Co-Doped Nanocrystalline Diamond Films. *Nanomaterials* **2020**, *10* (6), 1024.

(21) Liu, Y.; Chen, S.; Quan, X.; Yu, H.; Zhao, H.; Zhang, Y.; Chen, G. Boron and Nitrogen Codoped Nanodiamond as an Efficient Metal-Free Catalyst for Oxygen Reduction Reaction. *J. Phys. Chem. C* **2013**, *117* (29), 14992–14998.

(22) Wen, R.; Jiang, Z.; Miao, R.; Wang, L.; Liang, Y.; Deng, J.; Shao, Q.; Zhang, J. Electronic Transport Properties of B/N/P Co-Doped Armchair Graphene Nanoribbon Field Effect Transistor. *Diam. Relat. Mater.* **2022**, *124*, 108893.

(23) Guo, T.; Yang, N.; Yang, B.; Schulte, A.; Jin, Q.; Koch, U.; Mandal, S.; Engelhard, C.; Williams, O. A.; Schönherr, H.; Jiang, X. Electrochemistry of Nitrogen and Boron Bi-Element Incorporated Diamond Films. *Carbon* **2021**, *178*, 19–25.

(24) Liu, Y.; Zhang, Y.; Cheng, K.; Quan, X.; Fan, X.; Su, Y.; Chen, S.; Zhao, H.; Zhang, Y.; Yu, H.; Hoffmann, M. R. Selective Electrochemical Reduction of Carbon Dioxide to Ethanol on a Boron- and Nitrogen-co-doped Nanodiamond. *Angew. Chem.* **2017**, *129* (49), 15813–15817.

(25) Liu, Y.; Chen, S.; Quan, X.; Zhao, H.; Yu, H.; Zhang, Y. Tuning the Electrochemical Properties of a Boron and Nitrogen Codoped Nanodiamond Rod Array to Achieve High Performance for Both Electro-Oxidation and Electro-Reduction. *J. Mater. Chem. A* **2013**, *1* (46), 14706.

(26) Li, J.; Wang, Q.; Liu, Y.; Jiang, Z.; Liu, J.; Li, H.; Yuan, X. Boron/Nitrogen Co-Doped Diamond Electrode for Highly Efficient Electrochemistry Detection of Aniline. *Funct. Diam.* **2021**, *1* (1), 135–142.

(27) Schaper-Rinkel, P. The Role of Future-Oriented Technology Analysis in the Governance of Emerging Technologies: The Example of Nanotechnology. *Technol. Forecast. Soc. Change* **2013**, *80* (3), 444–452.

(28) Zhang, C.; Wang, X.; Liang, Q.; Liu, X.; Weng, Q.; Liu, J.; Yang, Y.; Dai, Z.; Ding, K.; Bando, Y.; Tang, J.; Golberg, D. Amorphous Phosphorus/Nitrogen-Doped Graphene Paper for Ultrastable Sodium-Ion Batteries. *Nano Lett.* **2016**, *16* (3),

2054–2060.

(29) Zhao, Y.; Yang, N.; Yao, H.; Liu, D.; Song, L.; Zhu, J.; Li, S.; Gu, L.; Lin, K.; Wang, D. Stereodefined Codoping of Sp-n and s Atoms in Few-Layer Graphdiyne for Oxygen Evolution Reaction. *J. Am. Chem. Soc.* **2019**, *141* (18), 7240–7244.

(30) Tang, H.; Yuan, X.; Cheng, Y.; Fei, H.; Liu, F.; Liang, T.; Zeng, Z.; Ishii, T.; Wang, M.-S.; Katsura, T.; Sheng, H.; Gou, H. Synthesis of Paracrystalline Diamond. *Nature* **2021**, *599* (7886), 605–610.

(31) Duo, I.; Fujishima, A.; Comninellis, C. Electron Transfer Kinetics on Composite Diamond (Sp^3)–Graphite (Sp^2) Electrodes. *Electrochem. Commun.* **2003**, *5* (8), 695–700.

(32) Jian, Z.; Xu, J.; Yang, N.; Han, S.; Jiang, X. A Perspective on Diamond Composites and Their Electrochemical Applications. *Curr. Opin. Electrochem.* **2021**, *30*, 100835.

(33) Yang, N.; Yu, S.; Macpherson, J. V.; Einaga, Y.; Zhao, H.; Zhao, G.; Swain, G. M.; Jiang, X. Conductive Diamond: Synthesis, Properties, and Electrochemical Applications. *Chem. Soc. Rev.* **2019**, *48* (1), 157–204.

(34) Mazaheri, H.; Allahkaram, S. R. Deposition, Characterization and Electrochemical Evaluation of Ni–P–Nano Diamond Composite Coatings. *Appl. Surf. Sci.* **2012**, *258* (10), 4574–4580.

(35) Jiang, X.; Klages, C.-P. Synthesis of Diamond/β-SiC Composite Films by Microwave Plasma Assisted Chemical Vapor Deposition. *Appl. Phys. Lett.* **1992**, *61* (14), 1629–1631.

(36) Zhuang, H.; Zhang, L.; Staedler, T.; Jiang, X. Highly Selective Diamond and β-SiC Crystal Formation at Increased Atomic Hydrogen Concentration: A Route for Synthesis of High-Quality and Patterned Hybrid Diamond/β-SiC Composite Film. *Scr. Mater.* **2011**, *65* (6), 548–551.

(37) Zhuang, H.; Zhang, L.; Staedler, T.; Jiang, X. Nanoscale Integration of SiC/SiO_2 Core-Shell Nanocables in Diamond through a Simultaneous Hybrid

Structure Fabrication. *Appl. Phys. Lett.* **2012**, *100* (19), 193102.

(38) Zhuang, H.; Jiang, X. Growth Controlling of Diamond and β-SiC Microcrystals in the Diamond/β-SiC Composite Films. *Surf. Coat. Technol.* **2014**, *249*, 84–89.

(39) Xu, J.; Yang, N.; Heuser, S.; Yu, S.; Schulte, A.; Schönherr, H.; Jiang, X. Achieving Ultrahigh Energy Densities of Supercapacitors with Porous Titanium Carbide/Boron-doped Diamond Composite Electrodes. *Adv. Energy Mater.* **2019**, *9* (17), 1803623.

(40) Chen, X.; Dong, X.; Zhang, C.; Zhu, M.; Ahmed, E.; Krishnamurthy, G.; Rouzbahani, R.; Pobedinskas, P.; Gauquelin, N.; Jannis, D.; Kaur, K.; Hafez, A. M. E.; Thiel, F.; Bornemann, R.; Engelhard, C.; Schönherr, H.; Verbeeck, J.; Haenen, K.; Jiang, X.; Yang, N. Interlayer Affected Diamond Electrochemistry. *Small Methods* **2024**, *2024*, 2301774.

(41) Zhai, Z.; Leng, B.; Yang, N.; Yang, B.; Liu, L.; Huang, N.; Jiang, X. Rational Construction of 3D-networked Carbon Nanowalls/Diamond Supporting CuO Architecture for High-performance Electrochemical Biosensors. *Small* **2019**, *15* (48), 1901527.

(42) Jian, Z.; Yang, N.; Vogel, M.; Zhou, Z.; Zhao, G.; Kienitz, P.; Schulte, A.; Schönherr, H.; Jiao, T.; Zhang, W.; Jiang, X. Tunable Photo-electrochemistry of Patterned TiO_2/BDD Heterojunctions. *Small Methods* **2020**, *4* (9), 2000257.

(43) Deshmukh, S.; Kunuku, S.; Jakobczyk, P.; Olejnik, A.; Chen, C.; Niu, H.; Yang, B.; Yang, N.; Bogdanowicz, R. Diamond-based Supercapacitors with Ultrahigh Cyclic Stability through Dual-phase MnO_2-graphitic Transformation Induced by High-dose Mn-ion Implantation. *Adv. Funct. Mater.* **2024**, *34* (8), 2308617.

(44) Zhang, C.; Huang, N.; Zhai, Z.; Liu, L.; Chen, B.; Yang, B.; Jiang, X.; Yang, N. Bifunctional Oxygen Electrocatalyst of Co_4N and Nitrogen-doped Carbon Nanowalls/Diamond for High-performance Flexible Zinc–Air Batteries. *Adv. Energy Mater.* **2023**, *13* (41), 2301749.

(45) Chen, B.; Zhai, Z.; Huang, N.; Zhang, C.; Yu, S.; Liu, L.; Yang, B.; Jiang, X.;

Yang, N. Highly Localized Charges of Confined Electrical Double-layers inside 0.7-nm Layered Channels. *Adv. Energy Mater.* **2023**, *13* (36), 2300716.

(46) Zhai, Z.; Zhang, C.; Chen, B.; Xiong, Y.; Liang, Y.; Liu, L.; Yang, B.; Yang, N.; Jiang, X.; Huang, N. Covalently-bonded Diaphite Nanoplatelet with Engineered Electronic Properties of Diamond. *Adv. Funct. Mater.* **2024**, *2024*, 2401949.

(47) Liu, J. H.; Pei, Z. L.; Shi, W. B.; Liu, Y. D.; Gong, J.; Sun, C. Studies on Preparation, Microstructure, Mechanical Properties and Corrosion Resistance of Ni Mo/Micron-Sized Diamond Composite Coatings. *Surf. Coat. Technol.* **2020**, *385*, 125451.

(48) Mochalin, V. N.; Gogotsi, Y. Nanodiamond–Polymer Composites. *Diam. Relat. Mater.* **2015**, *58*, 161–171.

(49) *Novel Aspects of Diamond: From Growth to Applications*; Yang, N., Ed.; Topics in Applied Physics; Springer International Publishing: Cham, 2019; Vol. 121.

(50) Yang, N.; Yu, S.; Zhang, W.; Cheng, H.; Simon, P.; Jiang, X. Electrochemical Capacitors with Confined Redox Electrolytes and Porous Electrodes. *Adv. Mater.* **2022**, *34* (34), 2202380.

(51) Zeng, Z.; Wen, J.; Lou, H.; Zhang, X.; Yang, L.; Tan, L.; Cheng, B.; Zuo, X.; Yang, W.; Mao, W. L.; Mao, H.; Zeng, Q. Preservation of High-Pressure Volatiles in Nanostructured Diamond Capsules. *Nature* **2022**, *608* (7923), 513–517.

(52) Tian, Q.; Yang, B.; Zhuang, H.; Guo, Y.; Wang, C.; Zhai, Z.; Liu, L.; Huang, N.; Jiang, X. Hybrid Diamond/Graphite Films: Morphological Evolution, Microstructure and Tribological Properties. *Diam. Relat. Mater.* **2016**, *70*, 179–185.

(53) Zhai, Z.; Huang, N.; Yang, B.; Liu, L.; Li, H.; Chen, J.; Zhang, B.; Jiang, X. In Situ Construction of Hierarchical Diamond Supported on Carbon Nanowalls/Diamond for Enhanced Electron Field Emission. *ACS Appl. Mater. Interfaces* **2020**, *12* (7), 8522–8532.

(54) Zhang, C.; Huang, N.; Zhai, Z.; Liu, L.; Chen, B.; Lu, Z.; Zhou, M.; Song, H.; Shi, D.; Yang, B.; Yang, N.; Jiang, X. Nitrogen-Doped Carbon Nanowalls/Diamond

Films as Efficient Electrocatalysts toward Oxygen Reduction Reaction. *Nanotechnology* **2022**, *33* (1), 15401.

(55) Srikanth Vadali, V. S. S.; Samra, H. A.; Staedler, T.; Jiang, X. Nanocrystalline Diamond/β-SiC Composite Interlayers for the Deposition of Continuous Diamond Films on W and Mo Substrate Materials. *Surf. Coat. Technol.* **2007**, *201* (22–23), 8981–8985.

(56) Tian, Q.; Huang, N.; Yang, B.; Zhuang, H.; Wang, C.; Zhai, Z.; Li, J.; Jia, X.; Liu, L.; Jiang, X. Diamond/β-SiC Film as Adhesion-Enhanced Interlayer for Top Diamond Coatings on Cemented Tungsten Carbide Substrate. *J. Mater. Sci. Technol.* **2017**, *33* (10), 1097–1106.

(57) Wang, T.; Handschuh-Wang, S.; Yang, Y.; Zhuang, H.; Schlemper, C.; Wesner, D.; Schönherr, H.; Zhang, W.; Jiang, X. Controlled Surface Chemistry of Diamond/β-SiC Composite Films for Preferential Protein Adsorption. *Langmuir* **2014**, *30* (4), 1089–1099.

(58) Wang, T.; Handschuh-Wang, S.; Huang, L.; Zhang, L.; Jiang, X.; Kong, T.; Zhang, W.; Lee, C.-S.; Zhou, X.; Tang, Y. Controlling Directional Liquid Motion on Micro- and Nanocrystalline Diamond/β-SiC Composite Gradient Films. *Langmuir* **2018**, *34* (4), 1419–1428.

(59) Yang, B.; Li, J.; Guo, L.; Huang, N.; Liu, L.; Zhai, Z.; Long, W.; Jiang, X. Fabrication of Silicon-Vacancy Color Centers in Diamond Films: Tetramethylsilane as a New Dopant Source. *CrystEngComm* **2018**, *20* (8), 1158–1167.

(60) Xu, J.; Yang, N.; Heuser, S.; Yu, S.; Schulte, A.; Schönherr, H.; Jiang, X. Achieving Ultrahigh Energy Densities of Supercapacitors with Porous Titanium Carbide/Boron-doped Diamond Composite Electrodes. *Adv. Energy Mater.* **2019**, *9* (17), 1803623.

(61) Shpilevaya, I.; Smirnov, W.; Hirsz, S.; Yang, N.; Nebel, C. E.; Foord, J. S. Nanostructured Diamond Decorated with Pt Particles: Preparation and Electrochemistry. *RSC Adv* **2014**, *4* (2), 531–537.

(62) Yu, S.; Yang, N.; Jiang, X.; Zhang, W.; Liu, S. Conductive Diamond for Electrochemical Energy Applications. In *Nanocarbon Electrochemistry*; Yang, N., Zhao, G., Foord, J., Eds.; Wiley, 2020; pp 171–199.

(63) Panizza, M.; Cerisola, G. Application of Diamond Electrodes to Electrochemical Processes. *Electrochimica Acta* **2005**, *51* (2), 191–199.

(64) Jian, Z.; Heide, M.; Yang, N.; Engelhard, C.; Jiang, X. Diamond Fibers for Efficient Electrocatalytic Degradation of Environmental Pollutants. *Carbon* **2021**, *175*, 36–42.

(65) Guo, Y.; Huang, N.; Yang, B.; Wang, C.; Zhuang, H.; Tian, Q.; Zhai, Z.; Liu, L.; Jiang, X. Hybrid Diamond/Graphite Films as Electrodes for Anodic Stripping Voltammetry of Trace Ag^{+} and Cu^{2+}. *Sens. Actuators B Chem.* **2016**, *231*, 194–202.

(66) Zhai, Z.; Huang, N.; Zhuang, H.; Liu, L.; Yang, B.; Wang, C.; Gai, Z.; Guo, F.; Li, Z.; Jiang, X. A Diamond/Graphite Nanoplatelets Electrode for Anodic Stripping Voltammetric Trace Determination of Zn(II), Cd(II), Pb(II) and Cu(II). *Appl. Surf. Sci.* **2018**, *457*, 1192–1201.

(67) Kelly, P. J.; Arnell, R. D. Magnetron Sputtering: A Review of Recent Developments and Applications. *Vacuum* **2000**, *56* (3), 159–172.

(68) Gudmundsson, J. T.; Lundin, D. Introduction to Magnetron Sputtering. In *High Power Impulse Magnetron Sputtering*; Elsevier, 2020; pp 1–48.

(69) Liang, J.; Liu, Q.; Li, T.; Luo, Y.; Lu, S.; Shi, X.; Zhang, F.; Asiri, A. M.; Sun, X. Magnetron Sputtering Enabled Sustainable Synthesis of Nanomaterials for Energy Electrocatalysis. *Green Chem.* **2021**, *23* (8), 2834–2867.

(70) Kale, M. B.; Borse, R. A.; Gomaa Abdelkader Mohamed, A.; Wang, Y. Electrocatalysts by Electrodeposition: Recent Advances, Synthesis Methods, and Applications in Energy Conversion. *Adv. Funct. Mater.* **2021**, *31* (25), 2101313.

(71) Han, H.; Lee, C.; Kim, Y.; Lee, J.; Kim, R.; Kim, J.; Yoo, B. Cu to Cu Direct Bonding at Low Temperature with High Density Defect in Electrodeposited Cu. *Appl. Surf. Sci.* **2021**, *550*, 149337.

(72) Lee, S. A.; Yang, J. W.; Choi, S.; Jang, H. W. Nanoscale Electrodeposition: Dimension Control and 3D Conformality. *Exploration* **2021**, *1* (3), 20210012.

(73) Gong, Y.; Jia, W.; Zhou, B.; Zheng, K.; Ma, D.; Li, Z.; Gao, J.; Ma, Y.; Hei, H.; Yu, S.; Xue, Y.; Wu, Y. Effect of Boron Doping Levels on the Microstructure and Characteristics of High-Quality Boron-Doped Diamond Electrodes Prepared by MPCVD. *Diam. Relat. Mater.* **2023**, *139*, 110377.

(74) Shang, H.; Jiang, Y. Investigation on Growth Rate and Quality of Diamond Materials in MPCVD System. *Semicond. Sci. Technol.* **2024**, *39* (11), 115013.

(75) Verbeeck, J.; Van Aert, S. Model Based Quantification of EELS Spectra. *Ultramicroscopy* **2004**, *101* (2–4), 207–224.

(76) Van Den Broek, W.; Jannis, D.; Verbeeck, J. Convexity Constraints on Linear Background Models for Electron Energy-Loss Spectra. *Ultramicroscopy* **2023**, *254*, 113830.

(77) Annys, A.; Jannis, D.; Verbeeck, J. Deep Learning for Automated Materials Characterisation in Core-Loss Electron Energy Loss Spectroscopy. *Sci. Rep.* **2023**, *13* (1), 13724.

(78) Houam, S.; Affoune, A. M.; Atek, I.; Kesri, F.; Saad Guermeche, R.; Chelaghmia, M. L.; Nacef, M.; Khelifi, O.; Banks, C. E. Determination of the Standard Rate Constant for Soluble-Soluble Quasi-Reversible Electrochemical Systems by Linear Sweep Voltammetry: Application to the Electrochemical Oxidation on Screen-Printed Graphite Electrodes. *Electrochimica Acta* **2023**, *449*, 142200.

(79) Kissinger, P. T.; Heineman, W. R. Cyclic Voltammetry. *J. Chem. Educ.* **1983**, *60* (9), 702.

(80) McCreery, R. L. Advanced Carbon Electrode Materials for Molecular Electrochemistry. *Chem. Rev.* **2008**, *108* (7), 2646–2687.

(81) Magar, H. S.; Hassan, R. Y. A.; Mulchandani, A. Electrochemical Impedance Spectroscopy (EIS): Principles, Construction, and Biosensing Applications. *Sensors* **2021**, *21* (19), 6578.

(82) Mohd Abid, M. A. Azam; Radzi, M. I.; Mupit, M.; Osman, H.; Munawar, R. F.; Samat, K. F.; Mohd Suan, M. S.; Isomura, K.; Islam, M. R. Cyclic Voltammetry and Galvanostatic Charge-Discharge Analyses of Polyaniline/Graphene Oxide Nanocomposite Based Supercapacitor. *Malays. J. Compos. Sci. Manuf.* **2020**, *3* (1), 14–26.

(83) Rafiee, M.; Abrams, D. J.; Cardinale, L.; Goss, Z.; Romero-Arenas, A.; Stahl, S. S. Cyclic Voltammetry and Chronoamperometry: Mechanistic Tools for Organic Electrosynthesis. *Chem. Soc. Rev.* **2024**, *53* (2), 566–585.

(84) Lingane, P. J.; Peters, D. G. Chronopotentiometry. *Crit. Rev. Anal. Chem.* **1971**, *1* (4), 587–634.

(85) Sharma, D. K.; Girão, A. V.; Chapon, P.; Neto, M. A.; Oliveira, F. J.; Silva, R. F. Advances in RF Glow Discharge Optical Emission Spectrometry Characterization of Intrinsic and Boron-Doped Diamond Coatings. *ACS Appl. Mater. Interfaces* **2022**, *14* (5), 7405–7416.

(86) Wang, H.; Tzeng, Y.-K.; Ji, Y.; Li, Y.; Li, J.; Zheng, X.; Yang, A.; Liu, Y.; Gong, Y.; Cai, L.; Li, Y.; Zhang, X.; Chen, W.; Liu, B.; Lu, H.; Melosh, N. A.; Shen, Z.-X.; Chan, K.; Tan, T.; Chu, S.; Cui, Y. Synergistic Enhancement of Electrocatalytic CO_2 Reduction to C_2 Oxygenates at Nitrogen-Doped Nanodiamonds/Cu Interface. *Nat. Nanotechnol.* **2020**, *15* (2), 131–137.

(87) Zhang, J.; Yu, X.; Zhang, Z.-Q.; Zhao, Z.-Y. Preparation of Boron-Doped Diamond Foam Film for Supercapacitor Applications. *Appl. Surf. Sci.* **2020**, *506*, 144645.

(88) He, Y.; Huang, W.; Chen, R.; Zhang, W.; Lin, H. Improved Electrochemical Performance of Boron-Doped Diamond Electrode Depending on the Structure of Titanium Substrate. *J. Electroanal. Chem.* **2015**, *758*, 170–177.

(89) Jian, Z.; Yang, N.; Vogel, M.; Leith, S.; Schulte, A.; Schönherr, H.; Jiao, T.; Zhang, W.; Müller, J.; Butz, B.; Jiang, X. Flexible Diamond Fibers for High-energy-density Zinc-ion Supercapacitors. *Adv. Energy Mater.* **2020**, *10* (44),

2002202.

(90) Sun, L. T.; Gong, J. L.; Zhu, D. Z.; Zhu, Z. Y.; He, S. X. Diamond Nanorods from Carbon Nanotubes. *Adv. Mater.* **2004**, *16* (20), 1849–1853.

(91) Werner, M. Diamond Metallization for Device Applications. *Semicond. Sci. Technol.* **2003**, *18* (3), S41–S46.

(92) Zhang, J.; Yu, X.; Zhao, Z.; Zhang, Z.; Li, J. Influence of Pore Size of Ti Substrate on Structural and Capacitive Properties of Ti/Boron Doped Diamond Electrode. *J. Alloys Compd.* **2019**, *777*, 84–93.

(93) Liu, Z.; Li, H.; Li, M.; Li, C.; Qian, L.; Su, L.; Yang, B. Preparation of Polycrystalline BDD/Ta Electrodes for Electrochemical Oxidation of Organic Matter. *Electrochimica Acta* **2018**, *290*, 109–117.

(94) Moraleda, I.; Cotillas, S.; Llanos, J.; Sáez, C.; Cañizares, P.; Pupunat, L.; Rodrigo, M. A. Can the Substrate of the Diamond Anodes Influence on the Performance of the Electrosynthesis of Oxidants? *J. Electroanal. Chem.* **2019**, *850*, 113416.

(95) Zhang, C.; Lu, X.; Lu, Y.; Ding, M.; Tang, W. Titanium-boron Doped Diamond Composite: A New Anode Material. *Diam. Relat. Mater.* **2019**, *98*, 107490.

(96) Schmid, H. K. Phase Identification in Carbon and BN Systems by EELS. *Microsc. Microanal. Microstruct.* **1995**, *6* (1), 99–111.

(97) Langenhorst, F.; Solozhenko, V. L. ATEM-EELS Study of New Diamond-like Phases in the B–C–N System. *Phys Chem Chem Phys* **2002**, *4* (20), 5183–5188.

(98) Dubrovinskaia, N.; Wirth, R.; Wosnitza, J.; Papageorgiou, T.; Braun, H. F.; Miyajima, N.; Dubrovinsky, L. An Insight into What Superconducts in Polycrystalline Boron-Doped Diamonds Based on Investigations of Microstructure. *Proc. Natl. Acad. Sci.* **2008**, *105* (33), 11619–11622.

(99) Kihn, Y.; Mirguet, C.; Calmels, L. EELS Studies of Ti-Bearing Materials and Ab Initio Calculations. *J. Electron Spectrosc. Relat. Phenom.* **2005**, *143* (2–3), 117–127.

(100) Abdallah, I.; Dupressoire, C.; Laffont, L.; Monceau, D.; Vande Put, A. STEM-EELS Identification of TiO_xN_y, TiN, Ti_2N and O, N Dissolution in the Ti2642S Alloy Oxidized in Synthetic Air at 650 °C. *Corros. Sci.* **2019**, *153*, 191–199.

(101) Tachibana, T.; Williams, B. E.; Glass, J. T. Correlation of the Electrical Properties of Metal Contacts on Diamond Films with the Chemical Nature of the Metal-Diamond Interface. II. Titanium Contacts: A Carbide-Forming Metal. *Phys. Rev. B* **1992**, *45* (20), 11975–11981.

(102) Liu, D. Y.; Hao, L. C.; Teng, Y.; Qin, F.; Shen, Y.; Tang, K.; Ye, J. D.; Zhu, S. M.; Zhang, R.; Zheng, Y. D.; Gu, S. L. Nitrogen Modulation of Boron Doping Behavior for Accessible N-Type Diamond. *APL Mater.* **2021**, *9* (8), 081106.

(103) Arnault, J. C. X-Ray Photoemission Spectroscopy Applied to Nanodiamonds: From Surface Chemistry to in Situ Reactivity. *Diam. Relat. Mater.* **2018**, *84*, 157–168.

(104) Ichibha, T.; Hongo, K.; Motochi, I.; Makau, N. W.; Amolo, G. O.; Maezono, R. Adhesion of Electrodes on Diamond (111) Surface: A DFT Study. *Diam. Relat. Mater.* **2018**, *81*, 168–175.

(105) Tachibana, T.; Glass, J. T. Correlation of Interface Chemistry to Electrical Properties of Metal Contacts on Diamond. *Diam. Relat. Mater.* **1993**, *2* (5–7), 963–969.

(106) Chun, S.-E.; Evanko, B.; Wang, X.; Vonlanthen, D.; Ji, X.; Stucky, G. D.; Boettcher, S. W. Design of Aqueous Redox-Enhanced Electrochemical Capacitors with High Specific Energies and Slow Self-Discharge. *Nat. Commun.* **2015**, *6* (1), 7818.

(107) Vonlanthen, D.; Lazarev, P.; See, K. A.; Wudl, F.; Heeger, A. J. A Stable Polyaniline-benzoquinone-hydroquinone Supercapacitor. *Adv. Mater.* **2014**, *26* (30), 5095–5100.

(108) Mai, L.-Q.; Minhas-Khan, A.; Tian, X.; Hercule, K. M.; Zhao, Y.-L.; Lin, X.; Xu, X. Synergistic Interaction between Redox-Active Electrolyte and Binder-Free Functionalized Carbon for Ultrahigh Supercapacitor Performance. *Nat. Commun.*

2013, *4* (1), 2923.

(109) Geng, H.; Cheng, M.; Wang, B.; Yang, Y.; Zhang, Y.; Li, C. C. Electronic Structure Regulation of Layered Vanadium Oxide via Interlayer Doping Strategy toward Superior High-rate and Low-temperature Zinc-ion Batteries. *Adv. Funct. Mater.* **2020**, *30* (6), 1907684.

(110) Yu, S.; Yang, N.; Zhuang, H.; Mandal, S.; Williams, O. A.; Yang, B.; Huang, N.; Jiang, X. Battery-like Supercapacitors from Diamond Networks and Water-Soluble Redox Electrolytes. *J. Mater. Chem. A* **2017**, *5* (4), 1778–1785.

(111) Wang, J.; He, Z.; Tan, X.; Wang, T.; He, X.; Zhang, L.; Huang, J.; Chen, G.; Du, K. Hybrid Supercapacitors from Porous Boron-Doped Diamond with Water-Soluble Redox Electrolyte. *Surf. Coat. Technol.* **2020**, *398*, 126103.

(112) Long, J.; Guan, L.; Wang, J.; Liu, H.; Wang, B.; Xiong, Y. Battery-like Flexible Supercapacitors from Vertical 3D Diamond/Graphite Composite Films on Carbon Cloth. *Carbon* **2022**, *197*, 400–407.

(113) Banerjee, D.; Sankaran, K. J.; Deshmukh, S.; Yeh, C.-J.; Gupta, M.; Lin, I.-N.; Haenen, K.; Kanjilal, A.; Sinha Roy, S. Single-Step Synthesis of Core-Shell Diamond-Graphite Hybrid Nano-Needles as Efficient Supercapacitor Electrode. *Electrochimica Acta* **2021**, *397*, 139267.

(114) Banerjee, D.; Sankaran, K. J.; Deshmukh, S.; Ficek, M.; Yeh, C.-J.; Ryl, J.; Lin, I.-N.; Bogdanowicz, R.; Kanjilal, A.; Haenen, K.; Sinha Roy, S. Single-Step Grown Boron Doped Nanocrystalline Diamond-Carbon Nanograss Hybrid as an Efficient Supercapacitor Electrode. *Nanoscale* **2020**, *12* (18), 10117–10126.

(115) Xiong, Y.; Wang, Y.; Zhou, J.; Liu, F.; Hao, F.; Fan, Z. Electrochemical Nitrate Reduction: Ammonia Synthesis and the Beyond. *Adv. Mater.* **2024**, *36* (17), 2304021.

(116) Liu, D.; Qiao, L.; Peng, S.; Bai, H.; Liu, C.; Ip, W. F.; Lo, K. H.; Liu, H.; Ng, K. W.; Wang, S.; Yang, X.; Pan, H. Recent Advances in Electrocatalysts for Efficient Nitrate Reduction to Ammonia. *Adv. Funct. Mater.* **2023**, *33* (43), 2303480.

(117) Zhao, X.; Jiang, Y.; Wang, M.; Liu, S.; Wang, Z.; Qian, T.; Yan, C. Optimizing

Intermediate Adsorption via Heteroatom Ensemble Effect over RuFe Bimetallic Alloy for Enhanced Nitrate Electroreduction to Ammonia. *Adv. Energy Mater.* **2023**, *13* (31), 2301409.

(118) Wang, Y.; Xu, A.; Wang, Z.; Huang, L.; Li, J.; Li, F.; Wicks, J.; Luo, M.; Nam, D.-H.; Tan, C.-S.; Ding, Y.; Wu, J.; Lum, Y.; Dinh, C.-T.; Sinton, D.; Zheng, G.; Sargent, E. H. Enhanced Nitrate-to-Ammonia Activity on Copper–Nickel Alloys via Tuning of Intermediate Adsorption. *J. Am. Chem. Soc.* **2020**, *142* (12), 5702–5708.

(119) Zhong, W.; Gong, Z.; He, Z.; Zhang, N.; Kang, X.; Mao, X.; Chen, Y. Modulating Surface Oxygen Species via Facet Engineering for Efficient Conversion of Nitrate to Ammonia. *J. Energy Chem.* **2023**, *78*, 211–221.

(120) Fang, L.; Lu, S.; Wang, S.; Yang, X.; Song, C.; Yin, F.; Liu, H. Defect Engineering on Electrocatalysts for Sustainable Nitrate Reduction to Ammonia: Fundamentals and Regulations. *Chem. – Eur. J.* **2024**, *30* (20), e202303249.

(121) Lu, S.; Lin, G.; Yan, H.; Li, Y.; Qi, T.; Li, Y.; Liang, S.; Jiang, L. In Situ Facet Transformation Engineering over Co_3O_4 for Highly Efficient Electroreduction of Nitrate to Ammonia. *ACS Catal.* **2024**, *14* (19), 14887–14894.

(122) Zhao, F.; Hai, G.; Li, X.; Jiang, Z.; Wang, H. Enhanced Electrocatalytic Nitrate Reduction to Ammonia on Cobalt Oxide Nanosheets via Multiscale Defect Modulation. *Chem. Eng. J.* **2023**, *461*, 141960.

(123) Zhu, R.; Qin, Y.; Wu, T.; Ding, S.; Su, Y. Periodic Defect Engineering of Iron–Nitrogen–Carbon Catalysts for Nitrate Electroreduction to Ammonia. *Small* **2024**, *20* (8), 2307315.

(124) Wang, Z.; Liu, S.; Zhao, X.; Wang, M.; Zhang, L.; Qian, T.; Xiong, J.; Yang, C.; Yan, C. Interfacial Defect Engineering Triggered by Single Atom Doping for Highly Efficient Electrocatalytic Nitrate Reduction to Ammonia. *ACS Mater. Lett.* **2023**, *5* (4), 1018–1026.

(125) Wang, Y.; Xia, S.; Cai, R.; Zhang, J.; Wang, J.; Yu, C.; Cui, J.; Zhang, Y.; Wu, J.; Yang, S.; Tan, H. H.; Wu, Y. Accelerating Industrial-level NO_3^- Electroreduction to

Ammonia on Cu Grain Boundary Sites via Heteroatom Doping Strategy. *Small* **2023**, *19* (26), 2302295.

(126) Zhang, S.; Dou, M.; Liu, M.; Yi, J.; Chen, M.; Wu, L. Electrosynthesis of Ammonia from Nitrate Using a Self-Activated Carbon Fiber Paper. *Inorg. Chem.* **2024**, *63* (31), 14736–14745.

(127) Li, T.; Tang, C.; Guo, H.; Wu, H.; Duan, C.; Wang, H.; Zhang, F.; Cao, Y.; Yang, G.; Zhou, Y. In Situ Growth of Fe_2O_3 Nanorod Arrays on Carbon Cloth with Rapid Charge Transfer for Efficient Nitrate Electroreduction to Ammonia. *ACS Appl. Mater. Interfaces* **2022**, *14* (44), 49765–49773.

(128) Song, Z.; Liu, Y.; Zhong, Y.; Guo, Q.; Zeng, J.; Geng, Z. Efficient Electroreduction of Nitrate into Ammonia at Ultralow Concentrations via an Enrichment Effect. *Adv. Mater.* **2022**, *34* (36), 2204306.

(129) Zhai, Z.; Chen, B.; Zhang, C.; Liu, L.; Song, H.; Zheng, Z.; Li, J.; Yang, B.; Jiang, X.; Huang, N. Construction of Porous Diamond Film with Enhanced Electric Double-Layer Capacitance via Regrowth of Diamond Nanoplatelets. *Funct. Diam.* **2023**, *3* (1), 2263468.

(130) Yang, B.; Yu, B.; Lu, J.; Li, H.; Zhai, Z.; Guo, X.; Huang, N.; Liu, L.; Jiang, X. Tailoring Optical Emission of Silicon-Vacancy Centers in Two-Dimensional Diamond Nanosheets via a Two-Step Oxidation Approach. *Funct. Diam.* **2023**, *3* (1), 2211074.

(131) Kuang, P.; Natsui, K.; Feng, C.; Einaga, Y. Electrochemical Reduction of Nitrate on Boron-Doped Diamond Electrodes: Effects of Surface Termination and Boron-Doping Level. *Chemosphere* **2020**, *251*, 126364.

(132) Kuang, P.; Natsui, K.; Einaga, Y.; Feng, C.; Cui, Y.; Zhang, W.; Deng, Y. Annealing Enhancement in Stability and Performance of Copper Modified Boron-Doped Diamond (Cu-BDD) Electrode for Electrochemical Nitrate Reduction. *Diam. Relat. Mater.* **2021**, *114*, 108310.

(133) Chen, S.; Lin, Q.; Ji, Z.; Sun, Z.; Shen, B. Ultrahigh Mechanical Robustness of Vertical Graphene Sheets Covalently Bonded to Diamond. *Carbon* **2023**, *201*,

390–398.

(134) Ma, Y.; Sun, X.; Yang, N.; Xia, J.; Zhang, L.; Jiang, X. Shape-controlled Growth of Carbon Nanostructures: Yield and Mechanism. *Chem. – Eur. J.* **2015**, *21* (35), 12370–12375.

(135) Qin, Y.; Eggers, M.; Staedler, T.; Jiang, X. Symmetric Growth of Carbon Nanosheets on Cu Nanowires by a Surface Diffusion Mechanism. *Nanotechnology* **2007**, *18* (34), 345607.

(136) Liu, Y.; Zhou, J.; Chen, L.; Zhang, P.; Fu, W.; Zhao, H.; Ma, Y.; Pan, X.; Zhang, Z.; Han, W.; Xie, E. Highly Flexible Freestanding Porous Carbon Nanofibers for Electrodes Materials of High-Performance All-Carbon Supercapacitors. *ACS Appl. Mater. Interfaces* **2015**, *7* (42), 23515–23520.

(137) Mao, Y.; He, J.; Sun, X.; Li, W.; Lu, X.; Gan, J.; Liu, Z.; Gong, L.; Chen, J.; Liu, P.; Tong, Y. Electrochemical Synthesis of Hierarchical Cu_2O Stars with Enhanced Photoelectrochemical Properties. *Electrochimica Acta* **2012**, *62*, 1–7.

(138) Hsu, Y.-K.; Yu, C.-H.; Chen, Y.-C.; Lin, Y.-G. Fabrication of Coral-like Cu_2O Nanoelectrode for Solar Hydrogen Generation. *J. Power Sources* **2013**, *242*, 541–547.

(139) Lu, F.; Fu, Z.; Bai, X.; Hao, T.; Liu, T.; Zheng, T. Research on the Growth State and Performance of Diamond Coatings Based on Different Carbon Source Concentration and Temperature. *Fuller. Nanotub. Carbon Nanostructures* **2022**, *30* (8), 830–838.

(140) Pang, H.; Wang, X.; Zhang, G.; Chen, H.; Lv, G.; Yang, S. Characterization of Diamond-like Carbon Films by SEM, XRD and Raman Spectroscopy. *Appl. Surf. Sci.* **2010**, *256* (21), 6403–6407.

(141) Cai, L.; Zhang, X.; Wang, Q.; Liu, Y. Selective Reduction of NO_3^- to N_2 Using a Highly Stable Cu^0/Cu_2O-PANI-CNTs as a Photocatalyst at Neutral pH. *Chem. Eng. J.* **2023**, *475*, 146261.

(142) Zhang, Y.; Zhou, X.; Zhao, Y.; Liu, Z.; Ma, D.; Chen, S.; Zhu, G.; Li, X. One-Step Solvothermal Synthesis of Interlaced Nanoflake-Assembled Flower-like

Hierarchical Ag/Cu_2O Composite Microspheres with Enhanced Visible Light Photocatalytic Properties. *RSC Adv.* **2017**, *7* (12), 6957–6965.

(143) Zheng, X.; Tian, Z.; Bouchal, R.; Antonietti, M.; López-Salas, N.; Odziomek, M. Tin (II) Chloride Salt Melts as Non-innocent Solvents for the Synthesis of Low-temperature Nanoporous Oxo-carbons for Nitrate Electrochemical Hydrogenation. *Adv. Mater.* **2024**, *36* (13), 2311575.

(144) Messias, I.; Winkler, M. E. G.; Costa, G. F.; Mariano, T.; Souza Junior, J. B.; Neckel, I. T.; Figueiredo, M. C.; Singh, N.; Nagao, R. Role of Structural and Compositional Changes of Cu_2O Nanocubes in Nitrate Electroreduction to Ammonia. *ACS Appl. Energy Mater.* **2024**, *7* (19), 9034–9044.

(145) Bai, L.; Franco, F.; Timoshenko, J.; Rettenmaier, C.; Scholten, F.; Jeon, H. S.; Yoon, A.; Rüscher, M.; Herzog, A.; Haase, F. T.; Kühl, S.; Chee, S. W.; Bergmann, A.; Beatriz, R. C. Electrocatalytic Nitrate and Nitrite Reduction toward Ammonia Using Cu_2O Nanocubes: Active Species and Reaction Mechanisms. *J. Am. Chem. Soc.* **2024**, *146* (14), 9665–9678.

(146) Hu, T.; Wang, C.; Wang, M.; Li, C. M.; Guo, C. Theoretical Insights into Superior Nitrate Reduction to Ammonia Performance of Copper Catalysts. *ACS Catal.* **2021**, *11* (23), 14417–14427.

(147) Qin, J.; Chen, L.; Wu, K.; Wang, X.; Zhao, Q.; Li, L.; Liu, B.; Ye, Z. Electrochemical Synthesis of Ammonium from Nitrates via Surface Engineering in Cu_2O(100) Facets. *ACS Appl. Energy Mater.* **2022**, *5* (1), 71–76.

(148) Hammer, B.; Nørskov, J. K. Electronic Factors Determining the Reactivity of Metal Surfaces. *Surf. Sci.* **1995**, *343* (3), 211–220.

(149) Guo, Y.; Zhang, R.; Zhang, S.; Zhao, Y.; Yang, Q.; Huang, Z.; Dong, B.; Zhi, C. Pd Doping-Weakened Intermediate Adsorption to Promote Electrocatalytic Nitrate Reduction on TiO_2 Nanoarrays for Ammonia Production and Energy Supply with Zinc–Nitrate Batteries. *Energy Environ. Sci.* **2021**, *14* (7), 3938–3944.

(150) Wang, V.; Xu, N.; Liu, J.-C.; Tang, G.; Geng, W.-T. VASPKIT: A User-Friendly

Interface Facilitating High-Throughput Computing and Analysis Using VASP Code. *Comput. Phys. Commun.* **2021**, *267*, 108033.

(151) Lu, J.; Lv, S.; Park, H. S.; Chen, Q. Electrocatalytically Active and Charged Natural Chalcopyrite for Nitrate-Contaminated Wastewater Purification Extended to Energy Storage Zn-NO_3^- Battery. *J. Hazard. Mater.* **2024**, *477*, 135287.

(152) Ye, J.; Wang, A.; Yang, Y.; Qian, X.; Wan, C.; He, G.; Chen, H. Vacancy Enhanced Proton Preference in Bimetallic Phosphide Catalysts for Electrochemical Ammonia Synthesis and Energy Supply in Zn-NO_3^- Battery. *Chem. Eng. J.* **2024**, *487*, 150434.

(153) Zhang, R.; Guo, Y.; Zhang, S.; Chen, D.; Zhao, Y.; Huang, Z.; Ma, L.; Li, P.; Yang, Q.; Liang, G.; Zhi, C. Efficient Ammonia Electrosynthesis and Energy Conversion through a Zn-nitrate Battery by Iron Doping Engineered Nickel Phosphide Catalyst. *Adv. Energy Mater.* **2022**, *12* (13), 2103872.

(154) Jiang, H.; Chen, G.; Savateev, O.; Xue, J.; Ding, L.; Liang, Z.; Antonietti, M.; Wang, H. Enabled Efficient Ammonia Synthesis and Energy Supply in a Zinc–Nitrate Battery System by Separating Nitrate Reduction Process into Two Stages. *Angew. Chem. Int. Ed.* **2023**, *62* (13), e202218717.

(155) Lu, S.; Lin, G.; Yan, H.; Li, Y.; Qi, T.; Li, Y.; Liang, S.; Jiang, L. In Situ Facet Transformation Engineering over Co_3O_4 for Highly Efficient Electroreduction of Nitrate to Ammonia. *ACS Catal.* **2024**, *14* (19), 14887–14894.

(156) Li, S.; Ma, P.; Gao, C.; Liu, L.; Wang, X.; Shakouri, M.; Chernikov, R.; Wang, K.; Liu, D.; Ma, R.; Wang, J. Reconstruction-Induced NiCu-Based Catalysts towards Paired Electrochemical Refining. *Energy Environ. Sci.* **2022**, *15* (7), 3004–3014.

(157) Li, R.; Xiang, K.; Peng, Z.; Zou, Y.; Wang, S. Recent Advances on Electrolysis for Simultaneous Generation of Valuable Chemicals at Both Anode and Cathode. *Adv. Energy Mater.* **2021**, *11* (46), 2102292.

(158) Pei, Y.; Pi, Z.; Zhong, H.; Cheng, J.; Jin, F. Glycerol Oxidation-Assisted Electrochemical CO_2 Reduction for the Dual Production of Formate. *J. Mater. Chem.*

A **2022**, *10* (3), 1309–1319.

(159) Wei, X.; Li, Y.; Chen, L.; Shi, J. Formic Acid Electro-synthesis by Concurrent Cathodic CO_2 Reduction and Anodic CH_3OH Oxidation. *Angew. Chem. Int. Ed.* **2021**, *60* (6), 3148–3155.

(160) Si, D.; Xiong, B.; Chen, L.; Shi, J. Highly Selective and Efficient Electrocatalytic Synthesis of Glycolic Acid in Coupling with Hydrogen Evolution. *Chem Catal.* **2021**, *1* (4), 941–955.

(161) Fan, L.; Ji, Y.; Wang, G.; Chen, J.; Chen, K.; Liu, X.; Wen, Z. High Entropy Alloy Electrocatalytic Electrode toward Alkaline Glycerol Valorization Coupling with Acidic Hydrogen Production. *J. Am. Chem. Soc.* **2022**, *144* (16), 7224–7235.

(162) Li, Z.; Qu, Y.; Hu, K.; Humayun, M.; Chen, S.; Jing, L. Improved Photoelectrocatalytic Activities of BiOCl with High Stability for Water Oxidation and MO Degradation by Coupling RGO and Modifying Phosphate Groups to Prolong Carrier Lifetime. *Appl. Catal. B Environ.* **2017**, *203*, 355–362.